STUDY ON THE DEVELOPMENT OF COLD ROLLED GRAIN ORIENTED STEEL

A THESIS

Submitted in partial fulfillment of the requirements for the award of the degree

of

DOCTOR OF PHILOSOPHY

by

VIPUL JAIN

Department of Metallurgical Engineering and Materials Science

Indian Institute of Technology Indore

October 2022

INDIAN INSTITUTE OF TECHNOLOGY INDORE

I hereby certify that the work which is being presented in the thesis entitled "**STUDY ON THE DEVELOPMENT OF COLD ROLLED GRAIN ORIENTED STEEL**", in the partial fulfillment of the requirements for the award of the degree of **Doctor of Philosophy** and submitted in the **Department of Metallurgical Engineering and Materials Science, Indian Institute of Technology Indore**, is an authentic record of my own work carried out during the time period from **December, 2017 to October, 2022** under the supervision of **Dr. Abhijit Ghosh**, Assistant Professor, Department of Metallurgical Engineering and Materials Science, IIT Indore.

The matter presented in this thesis has not been submitted by me for the award of any other degree of this or any other institute.

Vipul 19/04/2022

VIPUL JAIN

This is to certify that the above statement made by the candidate is correct to the best of my/our knowledge.

Abhijit Ghosh
19/04/23

Dr. ABHIJIT GHOSH (Thesis Supervisor)

Vipul Jain has successfully given his Ph.D. Oral Examination held on **April 19th, 2023.**

Abhijit Ghosh 19/04/23

Dr. ABHIJIT GHOSH (Thesis Supervisor)

ACKNOWLEDGEMENTS

I would sincerely like to thank my supervisor Dr. A. Ghosh for his constant guidance and inspiration at every stage of my Ph.D. tenure. I would also like to express my gratitude that this work could not be finished without his continuous motivation and patience.

I am thankful to the Department of Science and Technology (DST), New Delhi and IIT Indore for financial support. I am grateful to Mishra Dhatu Nigam Limited (MIDHANI), Hyderabad, and IIT Kharagpur for providing experimental facilities.

I would like to acknowledge Prof. N. K. Jain and Dr. Hemant Borkar, the faculty members of my Ph.D. Student's Progress Committee (PSPC) for their valuable comments and suggestions which encouraged me during my research. I also take this opportunity to thank Dr. Vinod Kumar, HOD of the Department of Metallurgical Engineering and Materials Science (MEMS) for his support in doing my research experiments.

I am grateful to Microstructure and Texture Engineering Laboratory (MTEL), Dept. of MEMS, Non-equilibrium Advanced Materials Engineering (NAME) Laboratory and Advanced Physical and Mechanical Metallurgy Lab, IIT Indore, for providing research facilities.

I would also like to express my sincere gratitude to Dr. Sudipta Patra from IIT BHU, Dr. Chandan Halder from IIT Indore, Dr. Sk. Md. Hasan from IIT Jodhpur and Mr. Pranabananda Modak from IIT Kharagpur for their kind help in experiments and for sharing their knowledge on various aspects related to this work.

The author genuinely wishes to thank Dr. Nikita Guha, Mr. Piyush Kumar, Dr. Sheetal K. Dewangan, Mr. Sarath K. Krishnan, Mr. Gaddam Shiva, Mr. Ankush Marodkar, Mr. Hitesh Patil and all the staff members of Dept. of MEMS for their assistance during my experimental work.

Above all, I acknowledge my parents, Mr. Anil Kumar Jain and Ms. Madhu Jain, other family members and friends for their endless patience and extreme support.

Dedicated to my

mother and father

LIST OF PUBLICATIONS

Papers Published:

1. **Vipul Jain**, A. Chatterjee, S. Patra, D. Chakrabarti, A. Ghosh (2020), Effect of tilt and twist angles on the cleavage crack propagation in ferritic steel, Int. J. Fract., 225, 115-121. (https://doi.org/10.1007/s10704-020-00467-x)
2. **Vipul Jain**, Pranabananda Modak, Sudipta Patra, Abhijit Ghosh (2022), Origin of Goss texture in Grain Oriented Electrical Steel: Role of Shear Bands, Materialia, 22, 101398. (https://doi.org/10.1016/j.mtla.2022.101398)
3. **Vipul Jain**, Sudipta Patra, Chandan Halder, Sk Md Hasan, Abhijit Ghosh (2022), Study on the formation of alligator crack and edge crack in high silicon grain oriented electrical steel during cold rolling, J. Appl. Phys., 132, 105101. (https://doi.org/10.1063/5.0097174)

Conferences:

1. **Vipul Jain**, A. Chatterjee, S. Patra, D. Chakrabarti, A. Ghosh, "Effect of tilt and twist angles on the cleavage crack propagation in ferritic steel", 6th Industry Academia Conclave (IAC) 2018, IIT Indore, India, 20 November 2018.
2. **Vipul Jain**, Pranabananda Modak, S. Patra, A. Ghosh, "Goss texture development in grain oriented electrical steel", 19th International Conference on Strength of Materials (ICSMA), Metz, France, 26th June-1st July 2022.

CONTENTS

LIST OF FIGURES

LIST OF TABLES

SYMBOLS

Symbol	Description
α-fiber	Orientations having rolling direction parallel to <110>
γ-fiber	Orientations having normal direction parallel to <111>
θ-fiber	Orientations having normal direction parallel to <001>
η-fiber	Orientations having normal direction parallel to <110>
Σ	Coincidence site lattice
ω	Angle of rotation of 3-axis PANanalytical® x-ray goniometer around axis parallel to normal direction with respect to sample
ψ	Angle of rotation of 3-axis PANanalytical® x-ray goniometer around axis parallel to rolling direction with respect to sample
μ	Coefficient of friction between rollers and rolling plate
$\dot{\varepsilon}_{ij}$	Deviatoric strain rate
σ_{kl}	Deviatoric stress
γ^s	Local shear rate
m_{ij}^s	Schmid tensor associated with slip and/or twinning systems
τ^s	Threshold shear stress
n	Inverse of rate sensitivity
s	Representing slip and/or twinning systems
Γ	Accumulated shear in a single grain

τ_0^s	Initial critical resolved shear stress
$\tau_0^s + \tau_1^s$	Back extrapolated critical resolved shear stress
θ_0	Initial hardening rate
θ_1	Asymptotic hardening rate
ε_{HR}	True strain during hot rolling
ε_{ICR}	True strain during intermediate cold rolling
ε_{CCR}	True strain during complete cold rolling
ε_{SCR}	True strain during single stage cold rolling
σ_f	Cleavage fracture stress
E	Young's modulus
ν	Poisson's ratio
γ_p	Effective surface energy
d_p	Effective grain size
φ_1, ϕ, φ_2	Euler angles as per Bunge notation representing orientation of crystal with respect to reference sample frame
θ	Inclination angle of shear bands from rolling direction
L_{SB}	Velocity gradient tensor on reference frame of shear bands
L_{25}, L_{15}	Velocity gradient tensor on sample reference obtained by incorporating θ (25°, 15°) in tensor transformation

ABBREVIATIONS

Abbreviation	Description
CRGO	Cold rolled grain oriented
RD	Rolling direction
ND	Normal direction
TD	Transverse direction
AGG	Abnormal grain growth
HE	High energy
CSL	Coincidence site lattice
HSI	High silicon
MSI	Medium silicon
LSI	Low silicon
HR	Hot rolling
AC	Air cooling
HBA	Hot band annealing
ICR	Intermediate cold rolling
IA	Intermediate annealing
CCR	Complete cold rolling
SCR	Single stage cold rolling
PR	Primary recrystallization

SR	Secondary recrystallization
DSC	Differential scanning calorimetry
OM	Optical microscope
FESEM	Field emission scanning electron microscope
EDS	Energy dispersive spectroscope
IPF	Inverse pole figure
ODF	Orientation distribution function
GOS	Grain orientation spread
FEM	Finite element method
VPSC	Visco-plastic self-consistent
CRSS	Critical resolved shear stress
ECF	Specimen cut from edge cracked sample to examine fracture surface
EC1	Specimen cut from edge cracked sample to study microstructure
ACF	Specimen cut from alligator cracked sample to examine fracture surface
AC1	Specimen taken out from alligator cracked sample far away from the cracked region to analyze microstructure
AC2	Specimen taken out from alligator cracked sample from the cracked region to study microstructure and microtexture
BCC	Body centered cubic

ABSTRACT

Cold rolled grain oriented (CRGO) steel is a Fe-Si alloy which is commercially produced for the application in transformer cores. A thin sheet of CRGO steel is manufactured by following hot rolling, cold rolling, and various intermediate annealing steps. In the final steps, primary and secondary recrystallization annealing is carried out where coarse Goss ({110}<001>) oriented grains are deliberately grown via abnormal grain growth phenomenon. However, the development of Goss orientation is still not completely understood. Furthermore, higher silicon concentration in electrical steel is beneficial in reducing magnetostriction and eddy current losses, but cracks can develop during cold rolling of Fe-Si alloy having more than 3 wt. % Si. In the present investigation, three Fe-Si alloys with 3.78 wt.%, 3.23 wt.% and 2.98 wt.% Si have been prepared in vacuum induction furnace. The microstructure and crystallographic texture after different stages of processing have been characterized using various experimental techniques such as Electron Backscatter Diffraction (EBSD), X-Ray Diffraction (XRD) etc. Analytical stress and crystallographic texture have been predicted using Finite Element Method (FEM) and crystal plasticity based analysis, respectively. Edge crack and alligator crack have been found to develop during cold rolling of Fe-3.78 wt.% Si. The FEM based stress analysis suggests that tensile stress along normal and rolling direction may evolve during cold rolling, which could be sufficient to develop such cracks. Also, the possibility of crack formation during cold rolling increases with increasing Si content. Hot band annealing and intermediate annealing treatment between cold rolling passes were found to be helpful in eliminating these cracks.

After successfully completing the cold rolling operation, step-by-step development of microstructure and texture have been studied in detail. It has been observed that Goss grains developed at the surface during hot rolling and hot band annealing, did not remain stable during subsequent cold rolling. The fraction Goss orientation after cold rolling becomes negligible (<2%) and it has been found to be independent of the sheet thickness and Si content. However, Goss orientation revived after primary recrystallization. Partial recrystallization study confirms that the shear bands developed during cold rolling act as the new source of Goss orientation. High magnification EBSD scan revealed the development of Goss orientation inside the shear band of {111}<112> oriented grain. Further, crystal plasticity based study suggests that under pure shear loading on an inclined plane at 25° angle from the rolling direction, (111)[$\bar{1}\,\bar{1}\,2$] oriented grain rotate towards Goss orientation. Present study confirms that intermediate annealing between cold rolling passes is not essential from the perspective of achieving Goss orientation in subsequent primary recrystallization. The boundaries of the Goss oriented grains evolved during final annealing treatment have more convex curvatures compared to the grain boundaries surrounding the other orientations. However, abnormal grain growth of Goss oriented grains has not been observed during secondary recrystallization in the present study. A detailed analysis on the role of precipitates on secondary recrystallization may provide further insight.

Keywords: Cold rolled grain oriented steel, Crystallographic texture, Goss orientation, Shear bands, Finite element method, Crystal plasticity

CHAPTER 1

Introduction

1.1 General Background:

Cold rolled grain oriented (CRGO) steel is an Fe-Si alloy which is widely used as a core material in transformers (Lin et al. 1995). Magnetic properties such as high permeability and low coercivity are basic requirements for a material to be used as transformer core with low hysteresis losses (Moses 1990). The processing route of CRGO steel typically includes hot rolling, cold rolling, primary recrystallization annealing and secondary recrystallization annealing. The suitability of CRGO steel in transformers is due to the presence of cube-on-edge crystallographic texture, called as Goss ($\{110\}\langle 001\rangle$) texture, which develops via abnormal grain growth during the final stages of processing (Hayakawa 2017).

During the application, core material is associated with different kinds of losses which are known as hysteresis loss and eddy current loss. Goss orientation provides minimum hysteresis loss as its rolling direction is preferentially aligned towards easy magnetization of iron, <001> (Kestens et al. 2008). Moreover, reduction of eddy current loss can be achieved by increasing silicon concentration in CRGO steel (Haiji et al. 1996), as it increases the electricity resistivity. Significant research has been carried out to minimize core losses in CRGO steel in the past 70 years which mainly includes improving the sharpness of Goss orientation and achieving thinner cold rolled sheet (Ushigami et al. 2003). However, the development of Goss texture in CRGO steel is still not completely understood.

In India, transmission losses cover more than 27 billion kWh which is approximately 18% of total power generation (1.5 trillion kWh). Iron core loss comprises more than 50% of the total transmission losses. Furthermore, the requirement of CRGO steel in India is fulfilled by importing. In order to establish a feasible commercial production of CRGO steel in the country, it is important to understand the development of Goss texture through different steps in the processing of CRGO steel.

1.2 Objectives

The following are the major objectives of the present thesis:

- To understand the development of microstructure and crystallographic texture during different stages in the production of CRGO steel.
- To understand the origin of Goss texture in CRGO steel.
- To understand the effect of varying silicon content on the development of Goss texture in CRGO steel.

1.3 Thesis organization

The results and discussion section of this thesis are divided into five major chapters (Chapter 4 to Chapter 8) as follows:

Chapter 4

Silicon is known to contribute to solid solution strengthening of iron. But increasing silicon content also increases the brittleness of Fe-Si steel which can develop cracks during cold rolling operations. The present study investigates the role of microstructure and crystallographic texture on the formation of edge crack and alligator crack which developed during cold rolling of high silicon (3.78 wt.%) CRGO steel. Analytical state of stress developed at different regions of the plate during cold rolling was predicted using Finite Element Method based analysis and was further correlated with the formation of such cracks.

Chapter 5

The present study demonstrates complete step by step development of microstructure and crystallographic texture after different stages in the processing of 3.78 wt.% CRGO steel. This chapter critically examines the role of different processing steps on Goss texture development.

Chapter 6

The identification of the primary source of Goss orientation in polycrystalline CRGO steel is an absolute necessity. This chapter explores the role of shear bands developed during cold rolling on the evolution of Goss texture in CRGO steel. Crystal plasticity based analysis has been carried out to get further insight on the development of Goss orientation.

Chapter 7

In this chapter, three CRGO steels with varying silicon concentration of 3.78 wt.%, 3.23 wt.% and 2.98 wt.% has been compared. The present work investigates the effect of varying silicon concentration on the development of rolling cracks and crystallographic texture in CRGO steel. Crystal plasticity based model was used to understand the texture development in CRGO steel based on amount of silicon. More specifically, the study examines the role of silicon content on Goss texture development.

Chapter 8

This chapter is focused on to understand the development of Goss orientation during cold rolling based on sheet thickness in CRGO steel having 2.98 wt.% Si. Crystal plasticity based analysis was incorporated to understand the stability of Goss orientation during cold rolling. This work specifically explores the development of shear bands and Goss texture at different levels of the cold rolled sheet.

CHAPTER 2

Literature Review

2.1 Composition of cold rolled grain oriented (CRGO) steel

CRGO steel has been widely used in transformer cores due to its desired magnetic properties such as low hysteresis loss and high permeability. CRGO steel is an Fe-Si steel having Si as a main constituent and other important alloying elements such as, Mn, Al, S and N, in small proportion. A typical Fe-Si phase diagram is shown in **Fig. 2.1**. The solid solubility of silicon in ferrite (BCC-Iron) varies between 4 wt.% to 6 wt.% at room temperature (González et al. 2013). Silicon is a ferrite phase stabilizer and austenite phase in Fe-Si steel phase space diminishes when silicon concentration exceeds 2 wt.% (**Fig. 2.1**).

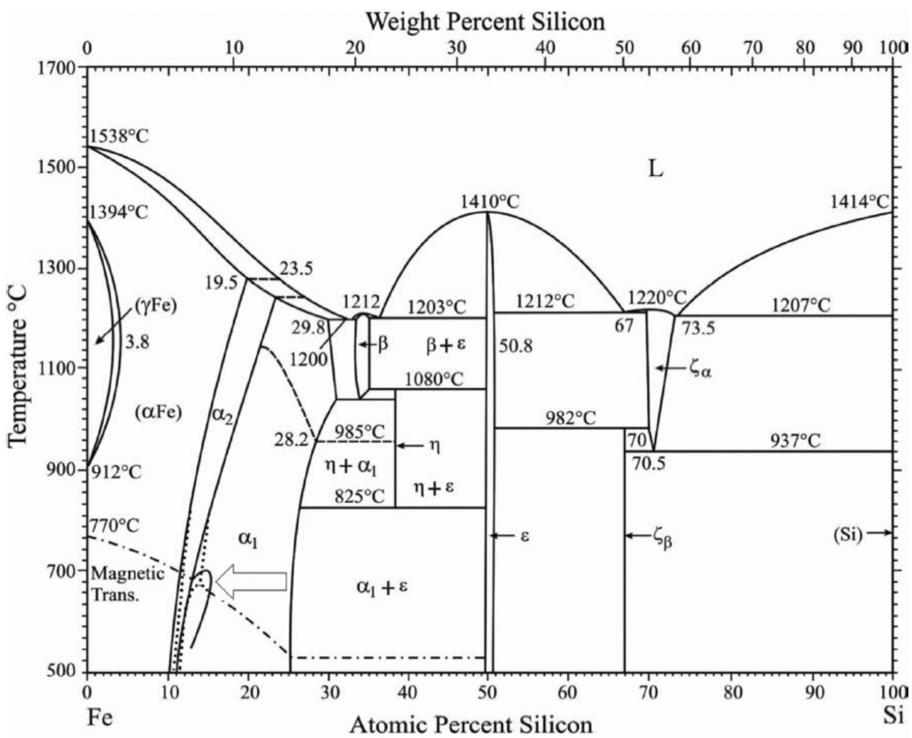

Figure 2.1: Fe-Si phase diagram (González et al. 2013)

Single ferrite phase is generally preferred as the presence of second phase refines the grain structure during multiple heat treatments. The fine grains consist more grain boundaries which impedes the motion of domains during magnetization and demagnetization process, ultimately increasing the hysteresis loss in transformer core (Mehring et al. 2001). The fine precipitates such as sulfides and nitrides act as inhibitors during the processing of CRGO steel. But the presence of Al, Mn can also promote austenite phase formation (Zhu et al. 2022). Therefore, the amount of silicon is generally selected to be more than 2 wt.% and the other elements are kept as low as possible. Magnetic behavior can further be improved by increasing the silicon concentration up to around 6.5 wt.% as it enhances the permeability of CRGO steel and helps in reducing the magnetostriction property and eddy current losses (Ouyang et al. 2019). However, processing CRGO steel with high silicon content can be challenging as it also increases flow stress and thus rolling load.

2.2 Processing of CRGO steel

The manufacturing methods have been developed in the past few decades to produce CRGO steel which offers low core losses (Ushigami et al. 2003). The common processing routes of CRGO steel are shown in **Fig. 2.2**. Slab reheating of the cast products is initially done to completely homogenize and solutionize all the precipitates. Hot and cold rolling are performed in multiple passes which are followed by two stage annealing technique known as primary and secondary recrystallization.

ARMCO Method (CGO)	Nippon Steel Method (HI-B)	Kawasaki Method (RG-H)
Steelmaking (Mn,S or Se)	Steelmaking (Al,N,Mn,S,Sn)	Steelmaking (Mn,Se or S ,Sb)
Hot rolling Slab reheating 1300℃ < T	Hot rolling Slab reheating 1300℃ < T	Hot rolling Slab reheating 1300℃ < T
Normalizing annealing	High Temp. annealing	Normalizing annealing
Primary cold rolling	Heavy cold rolling Reduction 87%	Primary cold rolling
Intermediate annealing		Intermediate annealing
Secondary cold rolling Reduction 50%		Secondary cold rolling Reduction 65%
Decarburization	Decarburization	Decarburization
Final annealing	Final annealing	Final annealing
Heat flattening Coating	Heat flattening Coating	Heat flattening Coating

Figure 2.2: Flow chart showing different methods for the processing of CRGO steel (Takahashi et al. 1996)

2.2.1 Hot Rolling

Microstructure development during hot rolling

Hot rolling is performed starting from temperature above 1200° C to reduce the thickness of the reheated slab up to around 2-3 mm (Günther et al. 2005). The microstructure development during hot rolling varies from surface to center of the rolled plate as shown in **Fig. 2.3**. The surface and sub-surface layers consist of equiaxed grains, whereas the central regions are comprised of elongated grains along RD. During hot rolling, the surfaces are subjected to fast cooling as the steel is in contact with the rollers. High shear stresses due to friction between rollers and the plate leads to dynamic recrystallization which promote equiaxed grains at the surface and sub-surface layers (Matsuo 1989). The negligible shear stresses at the centre leads to the retention of columnar grains which get elongated along RD.

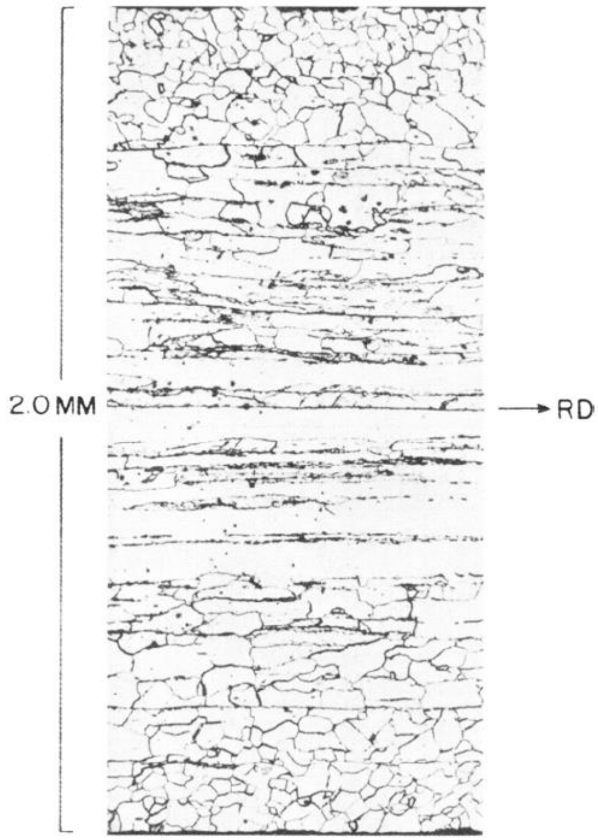

Figure 2.3: Through thickness microstructure after hot rolling showing structural inhomogeneities from surface to centre of the plate (Littmann 1975)

Texture development during hot rolling

The texture gradient has been reported to develop in the hot rolled microstructure (Raabe 2003). It appears due to different deformation modes acting through the thickness. The mid-thickness regions undergo plane strain deformation which develops common rolling textures consisting mostly α-fiber (RD||<110>) and γ-fiber (ND||<111>) crystallographic orientations (Hölscher et al. 1991, Raabe et al. 1992). The intensity of the formation of different rolling textures depends upon the hot rolling temperature and the amount of thickness reduction as shown in **Fig. 2.4**. On the other hand, high shear stresses at the surface regions aid the formation of shear texture having Goss, copper and brass type orientations (Hölscher et al. 1991, Shao et al. 2013, Bao et al. 2017, SHIN et al. 2008).

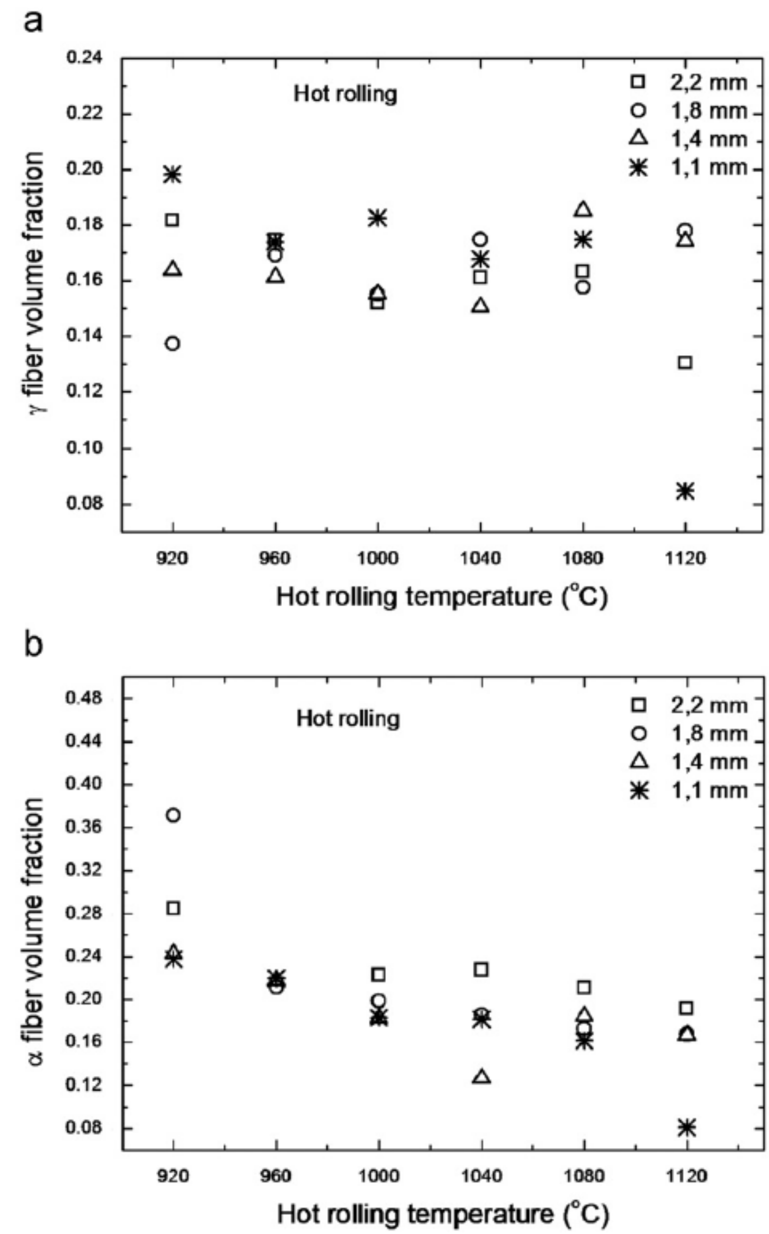

Figure 2.4: The intensity of α-fiber and γ-fiber texture as a function of hot rolling temperature subjected to different amount of thickness reduction (de Dafé et al. 2011)

Parameters involved in the development of the hot rolled structure

The microstructure and texture inhomogeneity during hot rolling also depends up on other factors such as, initial grain size, degree of deformation and finish roll temperature (Matsuo et al. 1986, Li et al. 2016). The extremely large grains before hot rolling affects the recrystallization process during hot rolling which can induce large hot bands throughout the thickness (Littmann 1975). The insufficient recrystallization due to low strain localization decreases the development of shear texture such as Goss orientation and likely develops rolling texture consisting mostly of α-fiber textured grains. It was reported that finish roll temperature below 850° C promotes through thickness inhomogeneity and γ-fiber crystallographic texture components (Hughes 1971). The high degree of deformation in the final pass during hot rolling can also lead to the development of prominent microstructure and texture gradient through the thickness (Matsuo et al. 1986).

Formation of precipitates during hot rolling

The precipitates are crucial during primary and secondary recrystallization annealing which influences the recrystallization process and abnormal grain growth, respectively (Gheorghies et al. 2009). The formation of precipitates such as, MnS and AlN, takes place during the hot rolling stage and their morphology depends up on the hot rolling temperature. **Table 2.1** shows the temperature range over which different precipitations take place during hot rolling. The size and density of precipitates during hot rolling strongly influences the formation of Goss texture during final annealing stages. Hot rolling above 1100° C ensures fine distribution and high density of the precipitates (Sakai et al. 1979).

Table 2.1: Precipitation and Goss texture distribution in hot-rolled or primary annealed sheets (Wang et al. 2016)

Hot Rolling Temperature (° C)	Precipitation in hot rolled sheets	Goss texture in hot rolled sheets	Goss texture in primary annealed sheets
900	Few coarse MnS, No fine AlN	-	Goss texture fraction: 1.75%, Distributed surface and central layers

1000	-	Weak Goss texture, Distributed subsurface layer	Goss Texture fraction: 1.04%, Distributed surface and central layers
1000	-	Weak Goss texture, Distributed subsurface layer	Goss Texture fraction: 1.43%, Distributed surface and central layers
1000	High density fine AlN, Mean size: 39.9 nm	Weak Goss texture, Distributed subsurface layer	Goss Texture fraction: 1.73%, Distributed surface and central layers
1100	Density: 15.4 μm^{-2}, High density fine AlN, Mean size: 55.1 nm	-	Goss Texture fraction: 2.11%, Distributed surface and central layers
(Matsuo 1989, Park et al. 2013)	Density: 21.9 μm^{-2}, High density fine MnS and high density fine AlN after hot band annealing	Strong Goss texture, Distributed subsurface layer	Goss Texture fraction: ≈ 1.8%, Mainly distributed subsurface layers

2.2.2 Hot Band Annealing

Annealing after hot rolling is usually performed to improve the formability and ductility during cold rolling. The microstructure and texture development during hot band annealing depends up on the annealing temperature and time. Annealing prior to cold rolling may not produce significant difference in the deformed structure, but later influences the primary recrystallized grain morphology (C. Hou 1996, Chang 2007). It was also shown that hot band annealing has slight influence on the development of various crystallographic orientations (Goss orientation, α-fiber, and γ-fiber texture components) during primary recrystallization, but shows huge impact on Goss texture development during secondary recrystallization annealing (Chang 2007). Importantly, the increase in size and distribution of precipitates during hot band annealing greatly affects the recrystallization behavior during primary recrystallization annealing and subsequent abnormal grain growth during secondary recrystallization annealing (Wang, Xu, Zhang, Fang, Lu, Misra, et al. 2015). The morphology of precipitates in the primary recrystallized structure with and without including the hot band annealing step in the process is shown in **Fig. 2.5**. The magnetic losses decreases with the addition of hot band annealing step in the process compared to the processing route without annealing (Chang 2005, Schneider et al. 2016).

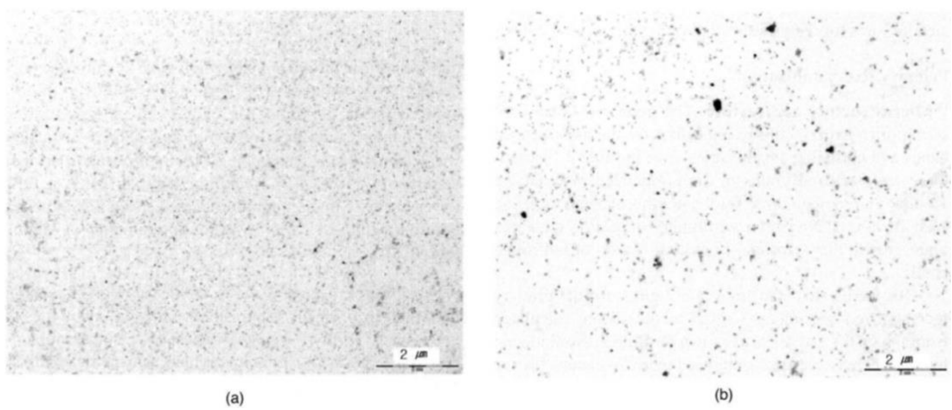

Figure 2.5: Size and distribution of precipitates in the primary recrystallized structure in the process (a) without hot band annealing, and (b) with hot band annealing (Chang 2005)

2.2.3 Cold Rolling

Microstructure and texture development during cold rolling

After hot band annealing, cold rolling is conducted to further reduce the thickness up to around 0.2-0.3 mm. The microstructure development during cold rolling depends up on the degree of deformation and grain structure prior to cold rolling (Hutchinson 1999). Through thickness heterogeneity develops in the deformed grain structure during cold rolling irrespective of their prior grain size. However, some microstructural features such as, shear bands, are favored inside large grains (T. Haratani et al. 1984, Ushioda et al. 1989, de Dafé et al. 2011). The texture evolution during cold rolling based on degree of deformation is represented in **Fig. 2.6**. The α- and γ-fiber texture components are typical rolling textures which develops during cold rolling (Hölscher et al. 1991). The grain size prior to cold rolling has little influence on the deformation texture. Only, the intensity of α- and γ-fiber texture components varies with the grain size prior to cold rolling (Campos et al. 2004).

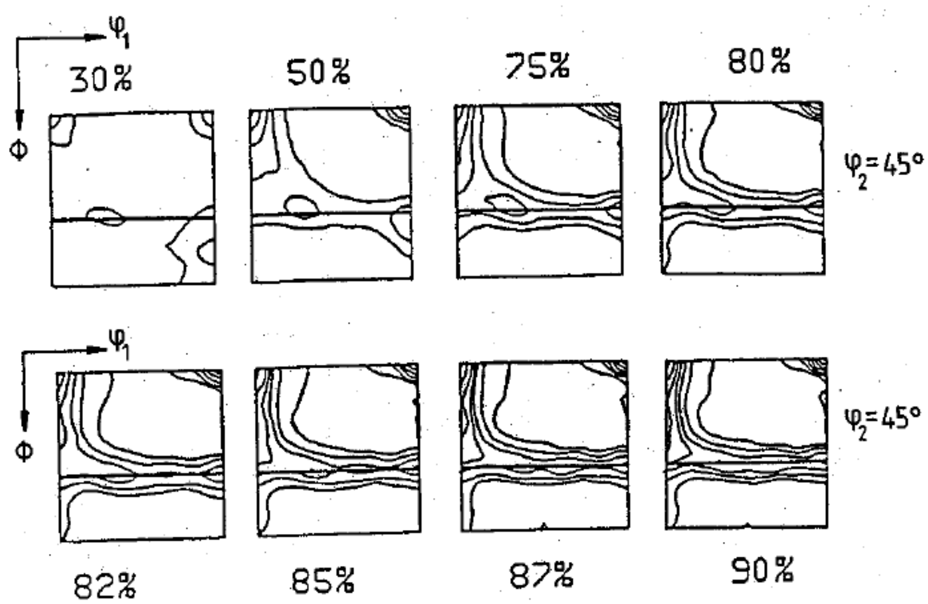

Figure 2.6: The development of crystallographic texture on increasing the degree of deformation during cold rolling (Hölscher et al. 1991)

Shear banding phenomenon during cold rolling

High strain localized areas in the form of shear bands which are tilted at certain inclination angle (typically between 25° - 35°) from the rolling direction, develop in the cold rolled structure. In general, shear band formation takes place inside large grains with favorable crystallographic orientations (Dorner et al. 2007, Nguyen-Minh et al. 2012, Schneider et al. 2016). The dependency of grain size prior to cold rolling on shear band formation is shown in **Fig. 2.7**. The orientations which have high Taylor factor such as, γ-fiber texture components, $\{111\}\langle 110\rangle$ and $\{111\}\langle 112\rangle$, and rotated Goss, are expected to possess high dislocation densities during deformation (Rajmohan 1997, Samajdar et al. 1997, Nguyen-Minh et al. 2012, Mehdi et al. 2020). Therefore, these orientations induce high strain hardening during cold rolling and may promote instability in the form of shear bands. The formation of shear bands during cold rolling is crucial for the Goss texture development in CRGO steel. However, the high strain accumulation inside shear band regions makes it difficult in examining the orientations developed inside those bands.

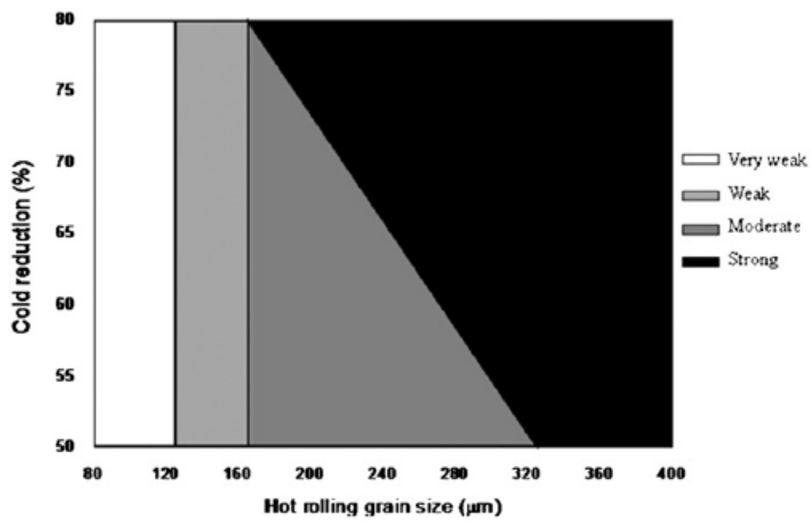

Figure 2.7: Intensity of shear band formation during cold rolling based on the grain size prior to cold rolling (de Dafé et al. 2011)

Prediction of deformation texture during cold rolling

Different crystal plasticity based models were developed to understand the evolution of crystallographic texture during cold rolling of bcc metals (Raabe 1995, Van Houtte et al. 1999). An example of the predicted cold rolling texture in low carbon steel based on LAMEL model is shown in **Fig. 2.8**. Similarly, various attempts were also made to predict the deformation texture quantitatively during cold rolling in CRGO steel. However, these simulations were unable to predict the texture development due to shear band formation. Some study reported the evolution of Goss orientation under shear deformation (T. Haratani et al. 1984, Ushioda et al. 1989), but those analysis were made on single crystals. Beside that, Goss orientation is known to be unstable under plane strain condition (Raabe et al. 2002). Furthermore, the formation of crystallographic orientations inside shear bands during cold rolling are associated with the geometrical softening phenomenon (Nguyen-Minh et al. 2012, Mehdi et al. 2020). But the predictability of the development of Goss orientation during shear band formation by the consideration of geometrical softening has not been explored much.

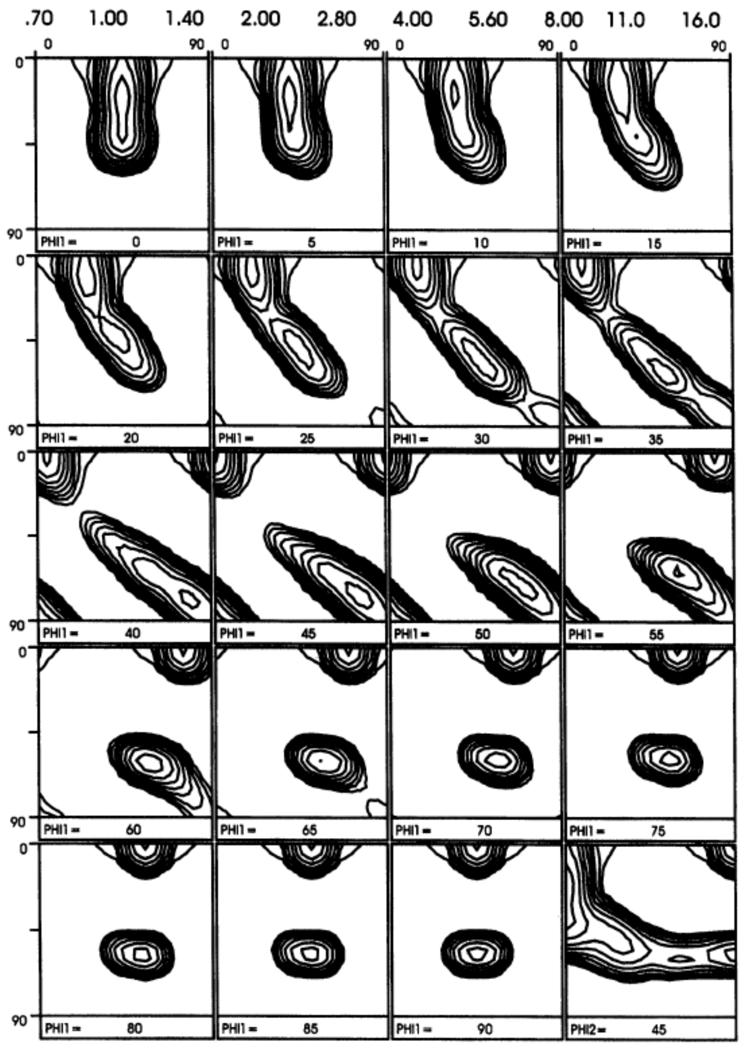

Figure 2.8: Prediction of cold rolling texture in low carbon steel using LAMEL model (Van Houtte et al. 1999)

2.2.4 Intermediate Annealing between Cold Rolling Passes

The intermediate annealing mainly improves the formability and ductility and it becomes easier to cold roll CRGO steel having high silicon content without any defects (Jahangiri et al. 2014). Annealing treatment between cold rolling stages was reported to be ineffective in producing any modification (qualitatively) in the texture development during deformation (Campos et al. 2004). However, the overall size of the primary recrystallized grains reduces due to multiple heat treatment steps involved in the process, which further leads to reduction in size of the secondary recrystallized grains. It has been reported that CRGO steel produced by two stage cold rolling with intermediate annealing treatment has inferior magnetic properties compared to CRGO steel processed by single cold rolling (Taguchi et al. 1975, Matsuo 1989, Qin et al. 2015). Nevertheless, to maximize the benefit of intermediate annealing in the subsequent annealing processes after cold rolling, equivalent degree of deformation during first and second cold rolling stages is appropriate to consider (Song et al. 2016). Due to intermediate annealing, the γ-fiber texture components in the primary recrystallized grain structure were enhanced, which showed a substantial impact during secondary recrystallization annealing step (Song et al. 2016, Song et al. 2021). The secondary recrystallized microstructures, developed in the two stage cold rolling processes with different amount of deformation before and after intermediate annealing, are shown in **Fig. 2.9**. The advantage of intermediate annealing treatment in-between two cold rolling stages with equal deformation can be noted.

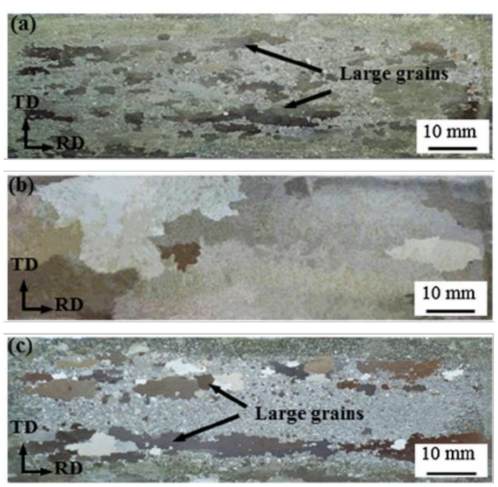

Figure 2.9: Microstructure after secondary recrystallization annealing developed considering intermediate annealing step between different two

stage cold rolling schedules having (a) low degree of deformation during first cold rolling stage and high degree of deformation during second cold rolling stage, (b) equivalent degree of deformation during first and second cold rolling stages, and (c) high degree of deformation during first cold rolling stage and low degree of deformation during second cold rolling stage (Song et al. 2016)

2.2.5 Primary Recrystallization Annealing

Recrystallized microstructure and role of inhibitors

The cold rolled sheets are first subjected to primary annealing treatment within the final two stage annealing process. The temperature and time for primary recrystallization annealing is chosen in such a way that the recrystallization process completes without extensive grain growth. A typical primary annealed microstructure consists homogeneous distribution of recrystallized grains throughout the thickness as shown in **Fig. 2.10**. In general, the primary recrystallization process is performed under decarburizing annealing environment (Harase et al. 1991, Gangli et al. 1994, Hayakawa et al. 2002, Yang et al. 2017). The average grain size of primary recrystallized grains depends up on size of the grains prior to cold rolling. The role of precipitates during primary recrystallization annealing is crucial in achieving recrystallized grain structure. The precipitates such as, MnS and AlN, act as inhibitors which helps in pining down the grain boundaries and restrict grain growth. The size, density and distribution of the inhibitors affects the grain size and morphology of the primary recrystallized grains (Park et al. 2013, Yang et al. 2017).

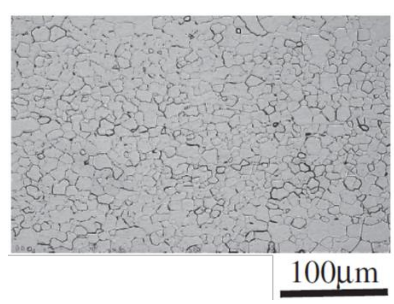

Figure 2.10: Microstructure after primary recrystallization annealing showing homogeneously formed recrystallized grains (Omura et al. 2013)

Crystallographic orientations in the primary recrystallized structure

The development of crystallographic orientations during primary recrystallization annealing is based up on the deformation texture of the cold rolled sheet (Heo et al. 1999, Imamura et al. 2013, Liu et al. 2014). The nucleation stage during the formation of primary recrystallized grain structure is dominated by high strained areas developed after cold rolling such as, shear bands, surface layers and grain boundaries (Schneider et al. 2016, Mehdi et al. 2019). A small area of the grain boundary region after partial recrystallization is shown in **Fig. 2.11** which represents that, grains started recrystallizing from the high strain localized areas. The recrystallization texture after the completion of primary annealing mainly consists of α-fiber, γ-fiber, cube and Goss orientations. The Goss oriented grains formed in the primary recrystallized structure are of major importance. However, the abnormal growth conditions during subsequent secondary recrystallization annealing process are only favorable for few primary Goss grains. The orientations of the grains surrounding the potential Goss grains and the character of their common grain boundaries have substantial role on their selective growth.

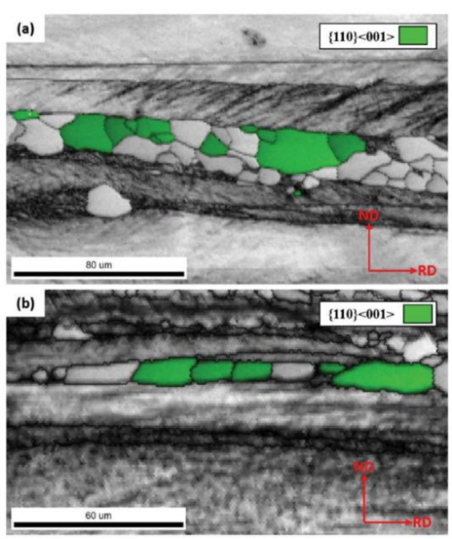

Figure 2.11: Partially recrystallized grain boundary regions representing areas with high strain energy initiates the recrystallization process (Mehdi et al. 2019)

Detrimental factors in the primary recrystallized structure

The completion of the recrystallization process during primary annealing is necessary for subsequent abnormal grain growth. An example is shown in **Fig. 2.12**, in which the incomplete primary grain structure leads to improper abnormal growth environment impeding the secondary recrystallization process. Moreover, the inhomogeneous distribution of the inhibiting agents or absence of appropriate second phase particles in the cold rolled sheet also affects the primary recrystallized grain structure (Li et al. 2011, Hayakawa 2017).

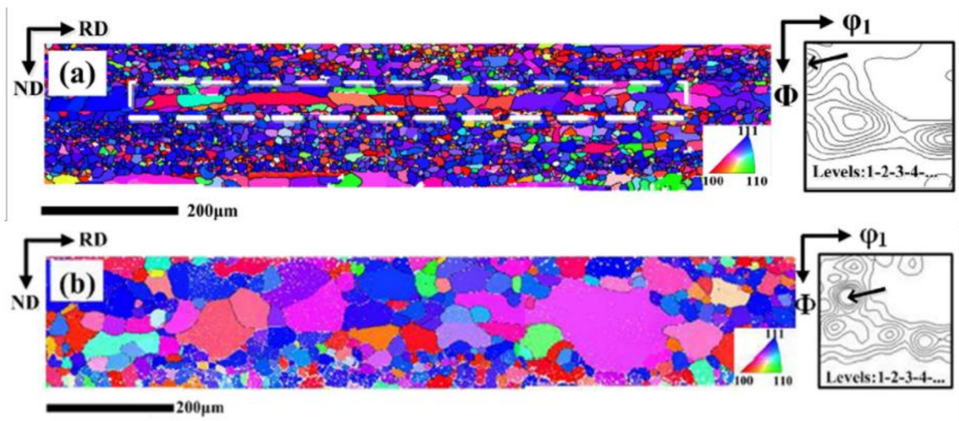

Figure 2.12: Microstructure and associated crystallographic orientations showing incomplete recrystallized grain structure during (a) primary recrystallization annealing, hindering the abnormal grain growth process during (b) secondary recrystallization annealing (Wang, Xu, Zhang, Fang, Lu, Misra, et al. 2015)

2.2.6 Secondary Recrystallization Annealing

Secondary recrystallized microstructure

The final high temperature annealing is performed under dry hydrogen atmospheric conditions above 900° C after completing the primary recrystallization step. The grain growth among secondary recrystallized grains depends up on the primary recrystallized microstructure and distribution of special grain boundaries (Park et al. 2002). The microstructure during secondary recrystallization annealing is recognized by abnormal growth of the selected grains. A typical example of an interrupted secondary recrystallized microstructure representing abnormal grain growth is shown in **Fig. 2.13**. It was reported that abnormal grain growth is preferred in the grains having size advantage over the other grains (Hillert 1965). However, it was also shown that grain having larger size usually grow slower compared to the other grains which are relatively smaller in size (Srolovitz et al. 1985).

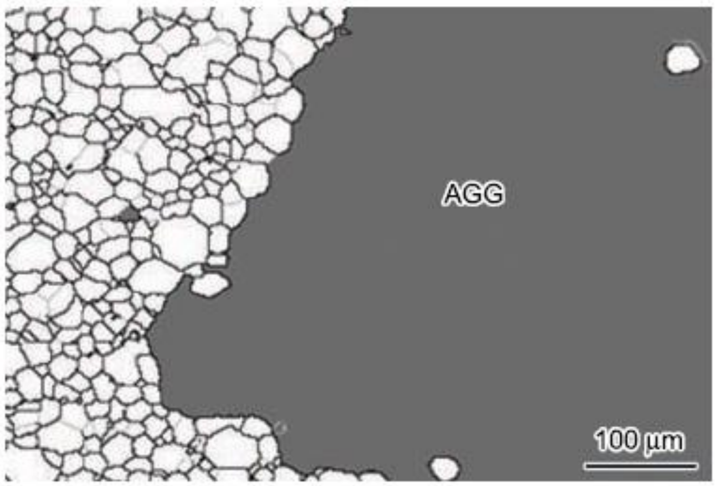

Figure 2.13: Microstructure after secondary recrystallization annealing which was interrupted to show abnormal gain growth (AGG) (Guo et al. 2010)

Abnormal grain growth of Goss oriented grains

The development of secondary recrystallized grains is dependent up on the primary recrystallized microstructure and crystallographic texture (Hayakawa 2017). The abnormal growth of Goss oriented grains during secondary recrystallization is well known. Goss oriented grains have the tendency to outgrow other grains in the surrounding matrix of the primary recrystallized structure. The size of final Goss oriented grains affects the magnetic properties of CRGO steel. The relation between core loss and final grain size is shown in **Fig. 2.14**. The Goss oriented grains, acting as a potential nuclei for abnormal grain growth, were reported to exist among the grain colonies which were developed around the surface and sub-surface layers of the primary annealed sheet (INOKUTI 1984, Inokuti 1996, Harase

1992). A schematic of secondary recrystallization process is shown in **Fig. 2.15** demonstrating that the development of Goss texture by abnormal grain growth occurred near the surface regions. However, in contrast to the above studies, several authors demonstrated that grain size and/or the presence of colonies of Goss oriented grains were not an essential condition for abnormal grain growth, rather it was achieved by certain growth advantages (Pease et al. 1981, Harase et al. 1988, Chen et al. 2003, Y Hayakawa et al. 1997).

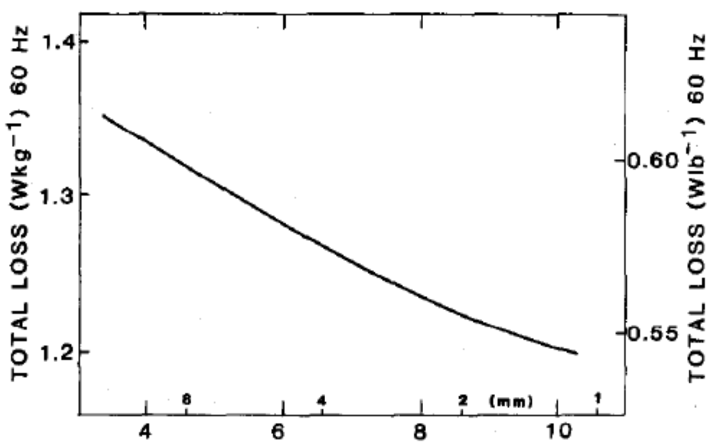

Figure 2.14: The values of total loss based on the size of final Goss oriented grains after secondary recrystallization (Littman 1982)

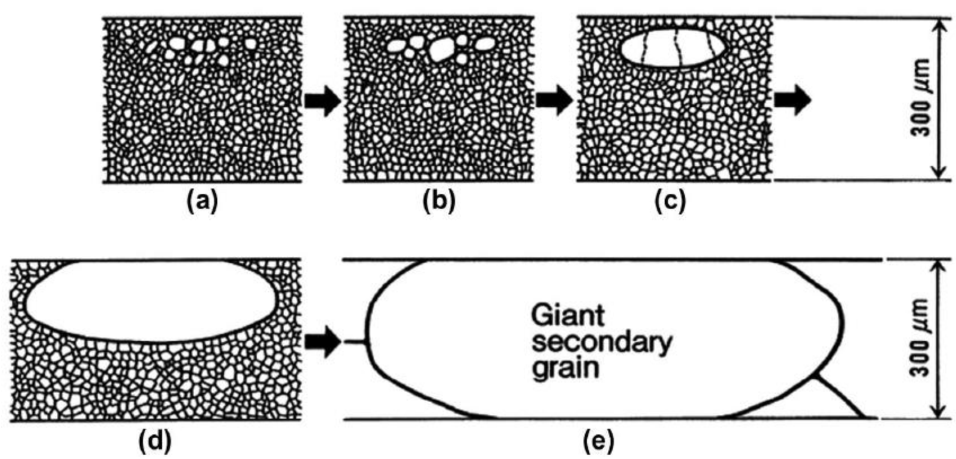

Figure 2.15: Schematic diagram of secondary recrystallization process showing the nucleation starts at surface layers leading to abnormal grain growth (Inokuti 1996)

Role of grain boundary character in the growth of Goss oriented grains

Numerous studies were conducted on the growth selectivity of Goss oriented grains during secondary recrystallization annealing. It was suggested that the growth of Goss oriented grains was controlled by either high grain boundary mobility or low grain boundary energy (Abbruzzese et al. 1992). The fraction of high energy (HE) grain boundaries having high misorientation angle between 20° - 45° was reported to be highest around Goss oriented primary grains (Y. Hayakawa et al. 1997, Hayakawa et al. 1998, Rajmohan et al. 2001). An experimental data showing the distribution of misorientation angle of grain boundaries around the overall primary recrystallized grains having Goss, main and average orientations is given in **Fig. 2.16**. A model was also proposed using Monte-Carlo simulations which demonstrated that the HE grain boundaries having misorientation angle between 20° - 45° were highly mobile (Y Hayakawa et al. 1997). These HE grain boundaries have high diffusivity and high migration rate which can explain the selective growth of Goss oriented grains (Omura et al. 2013).

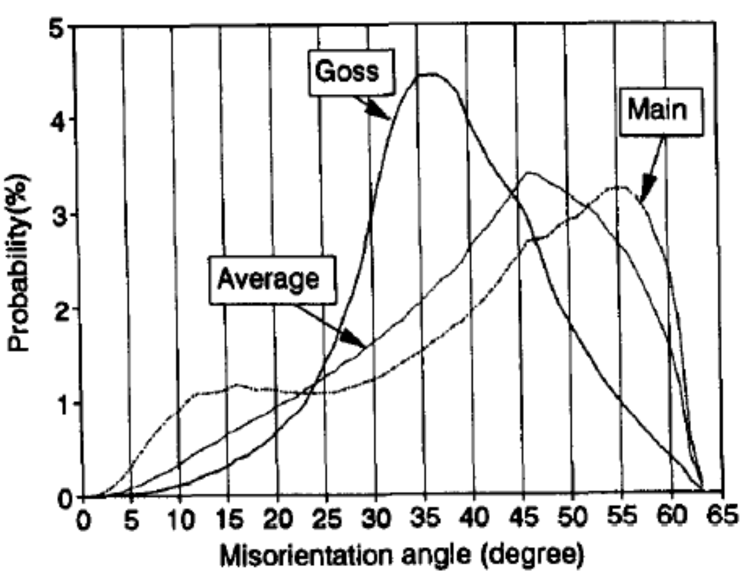

Figure 2.16: The distribution of grain boundaries based on misorientation angle around Goss, main and average orientations developed in the primary recrystallized structure (Y. Hayakawa et al. 1997)

On the other hand, the low Coincidence Site Lattice (CSL) boundaries Σ3 – Σ9 having low energy are free from imperfections which can also promote high migration rate compared to the other grain boundaries (Lin et al. 1996). In particular, it was shown that the presence of either Σ9 (Harase 1992) or Σ5 (Gangli et al. 1994), type CSL boundaries around the Goss oriented grains can explain the abnormal grain growth during secondary recrystallization. It was also reported that Σ9 type CSL boundaries have higher migration rate than the Σ5 type boundaries (Kumano et al. 2002, Kumano et al. 2003b, Kumano et al. 2003a). However, different kinds of CSL boundaries can develop around Goss oriented grains. A microstructure after primary recrystallization representing the presence of Σ3 – Σ51 CSL boundaries in the vicinity of grains having Goss orientation is shown in **Fig. 2.17**. Moreover, it was shown that the fraction of CSL boundaries surrounding Goss oriented primary grains were highly low (Rajmohan, J. A. Szpunar, et al. 1999). It was also demonstrated that the prediction of secondary recrystallization, by considering Σ1 – Σ51 CSL boundaries, does not lead to abnormal grain growth (Rajmohan, J. . Szpunar, et al. 1999). Broadly, the crystallographic orientations of the neighboring grains play an important role in generating the necessary grain boundary character to facilitate abnormal grain growth of Goss oriented grains. However, the conflicting reports do not confirm about the type of grain boundaries which promote abnormal grain growth. Most importantly, the existing literature could not address why only Goss grains have the growth advantage.

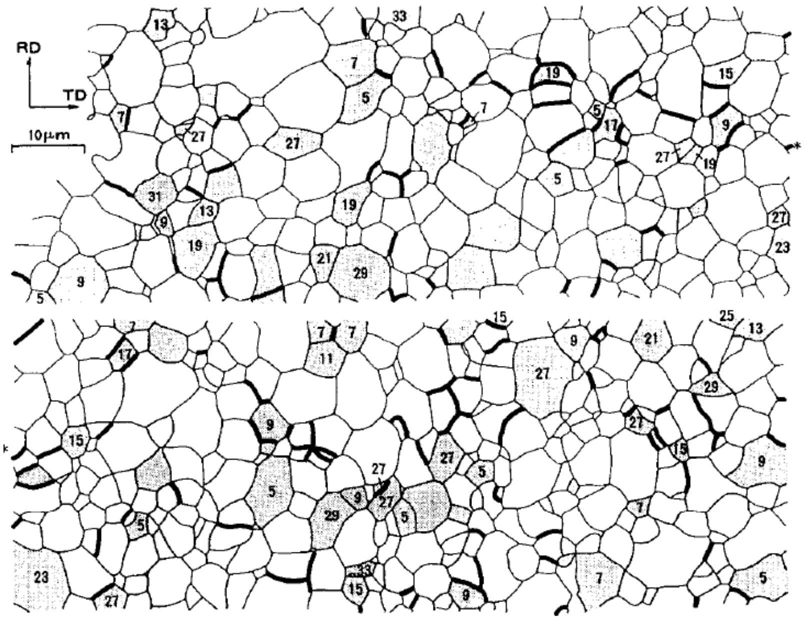

Figure 2.17: A primary recrystallized microstructure showing the formation of different kind of CSL boundaries (Σ3 – Σ51) in the vicinity of Goss oriented grains (Shimizu et al. 1989)

Role of inhibitors during secondary recrystallization annealing

The inhibitors such as, MnS and AlN, play a crucial role in establishing favorable conditions for abnormal grain growth by inhibiting the normal grain growth of other matrix grains (MATSUOKA 1967). In general, the abnormal grain growth is driven by the coarsening of precipitates which promote weak pinning force at the grain boundaries (Swift 1973). The coarsening of precipitates at high energy grain boundaries can further ease the pinning effect (Guo et al. 2010, Rajmohan et al. 2000). A schematic demonstrating the pinning forces around a growing secondary recrystallized grain is shown in **Fig. 2.18**. The interaction between the inhibitors and high energy grain boundaries (having misorientation angle between 20° - 45°) can produce high mobility which leads to the selective growth of Goss oriented grains during secondary recrystallization. However, it was also reported that in the presence of inhibitors, the low energy grain boundaries were less dragged compared to other boundaries which can induce high migration rate (Harase et al. 1991, Shimizu et al.

1989). The intensity of inhibitors around low energy grain boundaries (low CSL boundaries) can change the course of growth selectivity of Goss oriented grains. The driving force for grain growth is the reduction in grain boundary energy. It was shown that the balance between driving force and pinning force is also crucial in explaining the abnormal grain growth (Maazi et al. 2006). The inhibitors such as, Al_2O_3, are not desirable due to high stability of those precipitates which can develop high pinning force at the grain boundaries and impede the secondary recrystallization process (Hayakawa 2017).

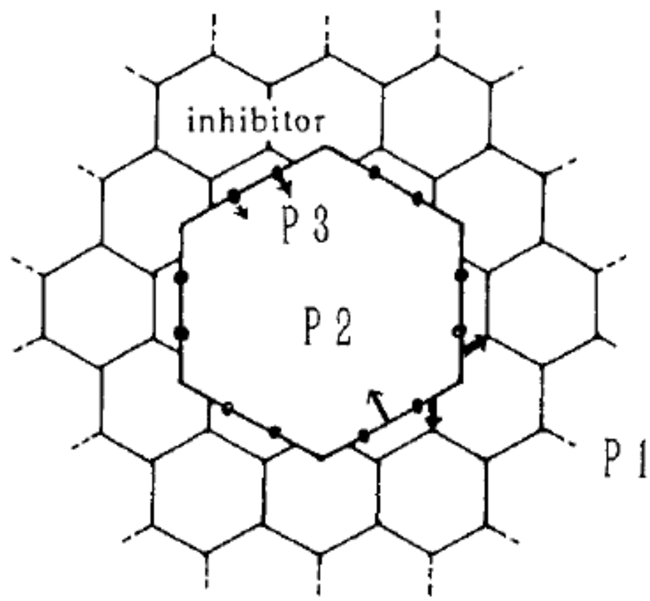

Figure 2.18: A schematic showing pinning forces by the inhibitors around a growing secondary recrystallized grain (Ushigami et al. 1998)

2.3 On the origin of Goss texture in CRGO steel

2.3.1 Goss orientation in the hot rolling stage

The source of Goss orientation in CRGO steel is a matter of debate for last few decades. It was reported that the Goss oriented grains formed at the surface regions during hot rolling, grow later during the primary and secondary recrystallization stages due to 'texture inheritance' (Mishra et al. 1986, Shimizu et al. 1986, Böttcher et al. 1993, Matsuo et al. 1986, Inokuti 1996). A schematic representing the inheritance of Goss orientation from hot rolling to primary recrystallization stage is shown in **Fig. 2.19**. It was demonstrated that the removal of the critical surface layers of the hot rolled plate leads to unfinished secondary recrystallization (Böttcher et al. 1993, Mishra et al. 1986). The Goss oriented grains were shown to be highly stable under shear stresses which usually prevails at the surface regions during hot rolling (HASHIMOTO 1988). The slip rotation under high shear deformation at surface and sub-surface layers during hot rolling was reported to promote the formation of Goss oriented grains (Shimizu et al. 1986).

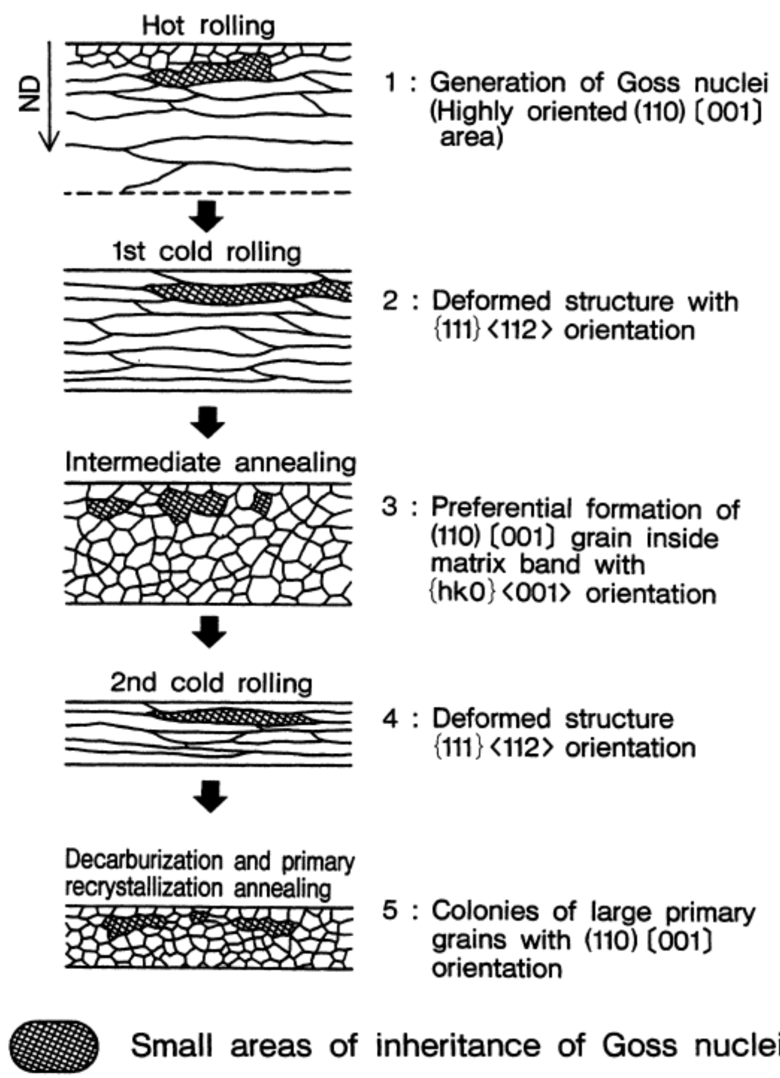

Figure 2.19: A schematic diagram showing inheritance of Goss orientation from hot rolling to primary recrystallization stage (Inokuti 1996)

Dorner et al. (Dorner et al. 2007) investigated the importance of Goss oriented grains formed during hot rolling. Cold rolling was performed on single Goss oriented grain which was selected from surface regions of the hot rolled plate. Two kinds of deformed structure were developed during cold rolling, shear bands and microbands. The initial Goss orientation was observed to retain in both shear bands and microbands. However, it was demonstrated that the Goss oriented grains inside microbands were stable and subsequently significant during primary and secondary recrystallization processes. On the other hand, Giri et al. (Giri et al. 2020) suggested that the formation of Goss oriented grains during hot rolling occurred due to dynamic recrystallization by particle stimulated nucleation in the ferrite phase.

2.3.2 Goss orientation in the cold rolling stage

Studies were also conducted to understand the formation of Goss oriented grains by performing cold rolling on single crystals having $\{111\}\langle 112\rangle$ orientation. It was reported that the Goss texture during primary and secondary recrystallization stages developed from the shear band regions which formed during cold rolling inside γ-fiber texture component ($\{111\}\langle 112\rangle$) (T Haratani et al. 1984, Ushioda et al. 1989). The importance of shear bands during cold rolling in polycrystalline CRGO steels was also shown by some researchers (I Samajdar et al. 1998, Park et al. 2003, Lee et al. 2018). However, the observations were mostly made with the help of partial recrystallization technique and no direct evidence was provided about the formation of Goss oriented grains inside shear bands. On the other hand, similar study demonstrated that the Goss oriented grains can form at three different locations in the cold rolling structure such as, along shear bands and microbands of $\{111\}\langle 112\rangle$, and at the grain boundaries of $\{111\}\langle 112\rangle$ and $\{113\}\langle 361\rangle$ (Mehdi et al. 2019). Furthermore, it was also shown that the Goss texture during primary recrystallization annealing independently developed from the cold rolled sheet irrespective of the presence of Goss orientation prior to cold rolling

(Heo et al. 1999). The γ-fiber crystallographic texture is a typical cold rolling texture. The Goss oriented grains evolved during subsequent primary recrystallization annealing, were reported to be related to the γ-fiber texture components formed at the surface regions of the cold rolled sheet (Zhang et al. 2021). The intensity of Goss orientation through the thickness of the primary recrystallized sheet is shown in **Fig. 2.20**.

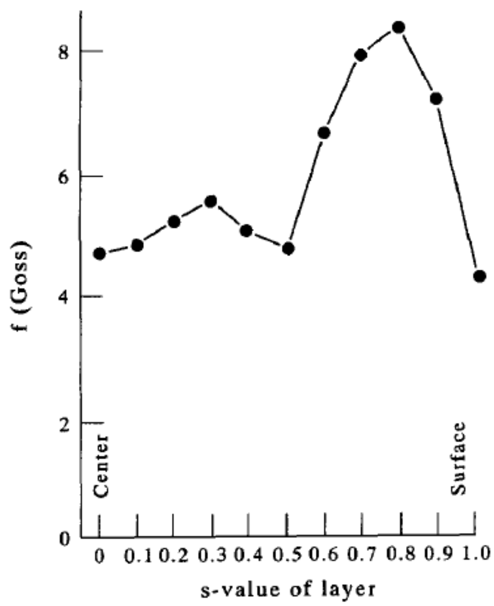

Figure 2.20: The intensity of Goss orientation through the thickness of the primary recrystallized sheet (Böttcher et al. 1993)

2.4 Cold rolling defects

The mechanical behavior of steels can change the loading conditions which affects the process of deformation. The microstructural features such as, grain morphology and inclusions, can lead to change in the mechanical properties of steels. Various kinds of defects may develop during cold rolling as shown in **Fig. 2.21**. The edge crack is a common cold rolling defect which generally occurs due to high brittleness of the material (Barlow et al. 1984, Samei et al. 2019). These edge cracks are either trimmed off before continuing the cold rolling process or various annealing treatments are utilized to increase the ductility of the material. A study on non-oriented electrical steel showed that the edge crack developed in intergranular fashion due to presence of oxide inclusions at the grain boundary(Han et al. 1999). Another study demonstrated that the edge cracks in high silicon CRGO steel, having silicon content more than 3 wt.%, propagated in ductile manner (Byon et al. 2021). Alligator cracking phenomenon has also been observed to develop during cold rolling in different varieties of steels (Xu et al. 1994, Kim et al. 2013). However, the reasons behind the development of alligator crack in CRGO steel during cold rolling has been rarely reported.

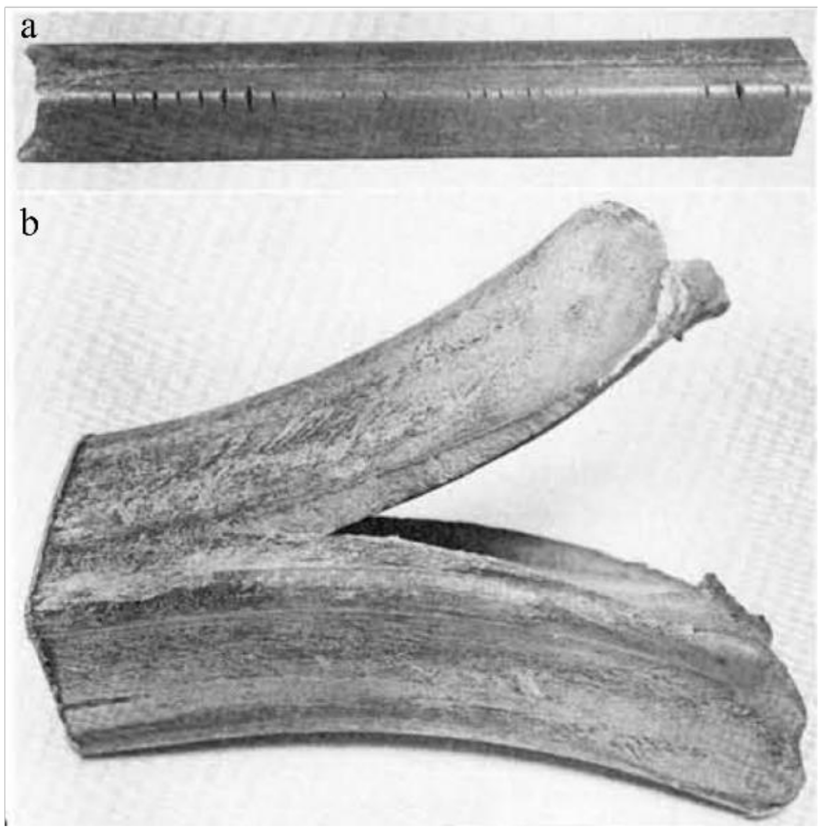

Figure 2.21: Defects formed during cold rolling, (a) edge cracks, and (b) alligator crack (Barlow et al. 1984)

2.4.1 Effect of silicon on mechanical behavior during cold rolling

It is well known that increasing the silicon content improves magnetic behavior of CRGO steel (Haiji et al. 1996, C.-K. Hou 1996, Heo et al. 1999, Turner et al. 2010). The measured values of core loss vs silicon content is shown in **Fig. 2.22**. However, higher silicon addition in Fe-Si steel develops other microstructural heterogeneities which may lead to unsuccessful thermo-mechanical processing. Silicon produces a substitutional solid solution in bcc-iron which provide strengthening to Fe-Si alloy. The addition of silicon also increases the ductile to brittle transition temperature (Gerberich et al. 1981). The room temperature ductility decreases on increasing the silicon concentration and as a consequence, high silicon content greater than 3 wt.% can induce brittleness. Moreover, different ordered phases such as, B2 and $D0_3$, starts to develop on exceeding the silicon content above 5 wt.% (Ouyang et al. 2019) (**Fig. 2.1**), which further reduces the ductility of Fe-Si alloy.

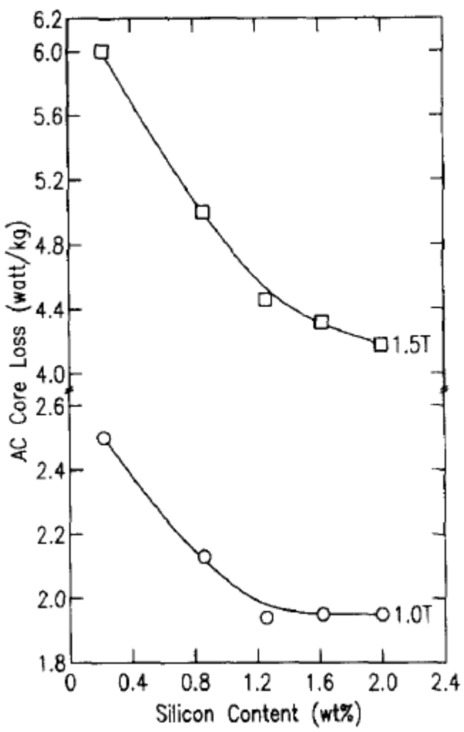

Figure 2.22: Effect of silicon concentration on core losses (C.-K. Hou 1996)

2.4.2 Effect of crystallographic texture during cold rolling

Crystallographic texture can also induce anisotropy in the mechanical properties of steels. The strain incompatibility between various crystallographic orientations can affect the formability and ductility during cold rolling. The grain orientations then become vital in generating different kinds of defects during cold rolling deformation. Some works have been reported which correlated the crack analysis in low carbon steel with the crystallographic texture (Ghosh et al. 2014, Ghosh et al. 2016). It was shown that the cube texture has its rolling plane parallel to $\{001\}$ cleavage plane which provided easy path for crack to propagate in cleavage fashion. Mainly, the studies on the formation of cold rolling defects in electrical steels were confined to microstructural parameters such as, grain size and inclusions. The role of crystallographic texture in the development of various cold rolling cracks in CRGO steel was rarely reported.

2.5 Summary

The above literature review clearly shows that various processing methods have been incorporated to produce Goss texture and thereby improve the magnetic properties of CRGO steel. However, the complete process of CRGO steel showing the microstructure and texture development at different stages is rarely reported. The most important aspect of CRGO steel is the formation of large Goss oriented grains at the end of the process and critical understanding on the source of the Goss texture is ambiguous. On the other hand, it was reported that higher silicon content further improves the magnetic properties of CRGO steel. However, it is difficult to process high silicon CRGO steel and the addition of high silicon can lead to variation in the microstructure and texture evolution.

CHAPTER 3

Experimental and Computational Details

3.1 Chemical Composition of CRGO Steel

The composition of the steel was carefully selected after a detailed thermodynamic analysis. Initially, the role of different alloying elements such as C, Si, Mn, and Al, on the overall phase evolution has been explored by predicting different phase diagrams using Thermo-Calc database as shown in **Fig. 3.1(a-f)**.

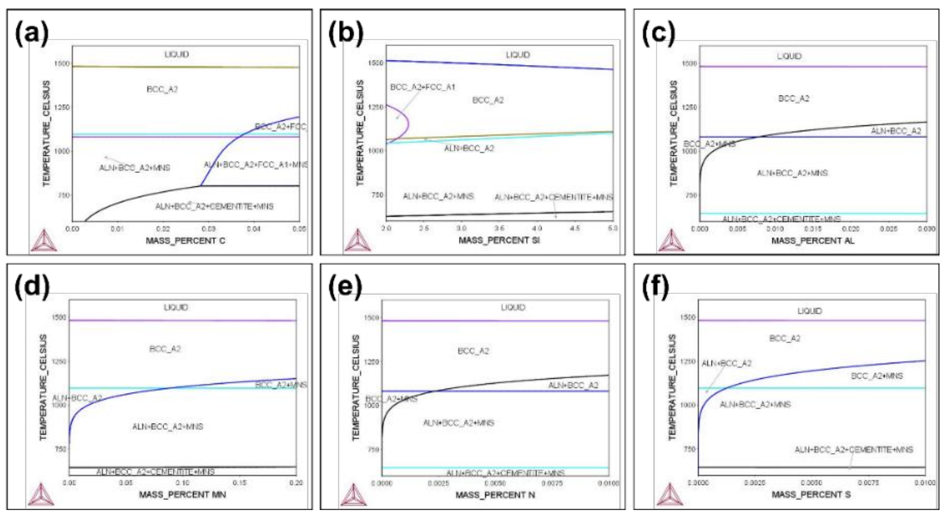

Figure 3.1: Phase diagrams predicted using thermodynamic database for (a) Fe-C, (b) Fe-Si, (c) Fe-Al, (d) Fe-Mn, (e) Fe-N, (f) Fe-S

The concentration of other alloying elements was kept constant while drawing the phase diagram with respect to one alloying element. For example, in Fe-Si phase diagram shown in **Fig 3.1(b)**, the wt. % of C, Mn, Al, N, and S were kept at constant values of 0.005, 0.07, 0.01, 0.003 and 0.001, respectively. In order to ensure the stability of ferrite phase throughout the phase space of an Fe alloy where the amount of C was around 0.002 wt. %, the Si concentration need not to be less than 2.5 wt. %, **Fig. 3.1(a, b)**. The composition was chosen in such a way that the formation of austenite phase was restricted. In addition, the dissolution temperature of the inhibitors such as, AIN and MnS, was tried to keep less than 1473 K, **Fig. 3.1(a-f)**. The concentration of the other chemical elements like S and N was also kept below a safe limit.

3.2 Processing of CRGO steel

3.2.1 Casting and Homogenization

With the optimized nominal composition, three cast products were melted using Vacuum Induction Melting (VIM) furnace of 60 kg capacity located in the Investment casting shop (ICP) of M/s Mishra Dhatu Nigam Limited (MIDHANI), Hyderabad. The actual composition of three melted alloys, which were named as HSI, MSI and LSI, is given in **Table 3.1**. The steel ingots were divided into several parts with dimensions 100 x 70 x 45 mm which were first subjected to reheating at 1200° C for 60 minutes to ensure homogenization of the structure. The development of extremely large grains after reheating, having grain size up to roughly 5 mm, are shown in the macrograph in **Fig. 3.2**.

Table 3.1: Chemical composition of CRGO steels (wt. %)

Element	Sample Names		
	HSI	MSI	LSI
C	0.0095	0.0024	0.004
Si	3.78	3.23	2.98
Mn	0.26	0.143	0.01
Al	0.002	0.002	0.01
S	0.002	0.003	0.001
N	0.0008	0.0021	0.0009
P	0.008	0.008	0.008
Fe	Balance		

Figure 3.2: Macrostructure after reheating at 1200° C for 60 minutes

3.2.2 Rolling Processes

Different rolling processes and in-between heat treatment steps for HSI composition involved in the present study are shown in the schematic in **Fig. 3.3**. Hot Rolling (HR) was performed to reduce 45 mm thick reheated slab down to 8 mm thick plate in multi-pass in the temperature range of 1200° C to 750° C achieving 1.72 true strain. There was a limitation to reduce the thickness of the plate below 1.5 mm in the laboratory scale cold rolling setup. Therefore, to achieve cold rolling strain similar to the industrial cold rolling process, HR was terminated after reaching 8 mm thickness. Cold rolling was conducted directly after HR without providing any prior annealing treatment and severe edge cracks were developed after reaching thickness of around 5.5 mm. During another schedule, the hot rolled plate was given Hot Band Annealing (HBA) treatment at 800° C temperature for 30 minutes in air before conducting cold rolling. The 8 mm thick annealed plate was cold rolled down to 1.5 mm thick sheet during Single stage Cold Rolling (SCR) in multi-passes corresponding to 1.67 true strain along thickness. However, the alligator crack also developed at one end of the cold rolled sheet. During the cold rolling process, sample was also collected after the reduction of 8 mm thick annealed plate to 3.5 mm achieving 0.82 true strain, which is named as Intermediate Cold Rolling (ICR). Separately, the intermediate cold rolled sample was subjected to Intermediate Annealing (IA) treatment at 800° C for 30 minutes in air. Subsequently, the cold rolling process was then completed (named as Complete Cold Rolling (CCR)) by reducing 3.5 mm thick intermediate annealed plate to 1.5 mm attaining 0.84 true strain. The modified schedule was successful in producing 1.5 mm thick cold rolled sheet without any defects. The details of the hot rolling and cold rolling processes for HSI composition are shown in **Table 3.2**.

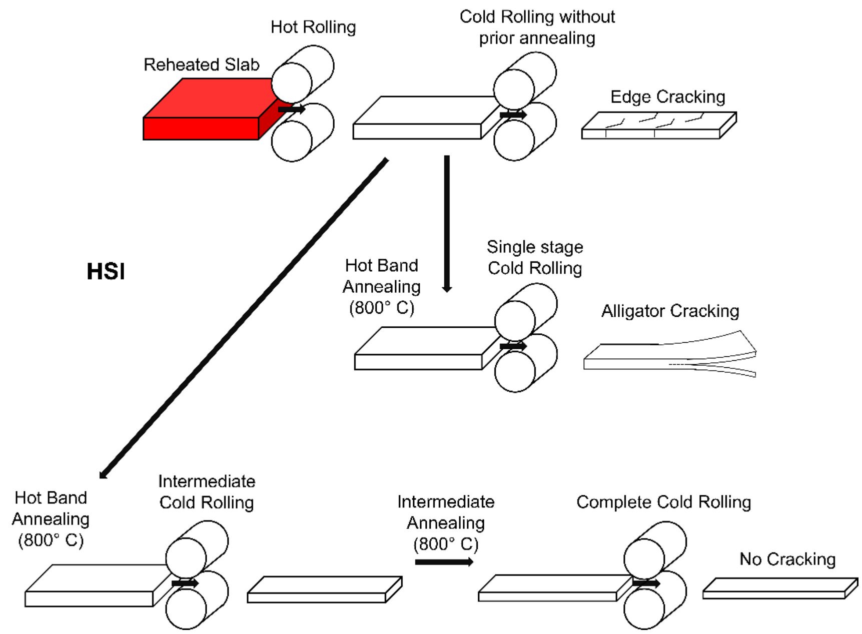

Figure 3.3: Schematic representation of the hot and cold rolling processes for HSI composition along with in-between heat treatment steps involved in the present study

Table 3.2: Hot and cold rolling process details for HSI composition

Process	Thickness Reduction (mm)	Temperature (° C)	Reduction (%)	True Strain (ε)
Hot Rolling				
After 1st pass	45 to 31.42	1200 to 1127	30.18	0.35
After 2nd pass	31.42 to 20	1127 to 985	36.34	0.45
After 3rd pass	20 to 8	985 to 750	61	0.91
Total Hot Rolling True Strain = 1.71				
Cold Rolling				
Directly after hot rolling in single stage	8 to 5.5 *(Edge cracks)*	Room Temperature	31.25	0.37
Single stage after hot band annealing	8 to 1.5 *(Alligator crack)*	Room Temperature	81.25	1.67
Intermediate stage after	8 to 3.5	Room Temperature	56.25	0.82

hot band annealing				
Completion stage after intermediate annealing	3.5 to 1.5 *(No cracks)*	Room Temperature	57.14	0.85

Similarly, different rolling processes and in-between heat treatment steps for MSI and LSI compositions are shown in the schematic in **Fig. 3.4**. Unlike HSI, all the rolling operations for MSI and LSI were successful in producing a thin cold rolled sheet without developing any kind of cracks. The hot rolling and cold rolling details for MSI and LSI compositions are listed in **Table 3.3** and **Table 3.4**, respectively.

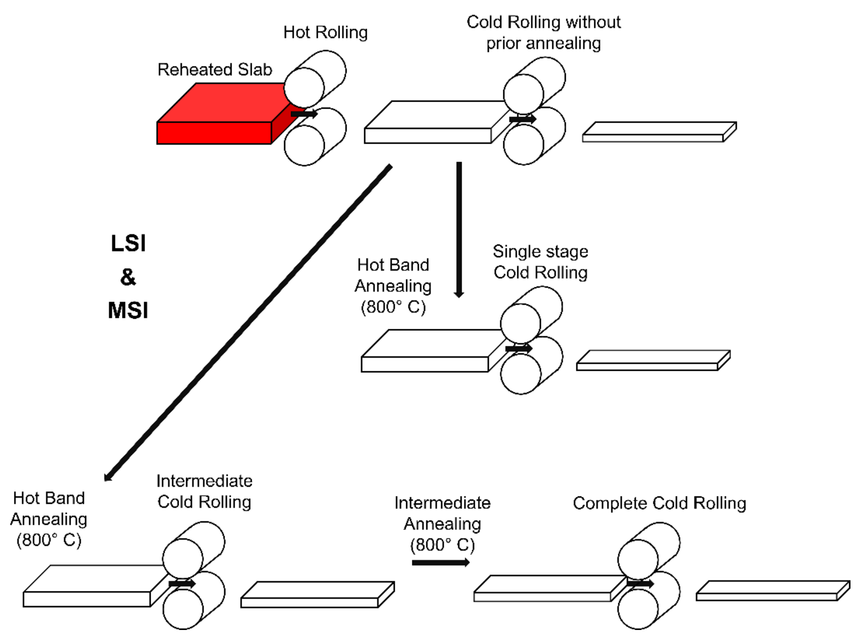

Figure 3.4: Schematic representation of the hot and cold rolling processes for MSI and LSI compositions along with in-between heat treatment steps involved in the present study

Table 3.3: Hot and cold rolling process details for MSI composition

Process	Thickness Reduction (mm)	Temperature (° C)	Reduction (%)	True Strain (ε)
Hot Rolling				
After 1st pass	45 to 33	1200 to 1022	26.66	0.31

After 2nd pass	33 to 19.5	1022 to 933	40.90	0.52
After 3rd pass	19.5 to 8.25	933 to 730	57.69	0.84
Total Hot Rolling True Strain = 1.67				
Cold Rolling				
Directly after hot rolling in single stage	8.25 to 1.5	Room Temperature	81.81	1.70
Single stage after hot band annealing	8.25 to 1.3	Room Temperature	84.24	1.84
Intermediate stage after hot band annealing	8.25 to 5	Room Temperature	39.39	0.50
Completion stage after intermediate annealing	5 to 1.4	Room Temperature	72.00	1.27

Table 3.4: Hot and cold rolling process details for LSI composition

Process	Thickness Reduction (mm)	Temperature (° C)	Reduction (%)	True Strain (ε)
Hot Rolling				
After 1st pass	45 to 31	1200 to 1120	31.11	0.37
After 2nd pass	31 to 20	1120 to 1000	35.48	0.44
After 3rd pass	20 to 8	1000 to 750	60	0.91
Total Hot Rolling True Strain = 1.72				
Cold Rolling				
Directly after hot rolling in single stage	8 to 1.5	Room Temperature	81.25	1.67
Single stage after hot band annealing	8 to 1.5	Room Temperature	81.25	1.67
Intermediate stage after	8 to 3.1	Room Temperature	61.25	0.95

hot band annealing				
Completion stage after intermediate annealing	3.1 to 1.35	Room Temperature	56.45	0.83

3.2.3 Typical Process of CRGO steel

The single stage cold rolled samples after hot band annealing were considered for the final two stage annealing steps in the processing of CRGO steel. Primary recrystallization annealing was attempted between the range of 550-700° C temperatures under air atmosphere. Subsequently, the secondary recrystallization annealing was performed between temperatures 900-1200° C under vacuum on the selected primary recrystallized samples. Temperature vs time representation of a typical process of CRGO steel is shown in the processing schematic in **Fig. 3.5**. Air cooling was incorporated after each heat treatment step throughout the process.

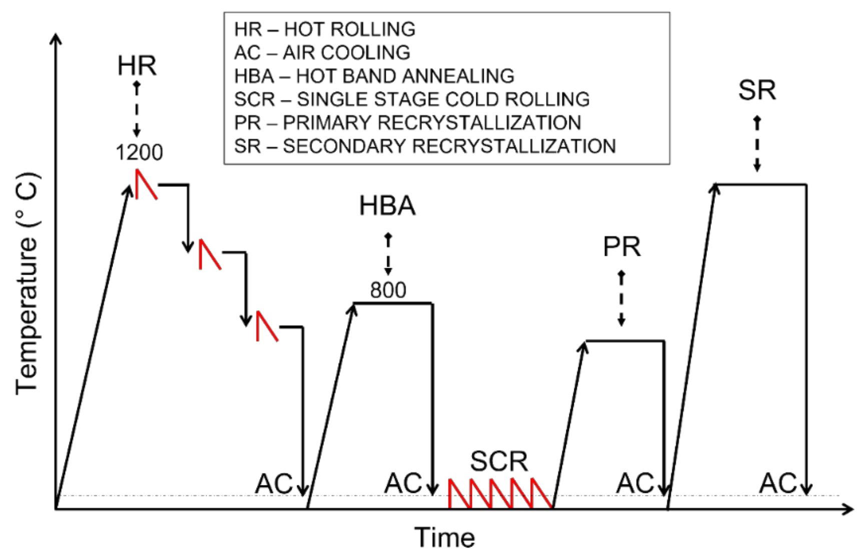

Figure 3.5: Temperature vs time representation showing typical process of CRGO steel

3.3 Characterization techniques

3.3.1 Differential Scanning Calorimetry

Differential scanning Calorimetry (DSC) test was employed using STA8000 model by Perkin Elmer to examine the phase transformations and formation of precipitates during heating and cooling cycle at the rate of 5° C/min.

3.3.2 Microstructure and Microtexture Characterization

The microstructural study of both the compositions, HSI and LSI, has been carried out through Optical Microscopy (OM), Field Emission Scanning Electron Microscopy (FESEM) and Transmission electron microscopy. The specimens were collected after different rolling and heat treatment steps during the process from RD-ND longitudinal section (yellow color) as shown in **Fig. 3.6**. The preparation of specimens for OM and FESEM analysis was done by following a standard metallographic procedure. After sufficient grinding and fine polishing, the specimens were etched using 2-4% nital solution (98-96% ethanol and 2-4% nitric acid, respectively). ZEISS inverted OM and JSM-7610FPlus FESEM with Energy Dispersive Spectroscopic (EDS) technique was utilized to examine the microstructure.

The specimens collected from Rolling Direction (RD)-Normal Direction (ND) longitudinal sections (yellow color) after various steps in the processing were also analyzed using Electron Backscatter Diffraction (EBSD) technique, **Fig. 3.6**. The preparation of specimens for EBSD analysis was done by polishing down to 3-4 µm diamond finish which was followed by final polishing with 0.5 µm colloidal silica solution. The EBSD attachment with JSM-7610FPlus FESEM was used for EBSD scans which were performed at 70° pre-tilt condition. The scanning areas vary from minimum of 5 µm x 5 µm to maximum of 1000 µm x 4000 µm along ND-RD longitudinal section at varying step sizes in the range of 50 nm to 3 µm depending up on the specimen thickness and requirement. The post-processing maps were generated with the help of MTex toolbox in MATLAB software which includes Band Contrast maps, Inverse Pole Figure (IPF) maps, Orientation Distribution Function (ODF) maps, Taylor Factor maps and Grain Orientation Spread (GOS) maps. EBSD data was also used for the grain size distribution, boundary curvature and grain boundary analysis based on misorientation angle boundaries and Coincidence Site Lattice (CSL) boundaries via MTex toolbox.

Transmission electron microscopic analysis has been carried out under JEOL JEM 2200FS model TEM operated at 200 kV. Thin foils were prepared by cutting thin wafers from the steel samples and polishing them down to ~70 μm thickness. Further, 3 mm diameter disks were punched from the foils and electropolished using 10% perchloric acid and 90 % acetic acid solution.

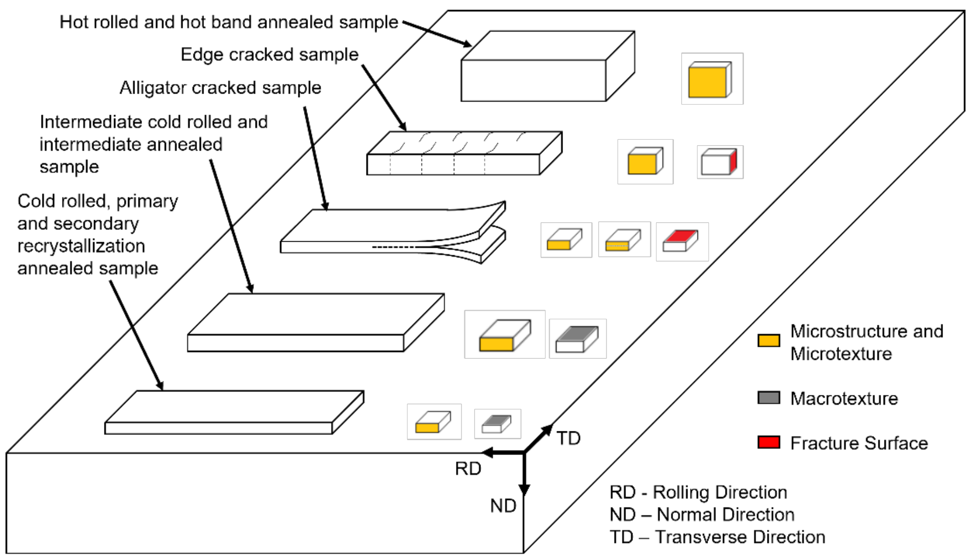

Figure 3.6: Schematic representation of specimens collected from samples after different processing and heat treatment steps for microstructure and microtexture study (yellow color), macrotexture study (gray color) and fractographic study (red color)

3.3.3 Macrotexture Analysis

Macrotexture analysis was conducted after different cold rolling processes (ICR, CCR, and SCR) and intermediate annealing (IA) on quarter (1/4th) thickness on RD-Transverse Direction (TD) plane, **Fig. 3.6**, using Cu-Kα radiation in PANanalytical® empyrean x-ray diffractometer. The scanning was done at 5° step size in the range of ω = 0° to 360° (rotation around ND-axis) and ψ = 0° to 80° (rotation around RD-axis) for three non-planar crystallographic planes ({110}, {200}, and {211}) using three-axis goniometer. ODF maps were generated from the collected pole figures via MTex toolbox in MATLAB platform.

3.3.4 Microhardness Testing

Microhardness values were measured on ND-RD longitudinal section of selected samples after flattening upper and lower surfaces. The upper surface was further polished to mirror finish which followed by etching with 2-4% Nital solution. Microhardness test was carried out employing Vickers Microhardness testing machine manufactured by Micro-Mach Technologies (model MMV-A, series 131) under 0.3kg load using 1/16" diamond indenter. At least ten readings were taken through the thickness to determine the average microhardness.

3.3.5 Fractography

Fractographic study was conducted on ND-TD plane of edge cracked sample and RD-TD plane of alligator cracked sample, **Fig. 3.6**. Specimens were first immersed into ethanol followed by an ultrasonication to remove all the dust particles to conduct fractographic analysis under JSM-7610FPlus FESEM.

3.4 Computational techniques

3.4.1 Finite Element Method

Finite Element Method (FEM) was used to simulated rolling process using the ABAQUS Explicit solver considering 20% thickness reduction. The mass scaling factor was incorporated by keeping the ratio of kinetic energy and internal energy (KE/IE) to below 5%. In addition, the quarter symmetric model was considered to reduce the execution time. The roller part was considered as analytical rigid, and the boundary conditions applied during rolling simulation has been represented by the schematic in **Fig. 3.7**. General tangential contact with the isotropic coefficient of friction was employed between rollers and the plate during rolling simulation. The coefficient of friction between rollers and the plate (μ) was considered as

0.3 to avoid slipping of the plate under rollers for given thickness reduction of 20% in the present study as shown in **Fig. 3.7**.

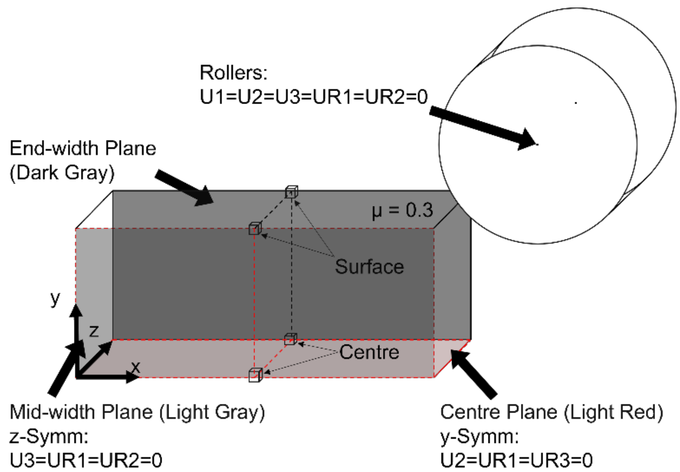

Figure 3.7: Schematic of the quarter symmetric steel part and analytical rigid roller created during rolling simulation showing the boundary conditions and coefficient of friction between rollers and the plate incorporated in the FEM study

3.4.2 Visco-plastic self-consistent simulations:

Visco-plastic self-consistent (VPSC) model is based on the mechanisms of crystal plasticity and integrates the deformation processes by slip and/or twinning. A detailed description of the VPSC formulation can be found elsewhere (Molinari et al. 1987, Lebensohn et al. 1993). Rate sensitivity law as shown in the equation (3.1) describes the visco-plastic constitutive behavior for a single grain.

$$\dot{\varepsilon}_{ij} = \sum_s m_{ij}^s \gamma^s = \dot{\gamma}_0 \sum_s m_{ij}^s \left(\frac{m_{kl}^s : \sigma_{kl}}{\tau^s}\right)^n \tag{3.1}$$

where, '$\dot{\varepsilon}_{ij}$' is a deviatoric strain-rate, 'σ_{kl}' is a deviatoric stress, 'γ^s' is the local shear-rate, 'm_{ij}^s' is the Schmid tensor associated with the slip and/or twinning systems and 'τ^s' is the threshold shear stress. 'n' is the inverse of rate sensitivity which has been considered as $n^{eff} = 10$ to achieve a realistic prediction corresponding to an interaction between lower and upper bound (Takajo et al. 2019). Also, the value of 's' represents slip and/or twinning systems among which {110}<111> and {112}<111> slip systems with same hardening parameters were considered to take part in the plastic deformation (Libovický 1971, Takeuchi et al. 1967, Takenaka et al. 2018a, Ushioda et al. 1989). The evolution of 'τ^s' can further be calculated by the voce hardening law (Hu et al. 2021, Sarkar et al. 2011) as shown in equation (3.2).

$$\tau^s = \tau_0^s + (\tau_1^s + \theta_1^s \Gamma)(1 - exp(-\Gamma \left|\frac{\theta_0^s}{\tau_1^s}\right|)) \tag{3.2}$$

Where, $\Gamma = \sum_s \Delta\gamma^s$ is the accumulated shear in a given grain, τ_0, (τ_0 + τ_1), θ_0, θ_1 are the initial Critical Resolved Shear Stress (CRSS), back-extrapolated CRSS, initial hardening rate and asymptotic hardening rate, respectively. Different voce hardening model parameters shown in **Tables 3.5, 3.6, 3.7** were used in the present investigation (Hu et al. 2021). In case I, equal initial CRSS of {110}<111> and {112}<111> slip systems were considered, **Table 3.5**, in case II 10% lower initial CRSS of {110}<111> slip system was used compared to {112}<111> slip system, **Table 3.6**, and in case III 20% lower CRSS of {110}<111> slip system was considered compared to {112}<111> slip system, **Table 3.7**. For simplicity, no latent hardening was considered.

Table 3.5: Voce Hardening Parameters of case I used in the present study

Voce Parameter	Value (MPa)
τ_0	2
τ_1	0
θ_0	1
θ_1	0

Table 3.6: Voce Hardening Parameters in case II used in the present study

Voce Parameter	Value (MPa)
τ_0	1.8
τ_1	0

θ_0	1
θ_1	0

Table 3.7: Voce Hardening Parameters in case III used in the present study

Voce Parameter	Value (MPa)
$\boldsymbol{\tau}_0$	1.6
$\boldsymbol{\tau}_1$	0
θ_0	1
θ_1	0

CHAPTER 4

Study on the formation of alligator crack and edge crack in high silicon cold rolled grain oriented steel during cold rolling

4.1 Introduction

CRGO steel is known for producing low magnetic losses when used in the transformer core as thin (<0.5 mm) laminated sheets (Lin et al. 1995). In order to achieve better electrical and magnetic properties, high concentration of Si in CRGO steel is desired (Haiji et al. 1996, C.-K. Hou 1996, Heo et al. 1999, Turner et al. 2010). Addition of silicon induces solid solution strengthening in iron. Beside that Si addition decreases the overall fracture stress and increases the ductile to brittle transition temperature (Gerberich et al. 1981). As a result, room temperature ductility is greatly affected with an increase in the Si content. On the other hand, ordered phases such as B2 and $D0_3$ evolve if the Si content is more than 5 wt. % (Ouyang et al. 2019). The presence of antiphase boundaries in ordered phases restricts the dislocation motion and reduces ductility. In general, the increase in the amount of Si content more than 3 wt. % can promote brittleness (Qiao et al. 2003, Hughes et al. 2005, Sorbello et al. 2009, Nakanishi et al. 2016) which often reduces the chance of successful thermo-mechanical operations. A thin (<2 mm) cold rolled sheet then becomes extremely challenging to produce.

The brittle nature of high Si CRGO steel may promote the formation of different types of cracks during the cold rolling process such as alligator crack and edge crack. Although, the formation of alligator crack was observed in different varieties of steel (Kim et al. 2013, Xu et al. 1994), no study has been focused on the development of alligator crack in CRGO steels so far. Defects such as porosities and segregation during the casting of steel were reported to occur, which contributed to the formation of crack at the mid-thickness region or center (Ghosh 2001, Bode et al. 2008, Réger et al. 2010, Miyazaki et al. 2013). Some authors have also shown that low Mn/S ratio and high carbon content leading to the formation of second phases could be the reason for the occurrence of centerline crack during the rolling process (Pandey et al. 2009, D. Bhattacharya et al. 2016). High concentration of Mn was generally reported to be responsible for centerline defects that later produce cracks during rolling (Kim et al. 2013, D. Bhattacharya et al. 2016). Higher sulfur content was also reported to lead off-centre segregation producing cracks at regions other than centerline (Diptak Bhattacharya et al. 2016). Kim et al. (Kim et al. 2013) have shown that during hot rolling of free machining steel, the alligator crack occurs due to microcracks developing around MnS inclusions. They have demonstrated that the increase in grain size of ferrite can promote discontinuous distribution of MnS inclusions, which restrict the growth of cracks. However, large grain size is not desired as it decreases the cleavage fracture stress (Joo et al. 2012, Ghosh et al. 2014). Xu et al. (Xu et al. 1994) have reported that the formation of alligator crack during cold rolling of spheroidized steel was related to the development of voids. The study showed that shear and residual stresses present in the vicinity of voids resulted in ductile fracture during alligatoring. However, the study did not provide any demonstration on the nature of residual stresses acting in the normal direction during rolling. Barlow et al. (Barlow et al. 1976) have also reported that during groove rolling, high stress concentration at the central region may develop. Turczyn et al. (Turczyn et al. 1992) have used the rigid plastic Finite Element Method (FEM) approach to show the stress distribution during plane strain rolling. But apparently, the analytical stress states responsible for alligator crack formation during cold rolling have not been studied in detail.

Furthermore, edge cracking phenomenon is commonly found during cold rolling and the development of edge cracks was considerably studied on the various grades of steel (Barlow et al. 1984, Samei et al. 2019). Han et al. (Han et al. 1999) conducted their studies on the non-oriented silicon steel and showed that edge crack initiated at oxide inclusions and propagate in intergranular fashion from the surface to interior. Recently, Byon et al. (Byon et al. 2021) also demonstrated the formation of edge cracks in more than 3 wt. % Si steel considering the roll bending phenomenon. However, contrary to their report that edge cracking occurs in a ductile fashion, high Si content in CRGO steel is expected to induce brittleness. Various analytical studies based on FEM were conducted to simulate the cold rolling process of low silicon steel using the damage model, and mainly delineated that the edge cracking phenomenon takes place by the growth of voids leading to ductile fracture (Yan et al. 2013, Sun et al. 2015). Moreover, Zan et al. (Zan et al. 2017) considered the cohesive zone model during their FEM study and reported that when Von-Mises equivalent stress along the rolling direction (RD) exceeds the critical cohesive stress, it encourages the development of the edge crack at 45° to RD.

Most of the studies on the rolling defects were focused on the role of microstructural parameters such as grain size and inclusions. However, the role of crystallographic orientations, which can significantly influence the cracking phenomena has not been considered until date. The current investigation addresses the role of both microstructure and microtexture on the alligator and edge cracking during cold rolling of high Si CRGO steel. An attempt has also been made to understand the role of analytical stress state during the cold rolling process on the evolution of these cracks with the help of FEM-based simulation.

4.2 Edge crack and alligator crack

In CRGO steel having HSI composition, different schedules of rolling and heat treatments which lead to the development of those cracks and the modified schedule which was effective in eliminating the cracks are demonstrated in the schematic shown in **Fig. 4.1(a-c)**.

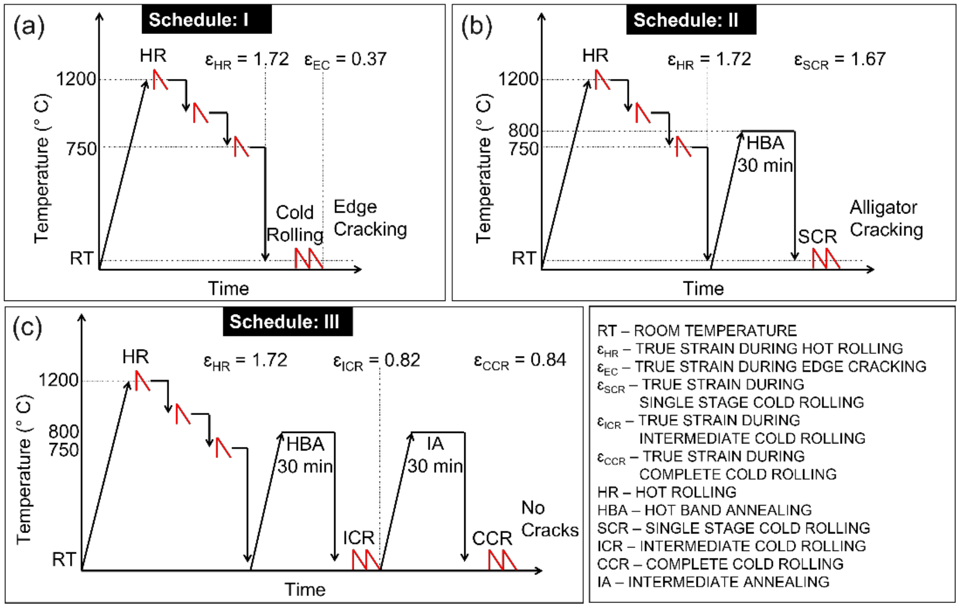

Figure 4.1: Schematic diagram showing hot rolling (HR), various cold rolling (ICR, CCR and SCR) and annealing steps involved in different schedules (a) Schedule I leads to edge crack formation, (b) Schedule II eliminates the edge cracking but leads to alligator crack formation, (c) Schedule III eliminates both types of cracks

The edge crack developed in schedule I and the alligator crack emerged in schedule II are shown in **Fig. 4.2(a)** and **(b)**, respectively. For further investigation, specimens were collected from different location of the cold rolled sheets, as shown by the schematic in **Fig. 4.2(c)** and **4.2(d)**. Two small specimens named ECF and EC1 were cut out from the edge cracked sample. ECF specimen was used to analyze the fracture surface along ND-TD cross-section and EC1 specimen was utilized to carry out the microstructural studies, **Fig. 4.2(c)**. Similarly, another specimen named ACF was collected from the alligator cracked sample to examine the fracture surface parallel to RD-TD cross-section, **Fig. 4.2(d)**. Moreover, for the microstructural and microtextural examination on the alligator crack formation, two small specimens were cut out as shown in **Fig. 4.2(d)**. The specimen collected from the region away from the crack was named AC1, whereas the other specimen around the split end was named AC2.

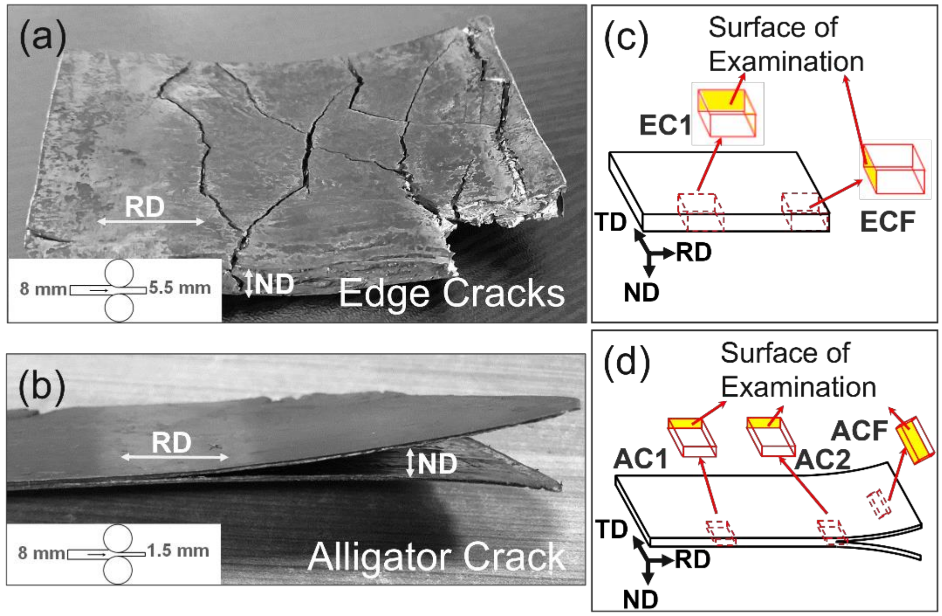

Figure 4.2: (a) Experimental evidence of the formation of edge cracks during cold rolling directly after HR with around 30% thickness reduction, (b) Experimental evidence of the formation of alligator crack during cold rolling after hot band annealing with around 82% thickness reduction, (c) Schematic diagram showing EC1 and ECF specimens cut out from the edge cracked sample shown in (a), (d) Schematic diagram showing various specimens (AC1, AC2 and ACF) cut from the alligator cracked sample shown in (b)

4.3 Microstructure analysis after hot rolling

The optical micrograph of the hot rolled specimen on the ND-RD cross-section from the surface to center is shown in **Fig. 4.3(a)**. The microstructure consists of only ferrite phase, as confirmed by the x-ray diffraction analysis. Most of the grains are found to be large, greater than 1 mm and elongated along the rolling direction. In a limited area, specifically at regions adjacent to grain boundaries, the presence of small recrystallized grains is also noticed as shown in **Fig. 4.3(b, c)**. The area weighted average grain size was found to be 1.22 ± 0.26 mm and the average length of the grains along RD was estimated to be 10.31 ± 2.66 mm.

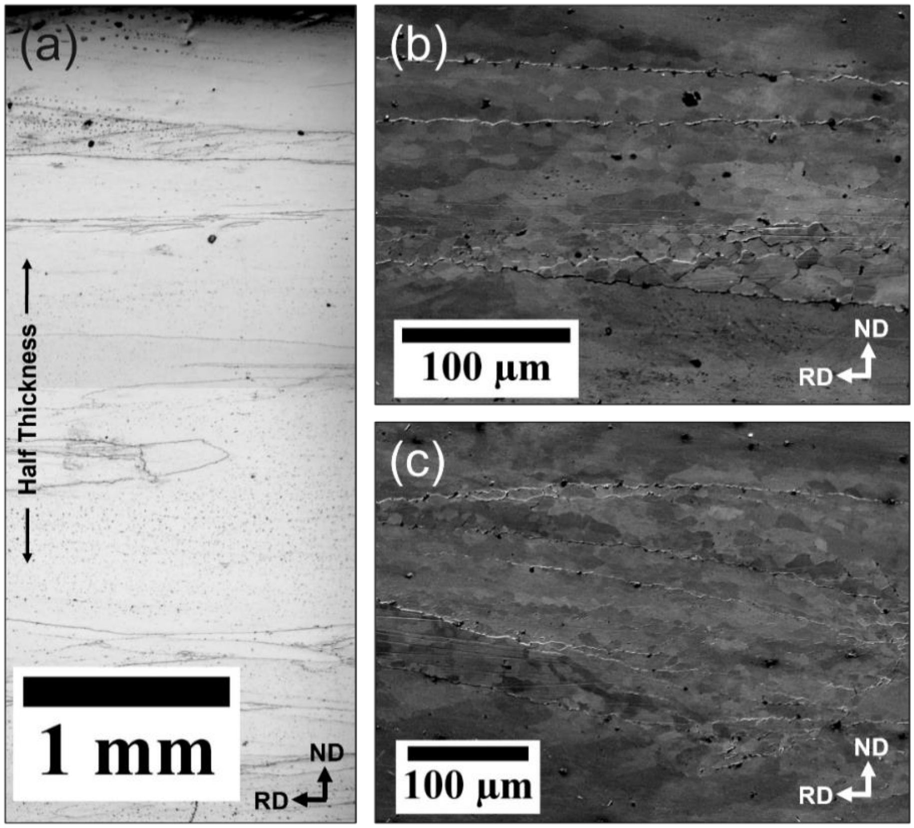

Figure 4.3: (a) Optical microstructure after HR from surface to center (50% thickness) along ND-RD cross-section, (b, c) High magnification FESEM images of the hot rolled sample showing small, recrystallized grains

4.4 Edge cracking

4.4.1 Microstructure analysis of the edge cracked sample

Edge cracking has been noticed in schedule I (as shown in **Fig. 4.1**) during cold rolling after reaching 5.5 mm thickness. The optical micrograph of the EC1 specimen is shown in **Fig. 4.4(a)**. Similar to the hot rolled sample, large, elongated grains were found to be aligned along the rolling direction. Several grains remained undeformed, as shown in **Fig. 4.4(b)**. At the same time, heavy deformation has been observed inside some of the grains as shown in **Fig. 4.4(c)**.

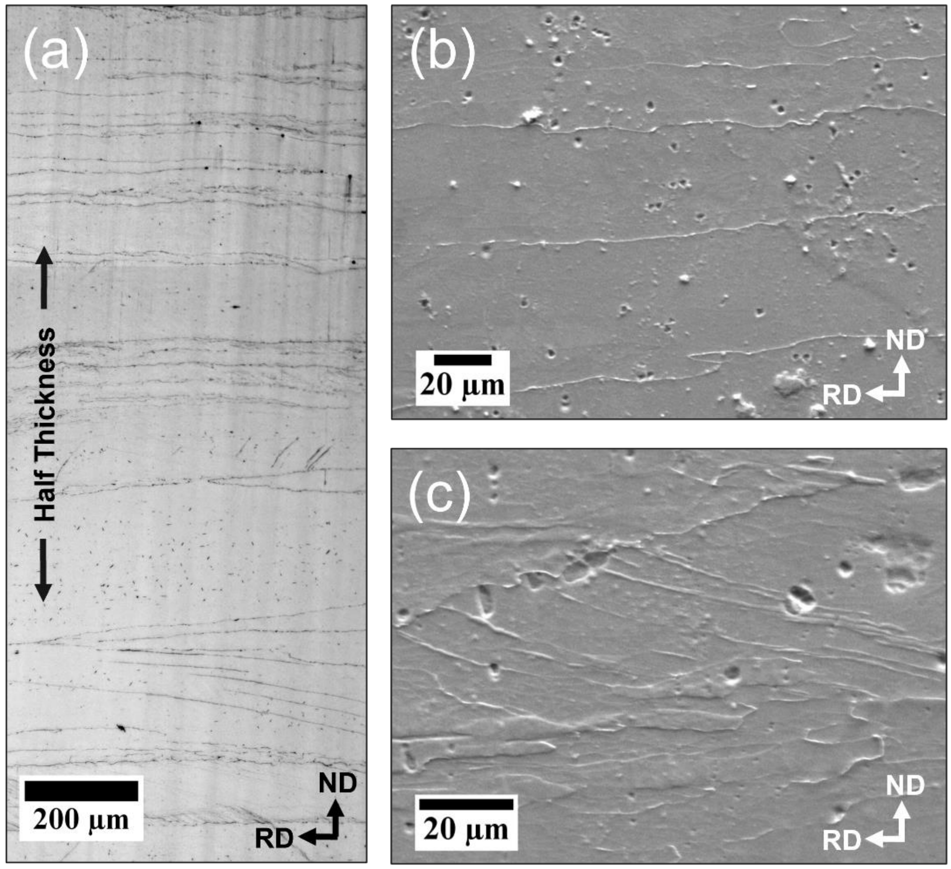

Figure 4.4: (a) Optical micrograph showing through thickness microstructure of the EC1 specimen along ND-RD cross-section (b) FESEM micrograph showing the undeformed grains (c) FESEM micrograph showing the deformed grains

4.4.2 Fracture surface of edge cracks

Fig. 4.5 shows the fracture surface of edge cracks observed on the ECF specimen (as represented in **Fig. 4.2(c)**). The river patterns and cleavage steps appeared on the fracture surface, as shown in **Fig. 4.5**, clearly manifests that it is a transgranular cleavage fracture. Some other studies (Qiao et al. 2003, Hughes et al. 2005, Sorbello et al. 2009, Nakanishi et al. 2016) have also reported similar cleavage crack propagation in Fe-Si steel. Detail study on cleavage crack formation is shown in **Appendix A**.

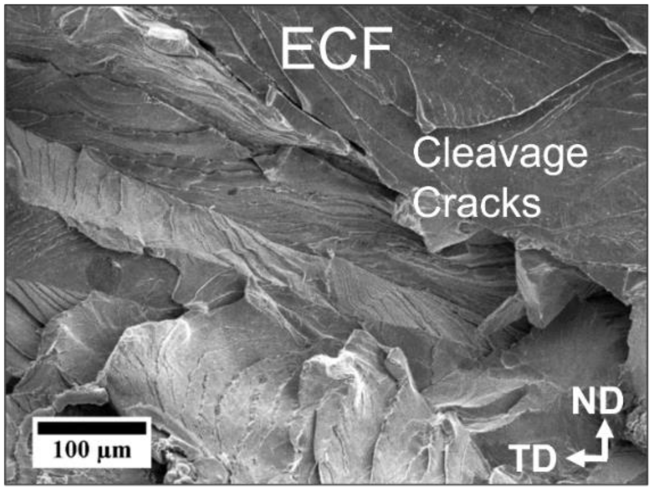

Figure 4.5: Fractographic study showing the fracture surface on ND-TD section of the ECF specimen (edge cracks)

4.5 Alligator cracking

4.5.1 Microstructure analysis of the Alligator cracked sample

Alligator cracking has been found to develop in schedule II (as shown in **Fig. 4.1**) during cold rolling after reaching around 2 mm thickness. The optical micrograph of the AC1 specimen is shown in **Fig. 4.6(a)**. The microstructure reveals the ND-RD cross-section after cold rolling from the surface to center. Non-uniformity in the microstructure manifests inhomogeneous deformation during cold rolling. The light colored regions represent large, elongated grains that remain undeformed. On the other hand, relatively dark colored regions depict the area of heavy deformation. FESEM images of the AC1 specimen, as shown in **Fig. 4.6(b, c)** demonstrate the occurrence of shear bands. Several microcracks are seen initiating inside those shear bands as highlighted with yellow arrows in **Fig. 4.6(b)**. A typical case of the growing microcrack is highlighted by a red arrow in **Fig. 4.6(c)**. The shapes and sizes of the microcracks initiated inside shear bands vary vastly from each other and their average size has been found to be roughly 0.5 µm.

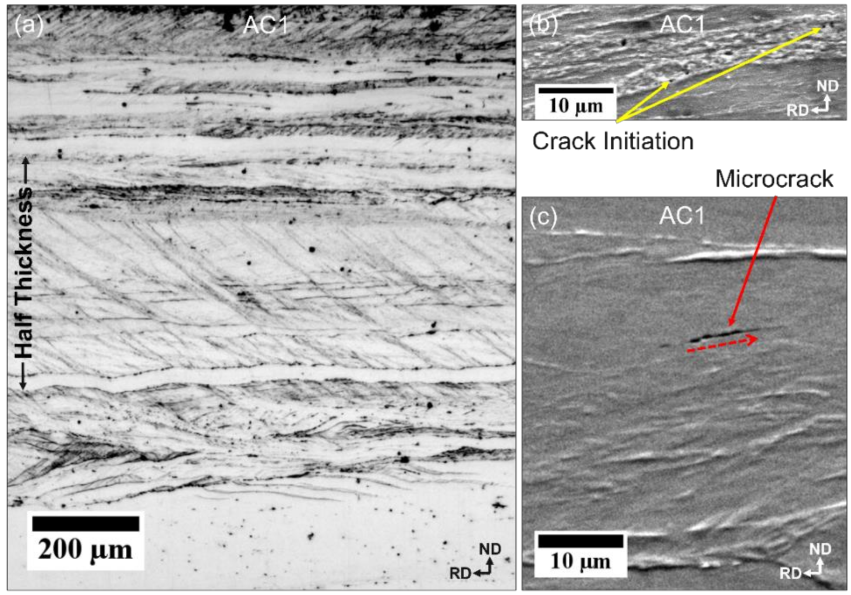

Figure 4.6: (a) Through thickness microstructure of the AC1 specimen along ND-RD cross-section from surface to centre, (b) FESEM micrograph of the shear band region of the AC1 specimen captured under secondary electron mode, (c) FESEM micrograph of the shear band region of the AC1 specimen captured under back-scatter electron mode

4.5.2 Elemental analysis on alligator crack

The presence of impurities and macro-scale segregation during casting may promote alligator crack during the cold rolling process. Therefore, the distribution of different elements such as Si, Mn, and Al across the alligator crack has been examined. **Fig. 4.7** shows the distribution of different elements in the AC2 specimen along the thickness perpendicular to the crack plane, characterized using the EDS analysis. No considerable variation in the distribution of any of the selected elements across the line of crack was observed which rule out the possibility of segregation to be the reason for alligator cracking.

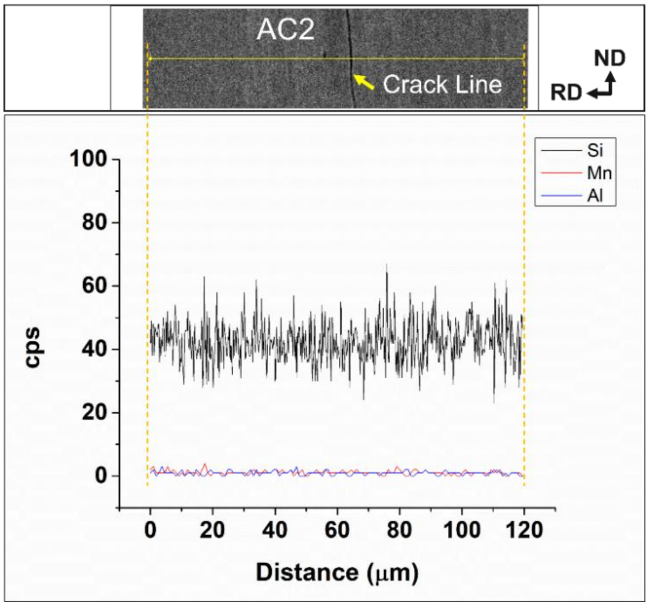

Figure 4.7: Line scan analysis for the distribution of various elements such as Si, Mn and Al across the alligator crack line on the AC2 specimen

4.5.3 Microstructure and microtexture analysis on alligator crack

Fig. 4.8(a) shows the microstructure of the AC2 specimen through thickness around the split region. Mostly, the alligator cracks form around the central region of the cold rolled plate. The crack propagates along the off-centered line before diverging its path towards the center as indicated by red arrows in **Fig. 4.8(a)**. The EBSD analysis was also performed on the AC2 specimen, as shown in the IPF map in **Fig. 4.8(b)**. Severe inhomogeneous deformation in the form of shear bands is distributed throughout the thickness. Shear bands near to the central hot band region develops inside γ-fiber (ND||<111>) oriented grain, as shown by white arrows in **Fig. 4.8(b)**. The hot band, comprising of θ-fiber (ND||<001>) textured grain, remained undeformed after cold rolling. Clearly due to large grain size of the hot band along RD, a flat interface formed between γ-fiber (ND||<111>) and θ-fiber (ND||<001>) textured grains which is named as hot band interface as indicated by yellow arrows in **Fig. 4.8(b)**. This kind of flat interface is expected to promote uninterrupted crack propagation without any deviation. In some regions, the alligator crack was also found to deviate from the mid-thickness path. An example is shown in **Fig. 4.8(c, d)** where the alligator crack was observed to propagate at around 1/4th thickness of the cold rolled plate. But regardless of the position, alligator crack was always noticed to follow either the hot band interface or θ-fiber (ND||<001>) textured grain.

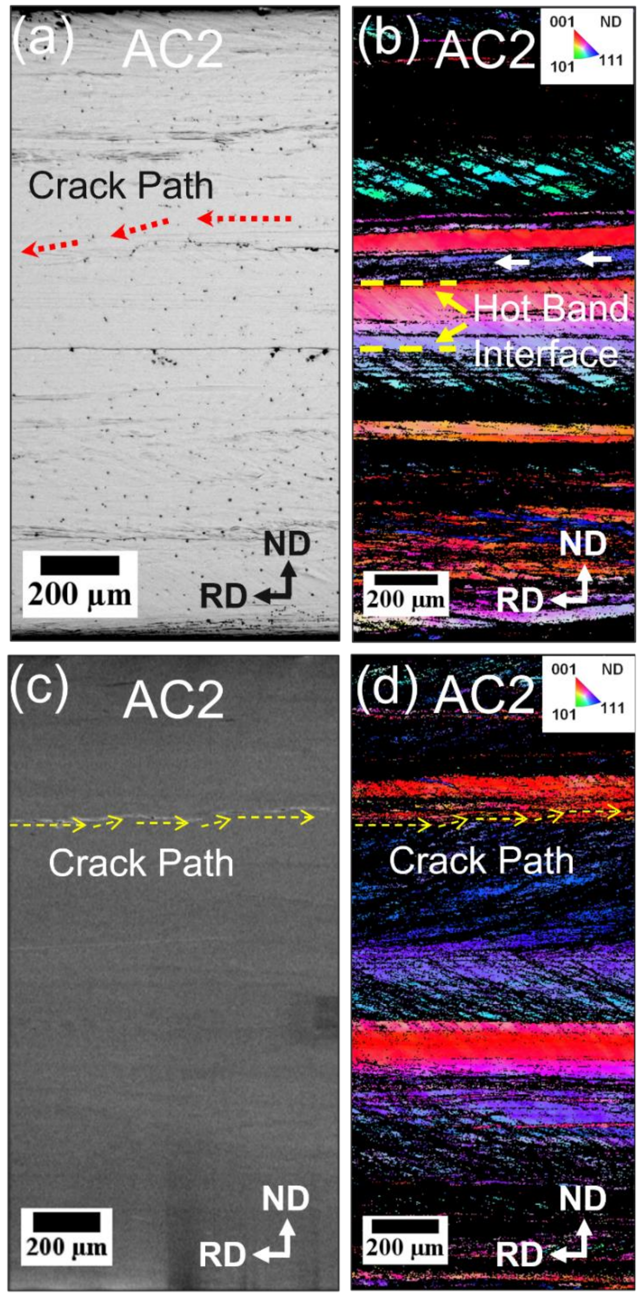

Figure 4.8: (a) Full thickness microstructure of the AC2 specimen along ND-RD cross-section, (b) IPF-ND map of the AC2 specimen after full thickness EBSD analysis conducted on ND-RD cross-section, (c) Through thickness FESEM micrograph (ND-RD cross-section) of AC2 specimen

showing alligator crack, (d) IPF-ND map of the AC2 specimen after full thickness EBSD analysis conducted on the same region shown in (c)

4.5.4 Fracture surface of alligator crack

Fig. 4.9 shows the fracture surface of alligator crack observed on the ACF specimen (as represented in **Fig. 4.2(d)**). The fracture surface appears to be flat having limited features. The mode of fracture could not be determined conclusively.

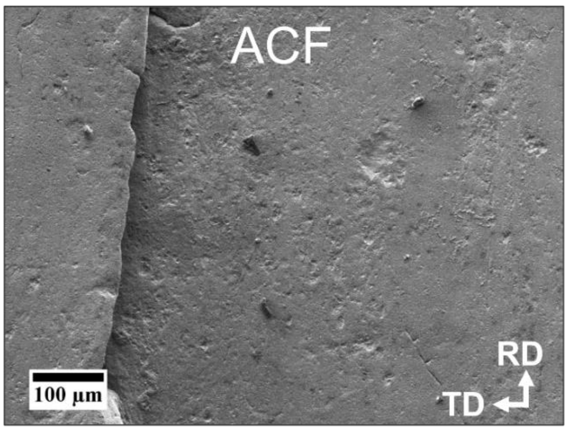

Figure 4.9: Fractographic study showing the fracture surface of the ACF specimen (alligator crack)

4.6 Rolling Simulation based on Finite Element Method

The rolling experiment was simulated with the help of FEM as shown in **Section 3.4.1**. In order to incorporate the elastic-plastic material property, the experimentally measured flow stress of CRGO steel under plane strain compression by Calvillo et al. (Calvillo et al. 2006) has been employed. The state of stress at different locations within the rolled plate plays a crucial role in understanding the formation of both alligator crack and edge crack. The x-direction, y-direction and z-direction in the simulation were taken as the representation of RD, ND and TD during the rolling experiment, respectively. **Fig. 4.10** shows the variation of roll force (along y(ND)-direction) with time during rolling. Increase in compressive roll force up to around 4 s, as shown in **Fig. 4.10**, denotes that the steel plate was not completely in-between the rollers. Furthermore, it attains a steady state between the time around 4 to 11 s indicating that the steel plate was completely in-between the rollers as highlighted in **Fig. 4.10**. The roll force was maximum at 6.6 s. Finally, the gradual decrease in compressive roll force after around 11 s denotes the departure of the steel plate at the other end. **Fig. 4.11(a)** represents the distribution of normal stress acting along the y(ND)-direction (S22) at 3.3 s as indicated in **Fig. 4.10**. **Fig. 4.11(b, c)** shows the distribution of normal stress acting along the y(ND)-direction (S22) at 6.6 and 12.3 s (as indicated in **Fig. 4.10**), respectively. **Fig. 4.11(d)** represents the evaluation of S22 with time for the selected elements located at the center and surface as marked with red dot in **Fig. 4.11(a, b, c)**. The whole representation of the stress state analysis illustrates that the normal stress along the y(ND)-direction (S22) at the entrance (before 3.3 s) and exit (after 12.3 s) stages were predicted to be tensile in nature as indicated by white arrows in **Fig. 4.11(a, c)**. The magnitude of the tensile stress was found to be higher at the centre compared to the surface region as shown in the insets in **Fig. 4.11(d)**. In the steady state zone during rolling simulation, the normal stress acting along the y(ND)-direction was found to be compressive in nature as expected irrespective of the location.

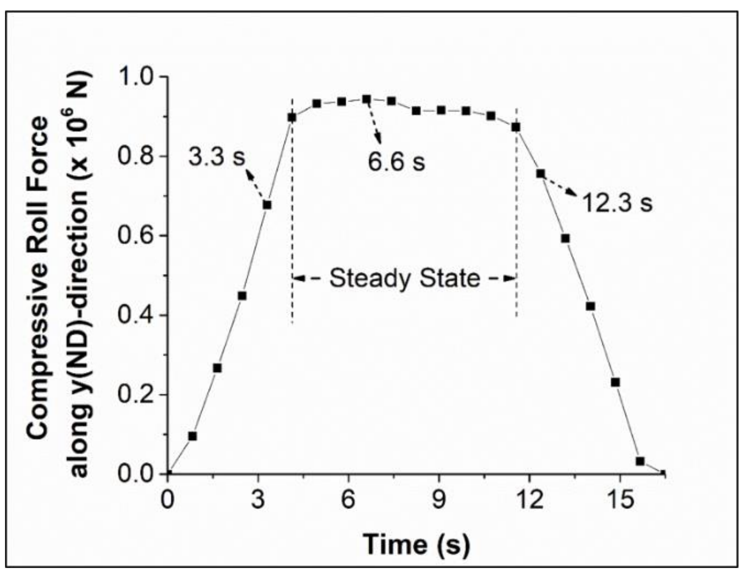

Figure 4.10: Roll Force vs Time graph during the rolling simulation for 20% thickness reduction

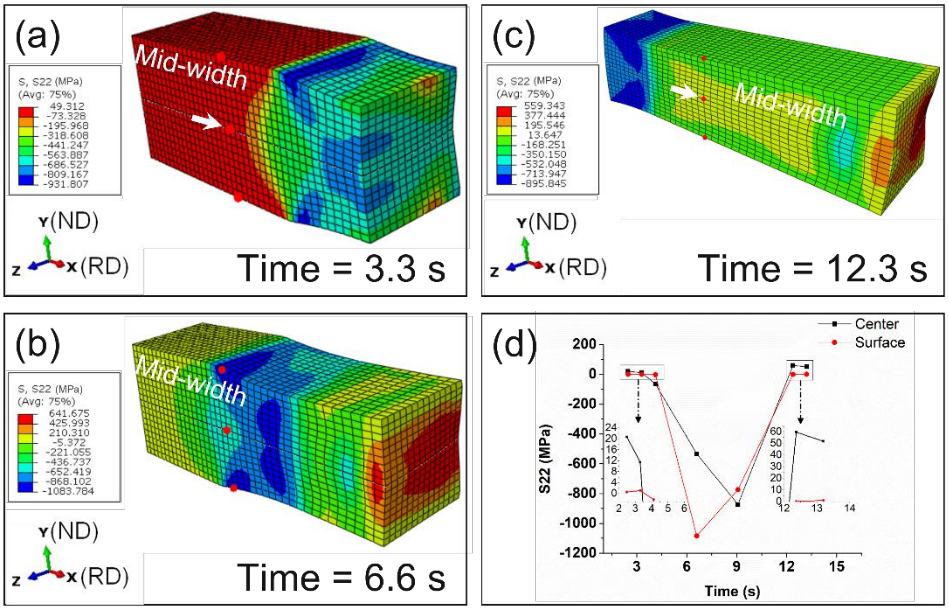

Figure 4.11: Normal stress distribution along y(ND)-direction (S22) along mid-width at (a) entry stage (3.3 seconds), (b) maximum Roll force in the steady state zone (6.6 seconds) and (c) exit stage (12.3 seconds), (d) S22 vs Time graph for the element shown by the red dot in (a,b,c) at centre and the surface during rolling simulation

Similarly, **Fig. 4.12(a, b)** shows the distribution of normal stress along the x(RD)-direction at the end-width (S11, end-width) at 6.6 and 12.3 s, respectively. The normal stress (S11, end-width) was found to be highly tensile at the end of the width, as indicated by white arrow in **Fig. 4.12(a)**. Moreover, **Fig. 4.12(c, d)** also exhibit the distribution of normal stress along the x(RD)-direction at the mid-width (S11, mid-width) at 6.6 and 12.3 s, respectively, during rolling simulation. The normal stress (S11, mid-width) at the maximum roll force (6.6 s) was found to be completely compressive at the middle of the width as indicated by white arrow in **Fig. 4.12(c)**. Moreover, during the exit stage (12.3 s) high tensile stress developed at the region close to the surface (indicated by white arrow in **Fig. 4.12(d)**).

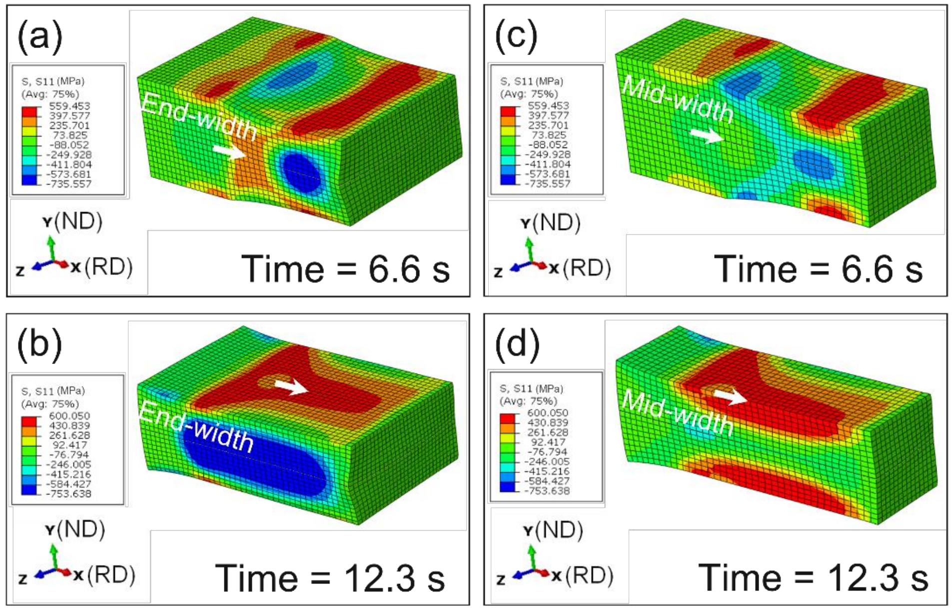

Figure 4.12: Normal stress distribution along x(RD)-direction (S11) along end-width at (a) maximum Roll force in the steady state zone (6.6 seconds) and (b) exit stage (12.3 seconds), and Normal stress distribution along x(RD)-direction (S11) along mid-width at (c) maximum Roll force in the steady state zone (6.6 seconds) and (d) exit stage (12.3 seconds)

4.7 Discussion

4.7.1 Edge crack

The edge cracks shown in **Fig. 4.5** develops as brittle transgranular cleavage fracture after around 30% thickness reduction during cold rolling. The subtle changes in normal stress acting along RD during the cold rolling process plays a crucial role in the formation of these edge cracks (Dodd et al. 1980, Barlow et al. 1984, Xie et al. 2011, Yan et al. 2013, Sun et al. 2015, Zan et al. 2017). The distribution of normal stress along the x(RD)-direction (S11, mid-width and end-width) during rolling simulation is illustrated in **Fig. 4.12(a-d)**. During the steady-state zone when the roll force was maximum (6.6 s), most part of the thickness at the end-width undergo high tensile stress along the x(RD)-direction, as indicated by white arrow in **Fig. 4.12(a)**. At the mid-width region the normal stress along RD has been predicted to be compressive as indicated by white arrow in **Fig. 4.12(b)**. Later, during the exit stage high tensile stress develops at the mid-width section (**Fig. 4.12(d)**) which further promotes the crack propagation in this region. Therefore, the edge cracking is likely to initiate at the end-width during the steady state zone (6.6 s) and the crack propagates further in TD during the exit stage (12.3 s). Also, the magnitude of the tensile normal stress in RD can be higher than 250 MPa at steady state zone (6.6 s), as seen in **Fig. 4.12(a)** for the rolling load corresponding to 20% thickness reduction. With the increase in flow stress of CRGO steel and the amount of thickness reduction in a single pass, the normal stress in RD may further increase.

$$\sigma_f = \sqrt{\frac{2E\gamma_p}{(1-\nu^2)d_p}} \tag{4.1}$$

On the other hand, the hot rolled microstructure as shown in **Fig. 4.3(a)** is coarse (an average grain size of 1.22 mm) and its cleavage fracture strength is anticipated to be low. Generalized Griffith's equation (Chen et al. 1990, Ghosh et al. 2013) was employed to calculate the cleavage fracture stress (σ_f) as shown in equation (4.1) where the values of Young's modulus (E) and poisson's ratio (ν) were taken as 210 GPa and 0.3, respectively. The cleavage fracture stress of the hot rolled sample was found to be less than 150 MPa after assuming the effective surface energy (γ_p) as 50 J/m^2 (Gerberich et al. 1985, Wu et al. 2004, Kawata et al. 2018). Hence, the high tensile normal stress in RD at the end-width of the cold rolled plate may have promoted the edge crack formation along TD during the cold rolling process. Hot band annealing and intermediate annealing in schedule-II and schedule -III, **Fig. 4.1(b, c)**, were found to be effective in eliminating edge cracks. The IPF maps of hot band annealed and intermediate annealed samples are shown in **Fig. 4.13(a, b)**, respectively. The grain size distribution of both the samples is also shown in **Fig. 4.13(c, d)**. On hot band annealing and intermediate annealing, the microstructure gets refined as shown in **Fig. 4.13(a, b)** with the average grain (recrystallized) size of 256 μm and 110 μm, respectively. As a result, the cleavage fracture strength of annealed samples is expected to be more than 300 MPa and thus the possibility of edge cracking in the annealed samples gets diminished. However, some of the large grains elongated along RD remained unrecrystallized after hot band annealing as shown in **Fig. 4.13(a)**. Despite the presence of these large grains in the microstructure, the edge cracking did not occur. Therefore, here the weakest link theory could not explain the non-occurrence of edge cracking phenomenon after hot band annealing.

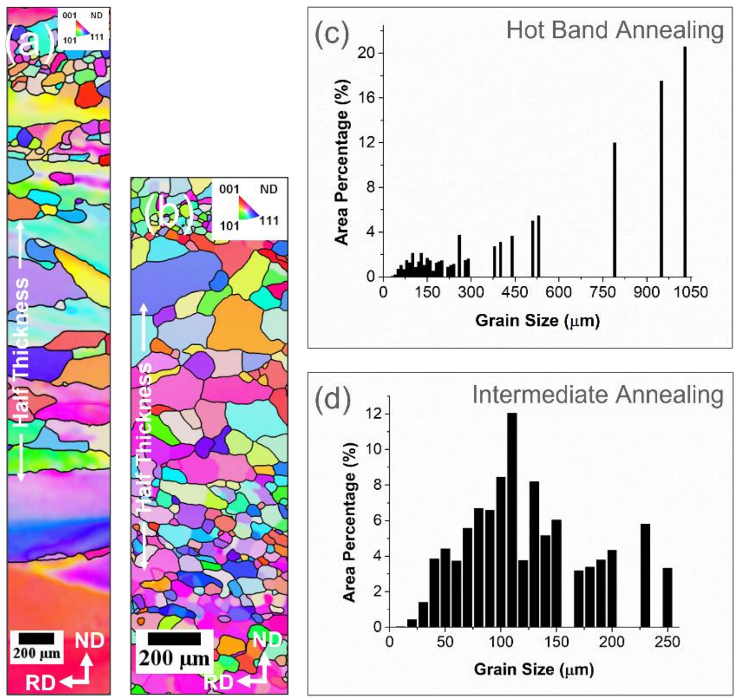

Figure 4.13: (a) IPF-ND map from surface to center (50% thickness) after hot band annealing done at 800° C for 30 minutes, (b) IPF-ND map of the cold rolled sample followed by intermediate annealing at 800° C for 30 minutes from surface to center (50% thickness), grain size distribution after (c) hot band annealing and (d) intermediate annealing

Fig. 4.14(a-c) illustrate a schematic representation of the formation of edge crack during the cold rolling process. The normal stress acting along the x(RD)-direction (S11) in the steady-state zone (6.6 s) and the exit stage (12.3 s) during rolling simulation is shown in **Fig. 4.14(a, c)**, respectively. The high tensile stress at the edges during the steady state condition initiates the edge crack, which propagates inwards (along TD) during the final exit stage, **Fig. 4.14(b, c)**.

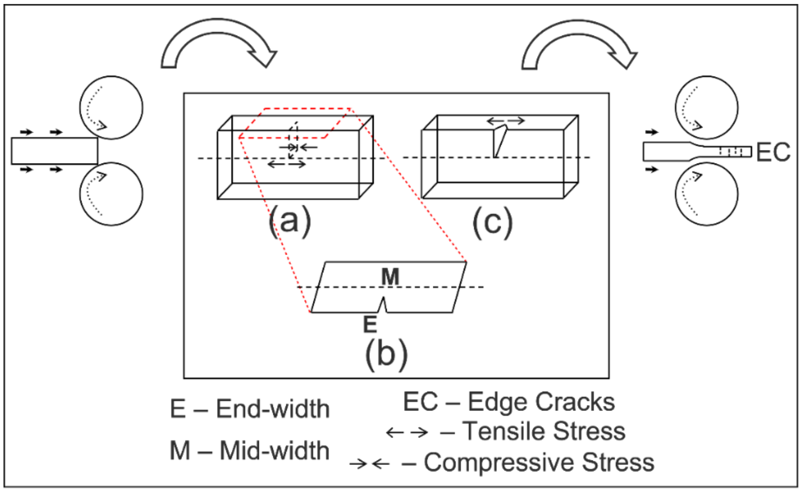

Figure 4.14: Schematic showing the steps involved in the edge crack formation during the cold rolling process of high Si CRGO steel

4.7.2 Alligator crack

Alligator crack was found to initiate during the cold rolling process inside the shear band regions. The strain accumulation inside shear bands was significantly higher than the region outside the shear bands, which can promote the formation of voids due to strain incompatibility. Furthermore, the cracks were found to propagate along the flat hot band interface as manifested in **Fig. 4.8(a-d)**. The elongated grain boundaries provided an easy path for the alligator crack propagation. The flat hot band interface mainly arises because large θ-fiber (ND||<001>) oriented grain remained un-recrystallized during HR followed by the annealing step and was subsequently stayed undeformed during the cold rolling operation. The crystallographic orientations of the neighboring grains surrounding the hot band interface might have played an important role in the formation of alligator crack. The EBSD analysis was conducted on the AC2 specimen around the region of the alligator crack as shown by the IPF-ND map in **Fig. 4.15(a)**. γ-fiber (ND||<111>) and θ-fiber (ND||<001>) texture components were mainly observed around the cracked region of the cold rolled plate and were named as regions 1 and 2, respectively. Region 1 corresponds to the shear band region whereas region 2 corresponds to the hot band region. The extent of grain rotation for {001}<110> and {111}<110> texture components, which were primarily present around the alligator crack are expected to be insignificant, since both of them are stable orientations under plane strain compression (Ray et al. 1994, Jain, Modak, et al. 2022). Therefore, orientations of the crystal in region 1 and region 2 prior to deformation are anticipated to remain unaltered during cold rolling. Different crystallographic orientations of the neighboring grains promote dissimilarity in their deformation behavior. The Taylor factor represents the extent of slip activity for a given crystal orientation and deformation mode in iso-strain condition. Under plane strain compression, the Taylor factor for different orientations (regions 1 and 2) as marked in **Fig. 4.15(a)** has been calculated using Mtex toolbox in MATLAB by considering {110} <111> and {112} <111> slip systems in BCC and represented in **Fig. 4.15(b)**. Region 1 ({111}<110>) posses roughly about 1.7 times higher Taylor factor compared to region 2 ({001}<110>). Therefore, it is expected that the shear strain or the dislocation density in region 1 would be around 1.7 times higher than that in region 2 (Nguyen-Minh et al. 2012, Sarkar et al. 2019, Mehdi et al. 2020, Jain, Modak, et al. 2022). In other words the slip systems in region 1 gets hardened and further accommodation of slip in region 1 will become difficult. For further confirmation, the hardness of the shear band region and the hot band region were separately measured with the help of Vickers Microhardness testing machine under 0.3 kg load with diamond indenter. As expected, the hardness of the shear band region was found to be higher, around 372 ± 7 HV, compared to the hardness of the hot band region which was around 314 ± 2 HV.

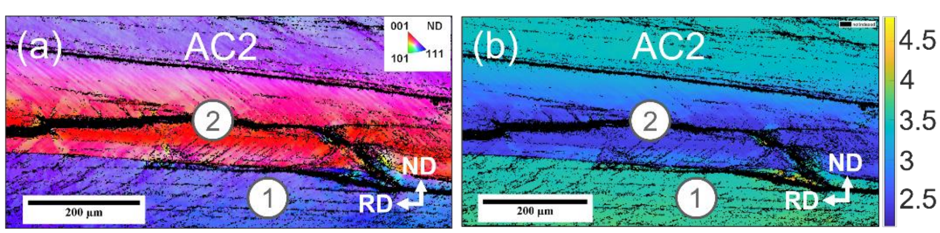

Figure 4.15: (a) IPF-ND map after conducting EBSD analysis on ND-RD cross-section at the area showing the alligator crack region of the AC2

specimen, (b) Taylor factor map under plane strain compression showing that different oriented grains (regions 1 and 2) have different Taylor factors

Although the shear bands and the flat hot band interface promote the alligator crack formation, the crack would not have been stable without the existence of normal tensile stress on the crack plane. The formation of crack around the mid-thickness region parallel to the rolling plane was itself unexpected since the rolled plate was anticipated to be under compression in ND. Turczyn et al. (Turczyn et al. 1992) had performed the FEM-based stress analysis and reported that the stress state at the center of the rolled plate is crucial in splitting of the plate during exit of the rolling process. The rolling simulation results shown in **Fig. 4.11(a-d)** clearly depicts that despite overall stress acting on the plate was compressive, there were tensile stresses acting along the y(ND)-direction (S22) at the entry and exit stages of cold rolling around mid-thickness of the plate. The maximum value of this tensile stress was around 20 MPa at the entry stage and 50 MPa at the exit stage for 20% thickness reduction. Therefore, this tensile nature of normal stress along the y(ND)-direction (S22) may promote the propagation of the alligator crack through the interface between regions 1 and 2 (**Fig. 4.8(a-d)** and **Fig. 4.15(a)**).

Mostly, the crack was found to propagate inside the θ-fiber (ND||<001>) textured grain as shown in **Fig. 4.8(b, d)** and **4.15(a)**. Interestingly, the shear bands have not been observed inside θ-fiber (ND||<001>) textured grain (**Fig. 4.8(b, d)**). Therefore, it is anticipated that shear bands do not to play any significant role on the propagation of alligator crack. The alligator crack is likely to propagate in cleavage fashion inside the θ-fiber (ND||<001>) textured grain. The EBSD analysis was performed covering a larger area of the AC1 specimen on both ND-RD and ND-TD cross-sections as shown by IPF maps in **Fig. 4.16(a)** to understand the overall shape and size of the hot band and constituent grains. The alligator crack was mostly propagating through the large θ-fiber (ND||<001>) textured regions as shown in **Fig. 4.8(b, d)** and **Fig. 4.15(a)**.

The size of the θ-fiber (ND||<001>) textured grain (mostly at the mid-thickness) was extremely large, more than 10 mm along RD which is evident in **Fig. 4.16(a)**. The cleavage fracture stress (σ_f) has been calculated considering the same values for Young's modulus (E), Poisson's ratio (ν), and effective surface energy (γ_p) as mentioned in **Section 4.7.1**. Since, the path followed by the alligator crack was parallel to the rolling plane, the crack was expected to be parallel to the length of the θ-fibered grain. Therefore, the length of θ-fiber textured grain along RD was considered as grain size (d_p) in Griffith's equation. The expected cleavage fracture stress of a grain having 10 mm grain size was found to be less than 50 MPa. Although the cleavage fracture stress was estimated to be extremely low which is unusual, such low value of cleavage fracture strength can occur due to the presence of extensively large grains.

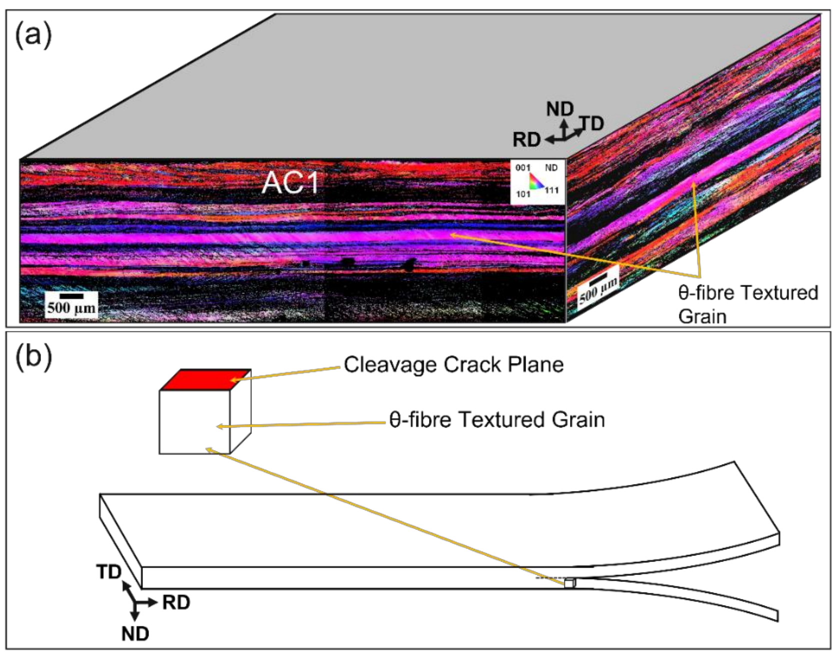

Figure 4.16: (a) AC1 specimen showing IPF-ND maps after conducting large EBSD analysis on ND-RD and ND-TD cross-sections through the thickness, (b) Schematic representing θ-fiber textured grain and cleavage crack plane at the central region around the alligator crack formation during the cold rolling process

In addition, the {001} cleavage plane in θ-fiber (ND||<001>) textured ferrite grain was also oriented parallel to the rolling plane and thus is in line with the crack plane of alligator crack as shown by the schematic in **Fig. 4.16(b)**. Similarly, in a recent work (Ghosh et al. 2016), it has been reported that the cluster of cube oriented grains having a rolling plane parallel to the {001} cleavage plane (i.e. ND||<001>) provides easy cleavage crack propagation path. The predicted normal stress (tensile) that was above 50 MPa in ND at mid-thickness during the exit stage (**Fig. 4.11(d)**), was sufficient to cause cleavage fracture in the cold rolled plate as the normal stress was also acting perpendicular to the {001} cleavage plane.

On the other hand, an intermediate annealing treatment shown in schedule-III, **Fig 4.1(c)**, has been found to be effective in preventing the alligator crack formation. The microstructure gets refined after intermediate annealing as shown in **Fig. 4.13(b)**. Importantly, the hot band structure completely gets eliminated by the intermediate annealing treatment. The deformed cold rolled structure is likely to provide more nucleation sites for recrystallization during intermediate annealing and thereby helps in removing the hot band structure and large θ-fiber (ND||<001>) textured grains. Elimination of these key microstructural features diminished the propensity of alligator crack in the intermediate annealed structure. In addition, the fine grain structure obtained after intermediate annealing is also expected to deform uniformly through thickness during the subsequent cold rolling step and reduces the possibility of cracking.

The steps associated with the initiation and propagation of alligator crack are schematically demonstrated in **Fig. 4.17(a-e)**. The mid-thickness region of the cold rolled plate showing shear bands (region 1) and the hot band (region 2) is indicated in **Fig. 4.17(a)**. The microcracks first initiated inside the region 1 as portrayed in **Fig. 4.17(b)**, which further extended into a crack along the shear bands by the coalescence of these microcracks as shown in **Fig. 4.17(c)**. The crack then reaches the hot band interface and further propagates between region 1 and 2 along the hot band interface, as shown in **Fig. 4.17(d)**. Later, the alligator crack prefers to propagate inside the large θ-fiber (ND||<001>) textured grain owing low (<50 MPa) cleavage fracture strength, **Fig. 4.17(d)**. It is worth noting that normal tensile stress in ND promotes the alligator crack as demonstrated in **Fig. 4.17(d, e)**.

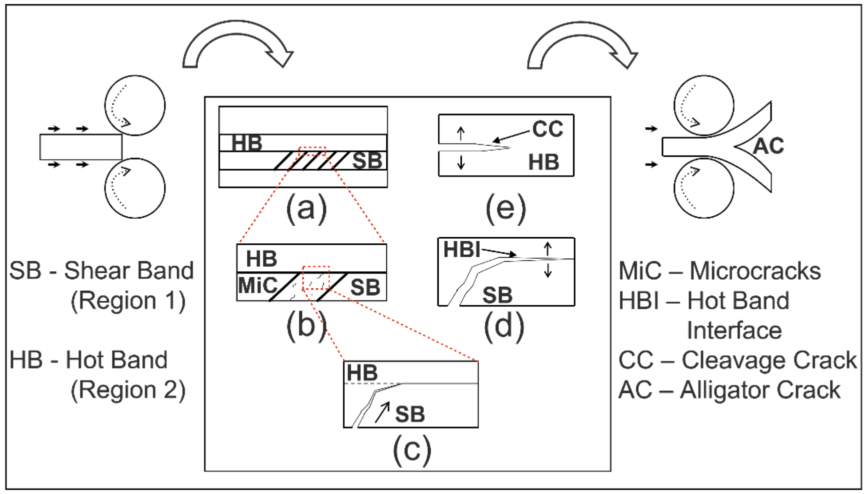

Figure 4.17: Schematic showing the steps involved in the alligator crack formation during the cold rolling process of high Si CRGO steel

In general, cleavage crack initiation is often linked to grain boundary segregation. However, in the present investigation, the carbon concentration in Fe-Si alloy was highly low, **Table 3.1**, and therefore, segregation in the form of grain boundary carbides was not observed. Moreover, other elements such as phosphorus, sulphur, boron, etc. (which are also extremely low in the investigated alloy) may also cause grain boundary segregation, but they usually cause intergranular fracture. In the present study, the edge cracks and alligator crack were mostly transgranular, except for some part of the alligator crack which was found to propagate along the grain boundary. Therefore, the grain boundary segregation was not expected to play a significant role. Further, to completely rule out the possibility of grain boundary segregation on edge cracking and alligator cracking, the segregation at the grain boundaries needs to be examined employing EPMA and/or special etching techniques.

4.8 Conclusions

The following conclusions can be drawn from the present study:

(a) FEM-based stress analysis reveals that cleavage edge crack initiates due to the development of high tensile stress at the edges during steady state condition. The edge crack propagates inwards along TD during the final exit stage.

(b) Hot band annealing was found to be effective in refining grain size and thus inhibit the formation of edge crack.

(c) High strain incompatibility results in initiation of alligator crack inside shear band regions, which develops during cold rolling of Fe-3.78 wt. % Si CRGO steel. Furthermore, the alligator crack was found to follow the hot band interface between {111}<110> and {001}<110> oriented grains having large difference in Taylor factor.

(d) FEM-based stress analysis demonstrates that normal tensile stress in ND develops at the mid-thickness during the exit stage of the cold rolling process.

(e) The alligator crack further propagates through the large elongated θ-fiber (ND||<001>) textured grains owing to significantly low (<50 MPa) cleavage fracture stress and favorable orientation of the {001} cleavage plane parallel to the fracture plane.

(f) Intermediate annealing between the cold rolling passes prevents the formation of alligator crack due to the elimination of the hot band structure.

CHAPTER 5

Study on step by step development of Goss texture in the processing of Fe-3.78wt.%Si cold rolled grain oriented steel

5.1 Introduction

The processing route of CRGO steel typically consists hot and cold rolling which is then followed by two stage annealing process known as primary and secondary recrystallization. In the final step of the processing, most part of the microstructure become composed of coarse Goss orientated ({110}<001>) grains. A characteristic feature of CRGO steel is that the final Goss oriented grains generally develops to be more than 10 mm in size (Wang et al. 2016, Fang et al. 2017). Chang et al. (Chang 2005) reported that normalizing before cold rolling helps in producing grains larger in size during primary and secondary recrystallization compared to those developed without normalizing. Annealing after hot rolling was also remarkably reported to enhance the magnetic properties of the CRGO steel (C. Hou 1996). Further, cold rolling is done using either two stage cold rolling method which involves intermediate annealing in between them or single stage cold rolling method with heavy deformation. However, Song et al. (Song et al. 2016) showed that two stage cold rolling method was ineffective in producing high quality Goss texture with large grain size.

Despite, a lot of progress has been done during the last two decades in producing CRGO steel to ensure low core losses (Xia et al. 2008). The primary origin of the final Goss texture is still a matter of debate to the scientific community. Some of the authors reported that the formation of Goss orientation first occurs during hot rolling due to high shear deformation beneath the surface layers (Matsuo et al. 1986, Mishra et al. 1986, Böttcher et al. 1993). The studies demonstrated that the Goss oriented grains develop by 'texture inheritance' during primary recrystallization, which were related to those formed earlier in the hot rolled structure. On the contrary, Goss orientation was shown to rotate towards the other orientations such as, {111}<112>, during cold rolling (Dorner et al. 2007, Mehdi et al. 2019). Many authors showed that the evolution of Goss orientation was related to the development of shear bands at the cold rolling stage (T Haratani et al. 1984, Ushioda et al. 1989, I Samajdar et al. 1998, Schneider et al. 2016). The studies reported that the high strain energy regions inside shear bands, acted as the nucleation sites for Goss oriented grains during primary recrystallization annealing. In general, grain size, crystallographic orientation and strain rate affects the formation of shear bands. Different crystallographic orientations which have high Taylor factor were reported to develop shear bands (SHIN et al. 2008, Nguyen-Minh et al. 2012, Mehdi et al. 2020, Jain, Modak, et al. 2022). The high Taylor factor of {111}<112> component of γ-fiber (ND||<111>) texture was reported to promote the shear band formation during cold rolling, which were then responsible for the development of Goss orientation on subsequent primary recrystallization (T Haratani et al. 1984, Ushioda et al. 1989, Jain, Modak, et al. 2022). However, Shin et al. (SHIN et al. 2008) reported that the shear band formation during cold rolling were also possible inside {112}<110> oriented grains because of high Taylor factor, which can as well act as the nucleation sites for Goss oriented grains to recrystallize during primary recrystallization.

Further, Goss oriented grains develops by the abnormal grain growth process during secondary recrystallization. The selective growth of Goss oriented primary grains depends upon different factors. Hillert et al. (Hillert 1965) showed that the abnormal grain growth occurs due to the size advantage of Goss oriented grains in the primary recrystallized structure. Nevertheless, it was also demonstrated later that the abnormal grain growth cannot possibly occur only to a grain having larger grain size in the matrix (Chen et al. 2003, Guo et al. 2010). It was established that the primary recrystallization was required to develop homogeneous spread of recrystallized grains among which one single grain having Goss orientation was then favoured with the abnormal growth criteria to outgrow millions of grains present in the surroundings (Lin et al. 1996, Shimizu et al. 1989). Different analogies have been reported to understand the growth environment that benefits only Goss oriented grains to grow during secondary recrystallization annealing (Hayakawa 2017). One of the important criteria was to know the character distribution of the grain boundaries among the primary recrystallized grains. Various workers portrayed that the Goss oriented primary grains must be exceptionally surrounded by the high energy grain boundaries having misorientation angle between 20°-45° (Hayakawa et al. 2002, Y Hayakawa et al. 1997, Y. Hayakawa et al. 1997, Hayakawa et al. 1998, Rajmohan 1997, Rajmohan, J. A. Szpunar, et al. 1999, Rajmohan, J. . Szpunar, et al. 1999, Rajmohan et al. 2001). These studies reported that the grain boundaries having mid-range misorientation angle between 20°-45° are noted to be high energy (HE) grain boundaries which supports Goss oriented grains to grow abnormally during secondary recrystallization. But, Inamura et al. (Imamura et al. 2013) demonstrated that grain having orientation different than Goss orientation, which is surrounded by the HE grain boundaries was also susceptible for abnormal grain growth. On the other hand, it was also shown that the low Coincidence Site Lattice (CSL) boundaries which were generally recognized to have low grain boundary energy, were capable to generate high grain boundary mobility giving growth advantage to Goss oriented grains over other primary grains (Lin et al. 1996). However, different authors suggested the role of different kind of CSL boundaries, such as Σ5 by gangli et al. (Gangli et al. 1994), Σ7 by harase et al. (Harase 1992) and Σ9 by a number of researchers (Rouag et al. 1990, Yoshitomi et al. 1993, Kumano et al. 2002, Kumano et al. 2003a, Kumano et al. 2003b), to be present in the vicinity of Goss oriented primary grains promoting abnormal grain growth. Importantly, it has also been reported severally that if any unrecrystallized grains remained among the primary grain structure, then it affects the abnormal grain growth behaviour later during secondary recrystallization (Littmann 1975, Wang, Xu, Zhang, Fang, Lu, Misra, et al. 2015, Song et al. 2016, Fang et al. 2017). Song et al. (Song et al. 2021) showed that the increase in λ-fiber (ND||<100>) textured grains having large grain size among the primary recrystallized structure decreases the chances of abnormal growth of Goss oriented grains on subsequent secondary recrystallization annealing.

Despite of significant effort on the understanding of Goss texture development in CRGO steel, less studies has been directed on complete development of CRGO steel covering all the processing steps. Similarly, the role of all processing steps involved on the final evolution of Goss orientation has not been studied thoroughly. Present investigation aims to demonstrate a complete picture on the development of grain oriented steel with the associated challenges involved. Our study presents a systematic thorough investigation on overall microstructural and textural development during the process of CRGO steel starting from alloy designing to secondary recrystallization. In addition, the critical factors affecting the development of Goss orientation during different steps has been addressed.

5.2 Equilibrium diagrams and processing of HSI CRGO steel

Thermodynamic analyses were performed with the actual composition of HSI steel to predict equilibrium phases in the temperature range of 600° C to 1600° C, **Fig. 5.1(a)**. The austenite phase was not predicted to develop between 600° C to 1600° C. Negligible amount (<0.1 wt. %) of cementite was expected to form below 701° C. Moreover, the predicted equilibrium fraction of MnS and AlN precipitates are shown in **Fig. 5.1(b)**. The precipitation of MnS particles started at 1198° C and becomes saturated at 928° C, while AlN started precipitating at 937° C and finished at around 718° C.

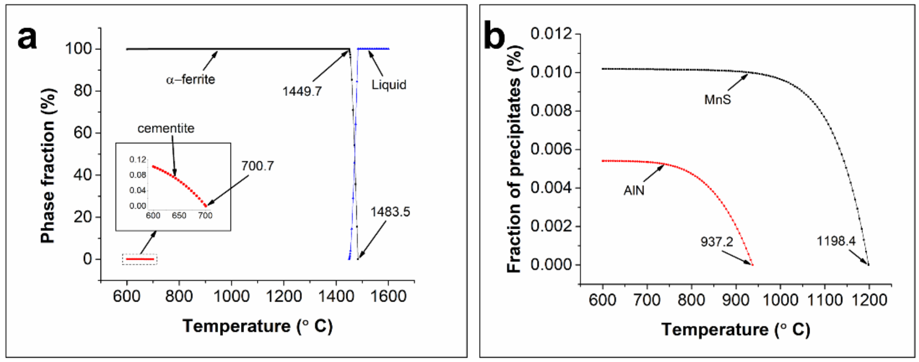

Figure 5.1: Thermodynamic calculations showing (a) equilibrium phases and (b) fraction of precipitates after considering actual composition of high silicon CRGO steel

The complete experimental details of the processing of HSI are given in **Chapter 3**. The microstructure after reheating consists of extremely large grains up to roughly 5 mm as shown in the macro image in **Fig. 3.2**. A temperature-time representation of the processing of HSI steel starting from HR to final annealing processes is shown in **Fig. 5.2(a)**, and the complete step by step representation of the process including strains achieved after various deformation stages is shown in **Fig. 5.2(b)**.

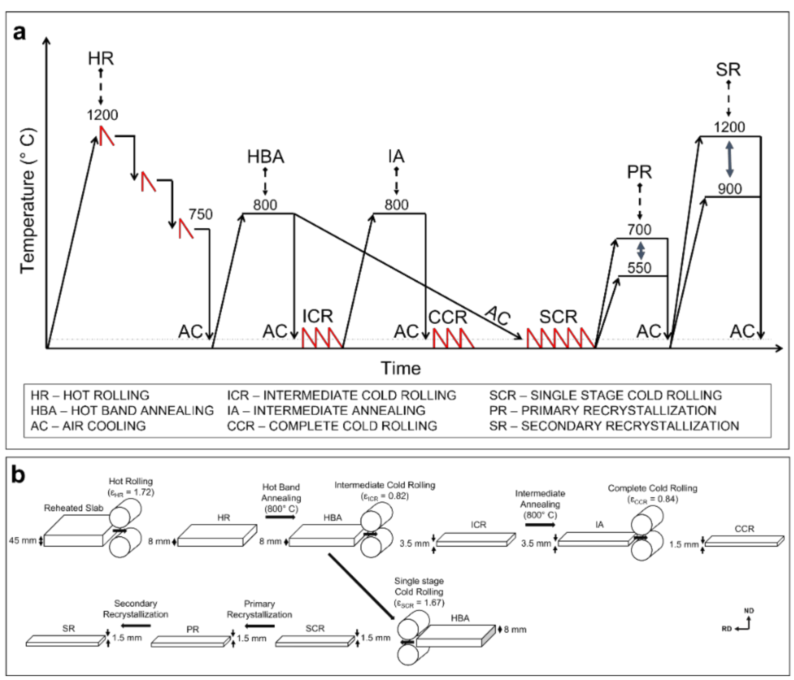

Figure 5.2: (a) Temperature vs Time representation of the processing of HSI steel starting from hot rolling (HR) to final annealing stages, and (b)

Complete step by step schematic representation of the processing of HSI steel

5.3 Microstructure and Microtexture Development after hot rolling

Fig. 5.3(a) shows the microstructure of HSI steel after HR from surface to center. Deformation of highly coarse grain structure, **Fig. 3.2**, generated large hot bands having grain size >5 mm along RD. The IPF map of HR sample is shown in **Fig. 5.3(b)**. The texture gradient was prominent from surface to the central region of the hot rolled plate. Rotated cube ({001}<110>) component of α-fiber (RD||<110>) texture was observed at the mid-thickness region, **Fig. 5.3(b)**. Also, the randomly oriented recrystallized grains with grain size in the range between 13-72 µm were found to develop at the surface region and along the grain boundaries of the large hot bands as indicated by white arrows in **Fig. 5.3(b)**. GOS map for the region shown in **Fig. 5.3(b)** is represented in **Fig. 5.3(c)**. The fine recrystallized grains can be clearly recognized by their low GOS values (<0.05) as indicated by white arrows in **Fig. 5.3(b, c)**. The high shear deformation, arising near the surface layers due to sticking friction during HR, was expected to cause dynamic recrystallization which promoted fine recrystallized grains at the surface. On the other hand, the strain incompatibility between two different oriented grains was expected to induce large triaxial stress, encouraging dynamic recrystallization to occur at the grain boundaries. Among these fine recrystallized grains, only few have Goss orientation. The heavily deformed large hot bands can be distinguished by their higher GOS values as compared to the undeformed large grains, **Fig. 5.3(c)**. Interestingly, some of the large grains with low GOS values were found to have Goss orientation, as indicated by red arrows in **Fig. 5.3(b, c)**.

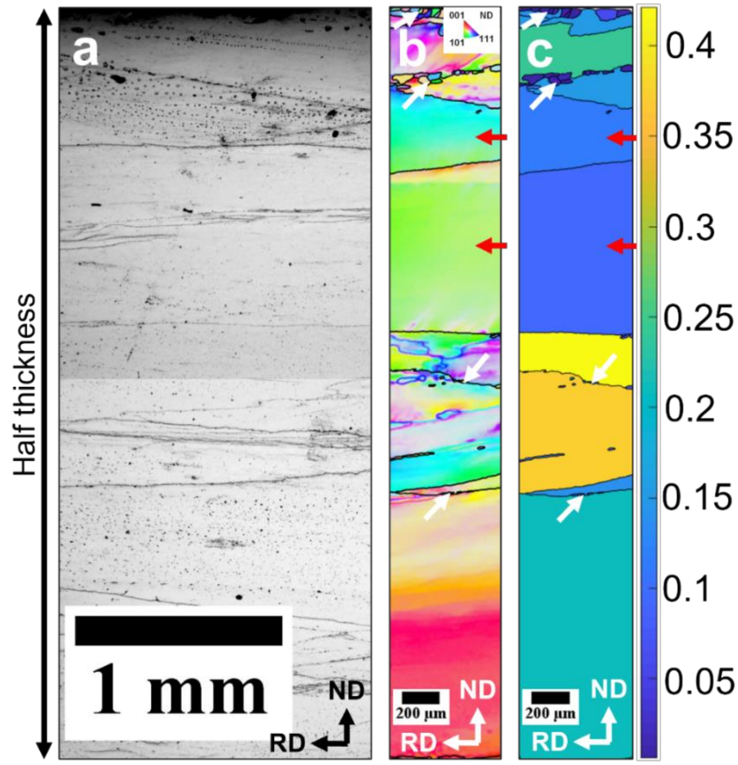

Figure 5.3: (a) Optical micrograph after HR from surface to center through the thickness along ND-RD cross-section, (b) IPF-ND map of the HR sample through 50% of the thickness along ND-RD cross-section, (c) Grain Orientation Spread (GOS) map of the region (a) showing recrystallized and deformed grains

5.4 Microstructure and Microtexture Development after Hot Band Annealing

Fig. 5.4(a) shows the through thickness microstructure of HBA sample from surface to center. In comparison to the hot rolled microstructure, higher fraction of the recrystallized grains has been observed. Moreover, some of the large hot bands remained unrecrystallized after annealing. IPF map of the investigated sample is shown in, **Fig. 5.4(b)**. Goss oriented grains were significantly found to be present as indicated by white arrows in **Fig. 5.4(b)**. The rotated cube oriented grains were observed to remain unrecrystallized at the mid-thickness region after HBA. The unrecrystallized grains were observed all over the thickness, while the recrystallized grains were found to evolve either at surface layers or near the grain boundaries. GOS map for the region, **Fig. 5.4(b)**, was constructed as shown in **Fig. 5.4(c)**. The recrystallized grains indicated by white arrows possess low GOS values (<0.05) compared to the unrecrystallized grains indicated by red arrows, **Fig. 5.4(b, c)**. The recrystallized grain size varied in the range of 44-271 μm and no preference on crystallographic orientation has been observed in these grains. In addition to rotated cube oriented grains, the Goss oriented grains which remained less deformed during HR, **Fig. 5.3(b, c)** did not recrystallized during HBA, **Fig. 5.4(b, c)**. Grain growth was also prominent in the hot band annealed structure.

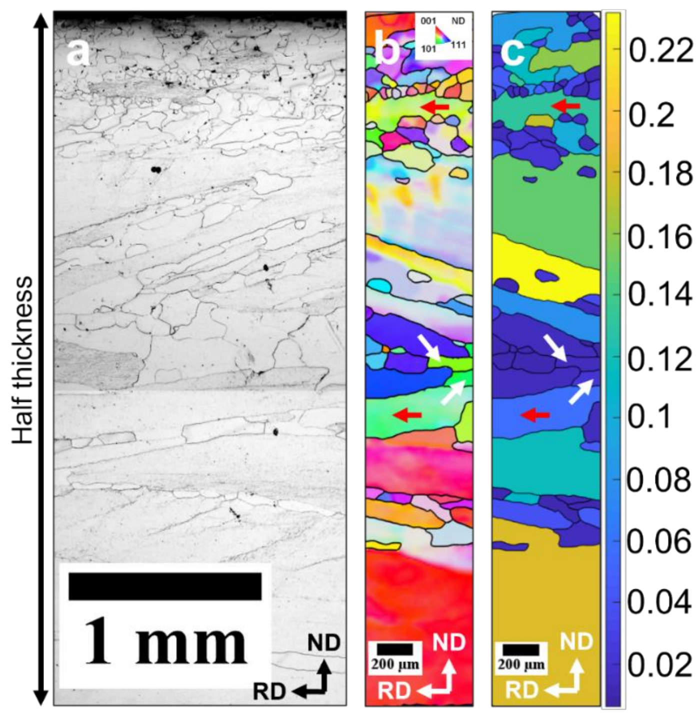

Figure 5.4: (a) Optical micrograph of the sample A from surface to center through the thickness along ND-RD cross-section, (b) IPF-ND map of the sample A through 50% of the thickness along ND-RD cross-section, (c) Grain Orientation Spread (GOS) map of the region (a) showing recrystallized and unrecrystallized grains

5.5 Microstructure and Microtexture Development after Intermediate Cold Rolling

The microstructure of the ICR sample is shown in **Fig. 5.5(a)**. Strain accumulation during ICR was found to be inhomogeneous. In some of the grains at different thickness level, the amount of deformation was observed to be high as marked by black arrows in **Fig. 5.5(a)**. The IPF map of the ICR sample is shown in **Fig. 5.5(b)**. ODF was also constructed based on the region shown in **Fig. 5.5(b)** and is represented in **Fig. 5.5(c)**. α-fiber texture was developed with strong intensity of {112}<110> orientation. Medium intensity of γ-fiber texture components was also observed after ICR. Grains having rotated cube orientation at the mid thickness were found to accumulate less deformation. Whereas the deformation of differently oriented grains at regions away from center was observed to be comparatively high. The high strain accumulation inside some of the grains causes instability in the deformed structure as exhibited by dark colored regions in **Fig. 5.5(b)**. These dark colored highly strained regions were inclined at certain angle from RD, denoting shear band formation as indicated by white arrows in **Fig. 5.5(b)**. The shear bands were found to develop inside grain having {111}<112> component of γ-fiber texture as marked by dotted white rectangle in **Fig. 5.5(b)**. For further confirmation, ICR sample was subjected to partial recrystallization at 650° C for 10 min. The microstructure of the partially recrystallized sample is shown in **Fig. 5.5(d)**. As expected, recrystallization has been found to initiate along the inclined line of shear band due to high accumulation of shear strain (T Haratani et al. 1984).

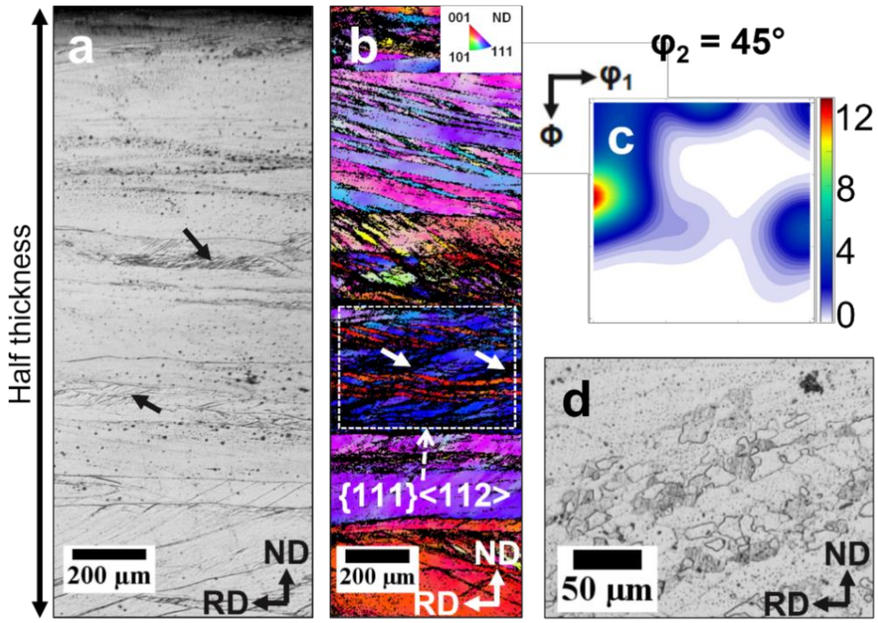

Figure 5.5: (a) Optical micrograph after ICR from surface to center along ND-RD cross-section, (b) IPF-ND map of the ICR sample through 50% of the thickness along ND-RD cross-section, (c) $\varphi_2 = 45°$ ODF map based on Bunge notation of the region shown in (b), and (d) Optical micrograph of shear band region after partial recrystallization of the ICR sample at 650° C for 10 min

5.6 Microstructure and Microtexture Development after Intermediate Annealing

Optical microstructure of the IA sample is shown in **Fig. 5.6(a)**. Unlike HBA, complete recrystallization of the grains throughout the thickness occurred after IA. The grain size varied in the range of 8 µm to 241 µm. The IPF map of the IA sample is shown in **Fig. 5.6(b)**. ODF was constructed for the region, **Fig. 5.6(b)**, as shown in **Fig. 5.6(c)**. A weak texture was developed containing grains distributed with random orientations all over the thickness. Interestingly, the presence of Goss orientation has been observed in the IA sample.

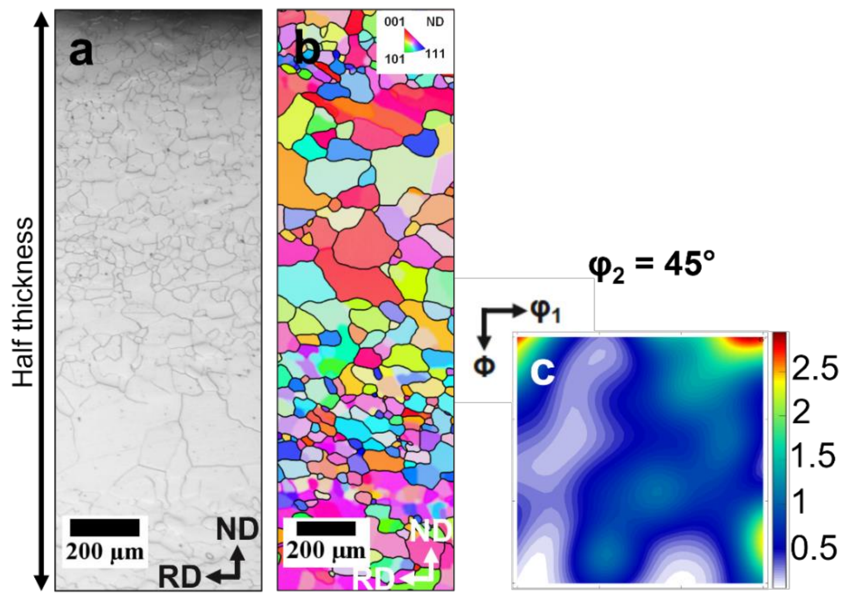

Figure 5.6: (a) Optical micrograph after IA from surface to center through the thickness along ND-RD cross-section, (b) IPF-ND map of the IA sample through 50% of the thickness along ND-RD cross-section, (c) $\varphi_2 = 45°$ ODF map based on Bunge notation of the region shown in (b)

5.7 Microstructure and Microtexture Development after Complete Cold Rolling

The optical microstructure of the CCR sample is shown in **Fig. 5.7(a)**. The distribution of relatively small sized grains after IA with respect to that after HBA, thereupon, promoted more homogeneous deformation in the CCR sample as compared to ICR sample. Band contrast map of the CCR sample is shown in **Fig. 5.7(b)**. The deformation at some regions produced elongated grains as indicated by yellow arrows in **Fig. 5.7(b)**. On the other hand, severe grain fragmentation was observed in most of the regions. The high strain accumulated around the deformed sub-grain structure resulted in low band contrast as indicated by white arrows in **Fig. 5.7(b)**. IPF map of the CCR sample is also shown in **Fig. 5.7(c)**. Similar to the ICR sample, there were some evidences of shear band formation during cold rolling (CCR) after IA, and the shear bands were limited to grains having {111}<112> orientation. However, the area fraction covering the shear band regions in CCR was considerably less. ODF constructed for the region,

Fig. 5.7(c), is exhibited in **Fig. 5.7(d)**. The deformed grains were occupied by mostly α- and γ-fiber texture components. Similar to the ICR sample, the intensity of Goss orientation was found to be negligible after CCR, **Fig. 5.7(d)**.

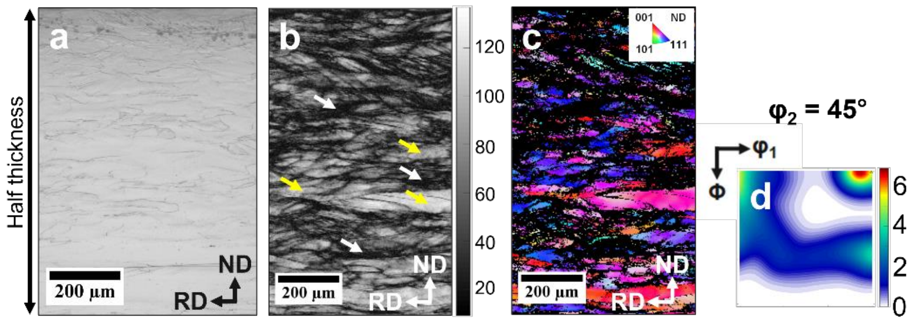

Figure 5.7: (a) Optical micrograph after CCR from surface to center through the thickness along ND-RD cross-section, (b) Band contrast map of the CCR sample from surface to center through the thickness along ND-RD cross-section, (c) IPF-ND map of the region shown in (b), and (d) φ_2 = 45° ODF map based on Bunge notation of the region shown in (c)

5.8 Microstructure and Texture Development after Single stage Cold Rolling

The microstructure of SCR sample is shown in **Fig. 5.8(a)**. The appearance of dark lines in the optical microstructure infers that some of the grains were subjected to heavy deformation as indicated by black arrows in **Fig. 5.8(a)**. EBSD analysis was conducted after SCR and the band contrast map is shown in **Fig. 5.8(b)**. SCR promoted shear band formation at most of the regions of the cold rolled sheet except mid-thickness region. The IPF and ODF maps for region shown in **Fig. 5.8(b)** were then generated as shown in **Fig. 5.8(c, d)**, respectively. α- and γ-fiber texture components along with {552}<232> orientation was observed to develop. The shear bands were observed to develop inside γ-fiber textured and {552}<232> oriented grains as indicated by white arrows in **Fig. 5.8(c)**. In addition, the propensity of shear bands was certainly increased. The orientation inside the shear band region could not be indexed due to large strain accumulation. However, for further confirmation, the SCR sample was subjected to annealing at 650° C for 10 min. The IPF map of the partially annealed sample has been shown in **Fig. 5.8(e)**. Clearly, the Goss oriented grains were found to develop along the shear bands. A detailed study on the formation of Goss orientation inside the shear bands has been shown in **Chapter 6** (Jain, Modak, et al. 2022).

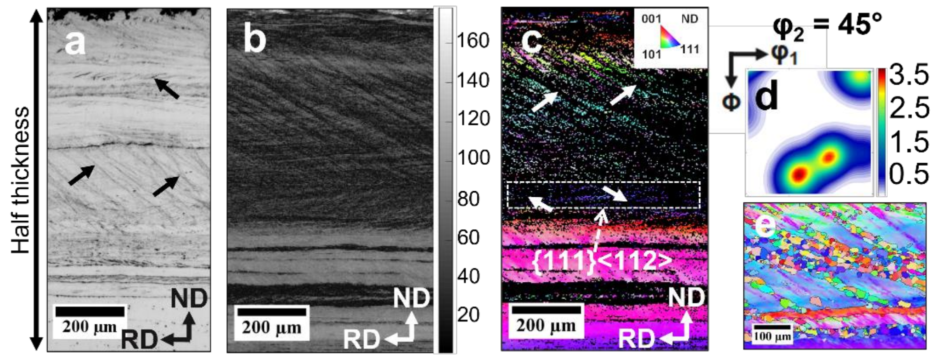

Figure 5.8: (a) Optical micrograph after SCR from surface to center along ND-RD cross-section, (b) Band contrast map of the SCR sample from surface to center through the thickness along ND-RD cross-section, (c) IPF-ND map of the region shown in (b), (d) φ_2 = 45° ODF map based on Bunge notation of the region shown in (c), and (e) IPF-ND map of partially recrystallized shear band region in the SCR sample at 650° C for 10 min

5.9 Macrotexture analysis of different cold rolled and intermediate annealed samples

In order to estimate the crystallographic texture from larger representative sample volume, macrotexture analysis has been carried out. ODF maps showing macrotexture of the ICR, IA, CCR, and SCR samples are shown in **Fig. 5.9(a-d)**, respectively. The volume fraction of major texture components was calculated from those ODFs with 15° threshold and is given in **Table 5.1**. The major texture components were rotated cube orientation and γ-fiber texture. The volume fraction of Goss orientation after ICR was less than 1%. After IA treatment, Goss orientation was also observed to increase, **Table 5.1**. However, in CCR sample, the volume fraction of Goss orientation again decreased. Typical rolling textures such as, α- and γ-fiber textures were developed in the SCR sample, **Fig. 5.9(d)**.

Importantly, the volume fraction of Goss orientation was found to be negligible after SCR, **Table 5.1**.

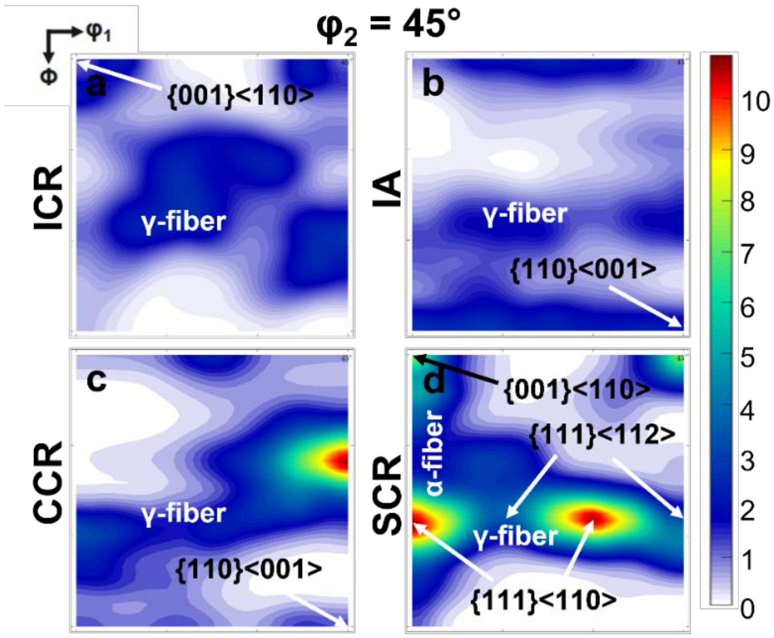

Figure 5.9: φ_2 = 45° ODF maps based on Bunge notation showing macrotexture analysis performed on quarter thickness along RD-TD plane after (a) Intermediate cold rolling (ICR), (b) Intermediate annealing (IA), (c) Complete cold rolling (CCR), and (d) Single stage cold rolling (SCR)

Table 5.1: Volume % of various orientations based on macrotexture analysis of ICR, IA, CCR, and SCR samples

Sample	{110}<001> (Goss)	{111}<112>	{111}<110>	{001}<110>
ICR	0.7	8.0	5.2	4.0
IA	3.1	6.2	5.0	1.9
CCR	1.6	7.0	8.2	1.1
SCR	0.3	12.3	21.7	7.6

5.10 Microstructure and Microtexture Development after Primary Recrystallization

Primary recrystallization (PR) study was attempted on SCR sample at different temperatures starting from 550° C up to 700° C for 30 min duration in air and IPF maps are presented in **Fig. 5.10(a-e)**. In case of the lowest annealing temperature at 550° C, no trace of recrystallization has been noticed, **Fig. 5.10(a)**. Even the areas inside the shear bands were not recrystallized. After increasing the recrystallization temperature to 625° C, the high strain regions such as, shear bands, started recrystallizing, whereas the other regions remained almost unrecrystallized, **Fig. 5.10(b)**. On further increasing the annealing temperature, the recrystallized regions increased as shown in **Fig. 5.10(c, d)**. Some large hot bands at the mid-thickness region remained unrecrystallized at 650° C. However, at 675° C, the structure got completely recrystallized and some considerable amount of grain growth has been observed in few grains. Annealing at 700° C causes extensive grain growth as indicated by white arrow in **Fig. 5.10(e)**. The grain size distribution after PR done at 625° C, 650° C, 675° C, and 700° C is also given below each IPF map as shown in **Fig. 5.10(f-i)**, respectively. The purpose of PR was to develop fine homogeneous distribution of recrystallized grains without grain growth. Therefore, both 650° C and 675° C can be considered as the optimum PR temperature having grain size (mode value) between 20-25 µm. ODFs were generated for the regions shown in **Fig. 5.10(a-e)** as represented in **Fig. 5.10(j-n)**, respectively. Mostly α- and γ-fiber texture components were observed before recrystallization, **Fig. 5.10(a, j)**. After partial recrystallization, Goss oriented grains started evolving and the intensity γ-fiber texture components decreased, **Fig. 5.10(b, k)**. Further, on increasing the PR temperature, the intensity of γ-fiber texture components reduced, **Fig. 5.10(c, l)** and **Fig. 5.10(d, m)**. The uncrystallized regions at the mid-thickness region were mostly occupied by rotated cube orientation, **Fig. 5.10(c, h)**. However, with the substantial grain growth occurred, **Fig. 5.10(e)**, an orientation slightly deviated from Goss orientation started developing as indicted by black arrow in **Fig. 5.10(n)**.

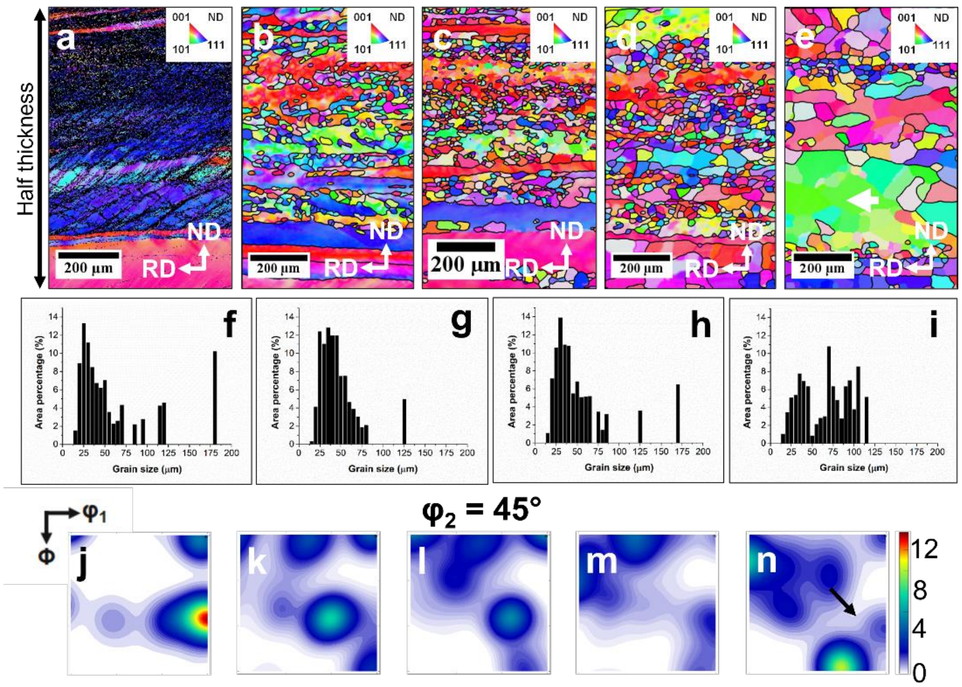

Figure 5.10: IPF-ND maps of half thickness along ND-RD cross-section after the attempt of PR at (a) 550° C, (b) 625° C, (c) 650° C, (d) 675° C, and (e) 700° C, respectively, under air atmosphere, grain size distribution after PR at (f) 625° C, (g) 650° C, (h) 675° C, and (i) 700° C, and (j, k, l, m, n) φ_2 = 45° ODF maps based on Bunge notation of the regions shown in (a, b, c, d, e), respectively

5.11 Microstructure and Microtexture Development after Secondary Recrystallization

Secondary recrystallization (SR) was attempted at 1200° C in vacuum on the primary recrystallized samples annealed at 550° C, 650° C and 700° C as shown in **Fig. 5.11(a-c)**. The recrystallized microstructure was composed of large grains (wt. average size >1 mm) with random orientations except the sample subjected to PR at 700° C. In case of the sample primary recrystallized at 700° C, a single grain having {001}<120> orientation was found to occupy the complete thickness after SR at 1200° C, **Fig. 5.11(c)**. The orientation of the coarse grains was not necessarily the desired Goss orientation. Since the grain growth was almost completed within short time period of 5 min, SR then has been attempted at lower temperature range to capture the grain growth mechanism.

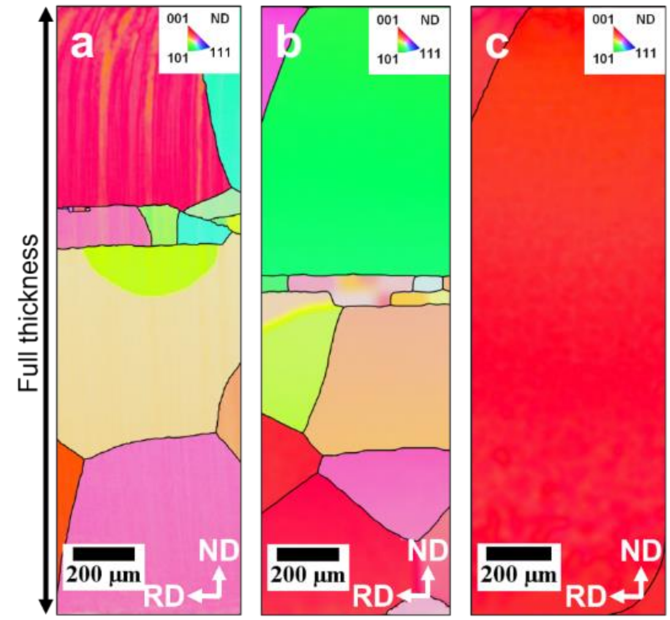

Figure 5.11: (a, b, c) IPF-ND maps showing full thickness of ND-RD cross-section after the attempt of SR at 1200° C under vacuum on PR samples annealed at 550° C, 650° C, and 700° C, respectively

SR has been carried out at 900° C, 950° C and 1000° C on the sample which was primary recrystallized at 650° C. The IPF maps and ODFs are shown in **Fig. 5.12(a-f)**. The duration of annealing has been restricted to 1 min only. In case of SR at 900° C and 950° C, a complete recrystallization without considerable grain growth has been observed, **Fig. 5.12(a, b)**. Further increase in SR temperature to 1000° C caused grain growth, **Fig. 5.12(c)**. The grain growth was not restricted to a specific orientation and abnormal grain growth could not be achieved. However, significant amount of Goss orientation was present in all the cases, **Fig. 5.12(d-f)**.

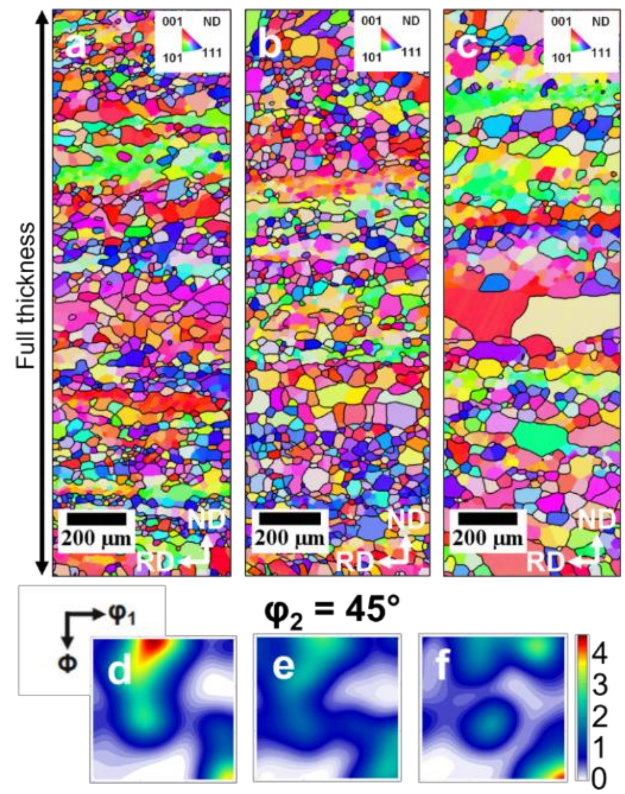

Figure 5.12: Through thickness IPF-ND maps along ND-RD cross-section after the attempt of SR at (a) 900° C, (b) 950° C, and (c) 1000° C, respectively, under vacuum on PR samples annealed at 650° C, (d, e, f) φ_2 = 45° ODF maps based on Bunge notation of the regions shown in (a, b, c), respectively

5.12 Characterization on the formation of precipitates

Precipitates were reported to have a great impact on the evolution of the microstructure during secondary recrystallization (Ushigami et al. 1998). In the present study, DSC was used to analyze the formation and dissolution of precipitates in the investigated steel during cooling and heating cycle. The heat flow curves during continuous heating and cooling of the HBA sample are shown in **Fig. 5.13(a)**. During heating, two significant endothermic peaks appeared at 735° C K and 1187° C, while during cooling, heat flow exchange curve shows four exothermic peaks at 1182° C, 987° C, 869° C and 733° C. The exothermic peaks appearing at 1182° C and 733° C are well complementing with the observed endothermic peaks. On the other hand, the occurrence of two additional weak peaks at 987° C and 869° C were not supported by the endothermic peaks during heating, and therefore were not conclusive. In order to correctly identify the start and end temperature of the transformations, first derivative of DSC curves (DDSC) for heating and cooling were also plotted with temperature as shown in **Fig. 5.13(b)**. For the first endothermic peak during heating, the DDSC curve started deviating from base line at 731° C and ends at 743° C. The onset temperature of second DDSC peak during heating was observed to be 1161° C and the finishing temperature was 1235° C. Similarly, the start and finish temperatures of the corresponding exothermic peaks during cooling can also be identified from the DDSC plot as indicated by arrows in **Fig. 5.13(b)**. The endothermic (during heating) and exothermic (during cooling) peaks at 735° C and 733° C, respectively, as shown in **Fig. 5.13(a)**, represents the magnetic transition temperature of Fe-3.78 wt. % Si steel and similar observation has made in other studies (Sopko et al. 2014, Yuan et al. 2007). On the other hand, according to thermodynamic prediction, the MnS and AIN precipitation was expected to occur below 1198° C and 937° C, **Fig. 5.1(b)**. The formation of MnS precipitates was accompanied by heat absorption at 1187° C and heat release at 1182° C during heating and cooling cycles, respectively, **Fig. 5.13(a, b)**. The heat release at 869° C during cooling may have been due to the precipitation of AIN. However, the heat absorption peak of AIN precipitation during heating cycle was not observed. Also, the heat flow changes occurred at 987° C in cooling curve was not understood.

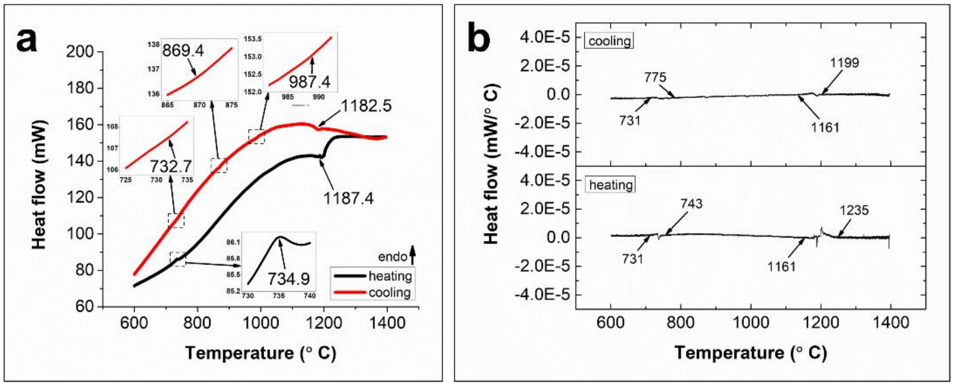

Figure 5.13: (a) Heat flow exchange curves after conducting DSC on HBA sample showing heating and cooling cycles at the rate of 5° C/min, and (b) first derivative of DSC (DDSC) heating and cooling curves shown in (a)

The morphology of second phase particles evolved during HBA and PR stages samples are shown in **Fig. 15(a, b)** and the corresponding EDS spectrums are also represented in **Fig. 15(c, d)**, respectively. The second phase particles were found to be the oxides of Al having around 5 µm particle size. Neither the presence of AlN nor MnS precipitates were detected in the investigated samples under optical microscope and FESEM. It appears that Al particles might have oxidized during melting.

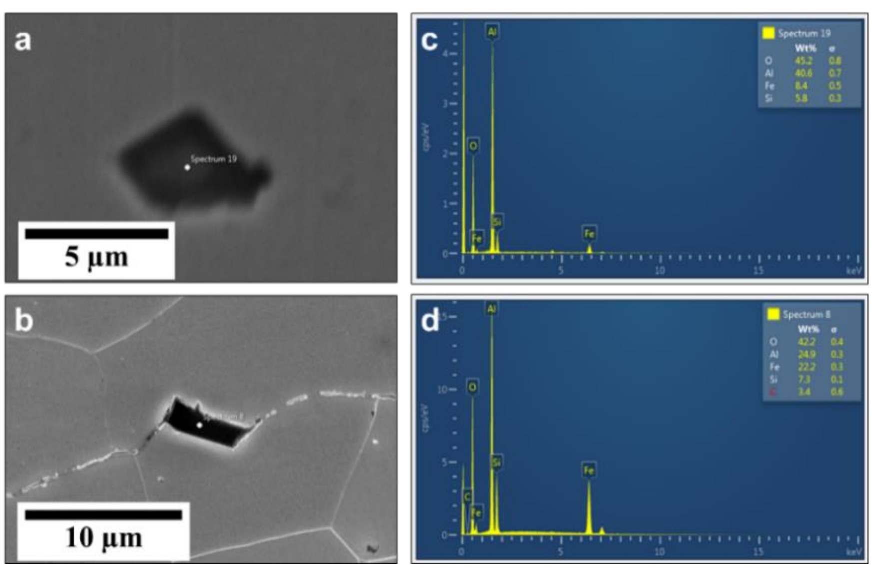

Figure 5.14: Morphology of precipitates after (a) HBA and (b) PR stages, and (c, d) EDS spectrums of (a, b), respectively

Transmission electron microscopic analysis has been conducted on the HR samples as shown in **Fig. 5.15(a-f)**. The presence of fine precipitates having size less than 10 nm were noticed in the bright field images, **Fig 5.15(a, d)**. The selected area diffraction pattern of regions corresponding to **Fig. 5.15(a)** and **Fig. 5.15(d)** are shown in **Fig. 5.15(b)** and **Fig 5.15(e)**, respectively. Further, the dark field images constructed with the selected diffraction spots (marked with red circles in **Fig. 5.15(b, e)**) confirm the presence the fine precipitates, **Fig. 5.15(e, f)**. However, the nature of the precipitates could not be confirmed in the present study. More detailed analysis is required to confirm the nature of those nano precipitates.

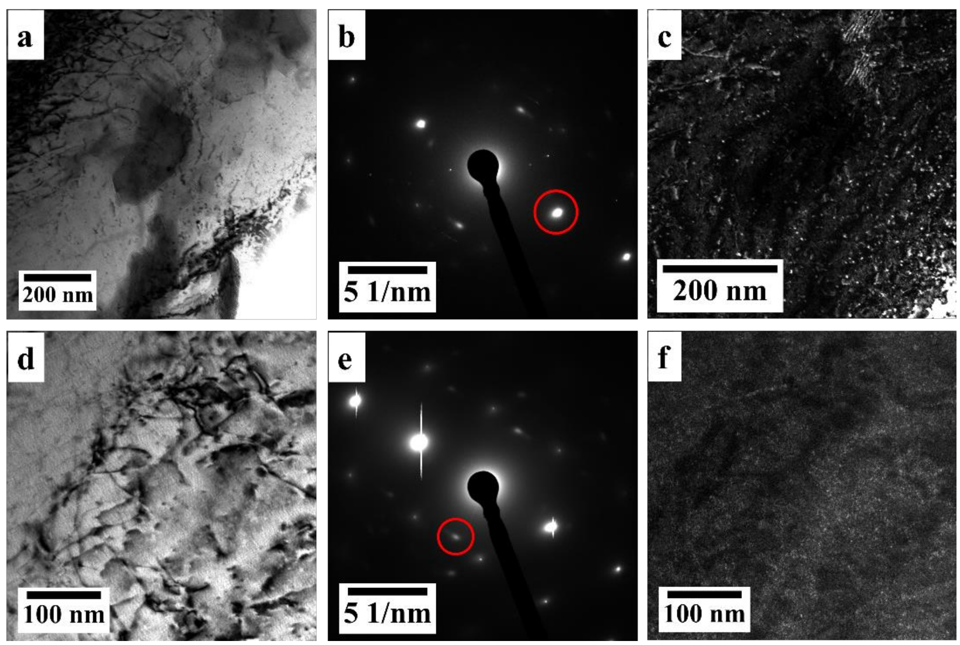

Figure 5.15: Transmission electron micrographs of the hot rolled samples showing (a, d) bright field images, (b, e) corresponding selected area diffraction patterns, and (c, f) dark field images constructed with the selected diffraction spots marked with red circles in (c, d), respectively

5.13 Discussion

Understanding the evolution of Goss orientation in CRGO steel was the prime objective of the present study. This section critically examines the role of different processing steps on GOSS texture development.

Grain size of the as cast sample was extremely large (>5 mm). After HR, most of the regions throughout thickness were covered by large unrecrystallized grains. Whereas few grains close to the surface region were recrystallized. Interestingly, the existence of GOSS orientation has been found in both fine recrystallized and coarse deformed zone, **Fig. 5.3(b, c)**. The large elongated Goss oriented grains were derived from the reheated structure. Pan et al. (Pan et al. 2016) reported that the initial columnar grains strongly affect the microstructure and texture development after cold rolling deformation. On the other hand, the fine recrystallized Goss oriented grains, observed near the surface regions were the product of dynamic recrystallization. Similar observation on the development of Goss texture at the surface during HR has been reported in other studies (Böttcher et al. 1993, Inokuti 1996). HBA at 800° C leads to finer structures with higher fraction of recrystallized grains, **Fig. 5.4(a, b)**. However, the grains either at the mid thickness region or having Goss and rotated cube orientations mostly remained unrecrystallized, **Fig. 5.4(b, c)**. The strain accumulation during HR in those orientations was low as compared to the other orientations. Low in-grain misorientation in rotated cube orientation has been reported in other studies (Raabe et al. 2002) as well. Moreover, grain growth of the fine recrystallized Goss oriented grains has also been observed during HBA. Thus, both unrecrystallized and recrystallized Goss oriented grains were present after HBA.

Deformation during cold rolling was heterogeneous and shear bands were developed. The susceptibility of shear banding was dependent on the grain orientation and the amount of thickness reduction. The common rolling textures such as, α- and γ-fiber, developed during cold rolling operations, **Fig. 5.5(b)** and **5.8(b)**. Shear banding was not observed inside the grains having rotated cube orientation which mostly existed at the mid-thickness region of the sheet. Mostly, the shear bands were formed inside {111}<112> oriented grain in ICR sample as shown in **Fig. 5.5(b)**. On increasing the cold rolling strain, the density of shear bands enhanced, **Fig.**

5.8(b). And the orientations other than γ-fiber texture components, such as {552}<232> orientation, were also found to accommodate shear bands. In general, crystallographic orientations having high Taylor factor are known to promote high dislocation activities or high shear strain (SHIN et al. 2008, Nguyen-Minh et al. 2012, Mehdi et al. 2020, Jain, Modak, et al. 2022). The increase in dislocation densities during high strain deformation induces strain hardening which may promote instability in the form of shear bands. Taylor factor maps for the regions shown in **Fig. 5.5(b)** and **5.8(b)** were generated for plane strain compression considering {110}<111> and {112}<111> slip systems and are represented in **Fig. 5.16(a)** and **(b)**, respectively. High Taylor factor of {111}<112> orientation has facilitated the shear band formation during ICR, **Fig. 5.16(a)**. Further, the region inside the shear band undergo crystal rotation which contributes to geometrical softening phenomenon (Nguyen-Minh et al. 2012). In our recent work it has been demonstrated in detail that the crystal rotation inside the shear bands of {111}<112> orientation leads to the formation of Goss orientation under plane strain compression (Jain, Modak, et al. 2022).

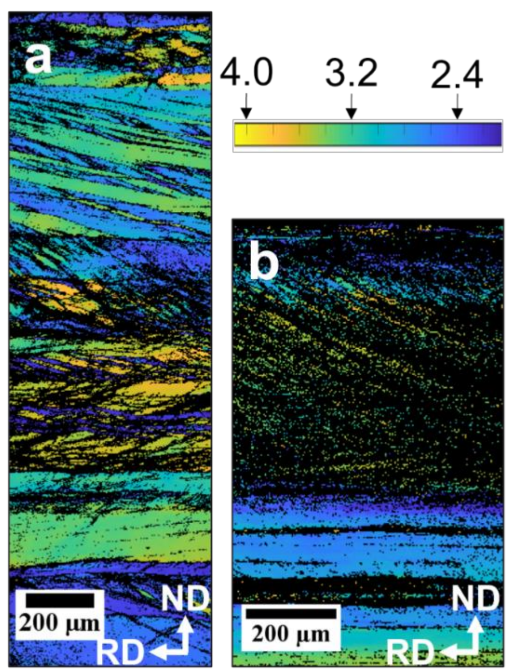

Figure 5.16: (a, b) Taylor Factor maps under plane strain compression generated for the regions shown in Fig. 7(b) and 10(c), respectively

On the other hand, macrotexture study confirms that overall, the intensity Goss orientation was negligible after ICR, **Fig. 5.9(a)**. Although, through thickness EBSD study portrayed that a sufficient amount of Goss orientation was present after HBA, **Fig. 5.4(b)**. This indicates that even if Goss texture was present before the cold rolling stage, they were unstable under heavy cold rolling operation. Similar conclusion has also been reported in other studies (Mehdi et al. 2019, Jain, Modak, et al. 2022). The Goss oriented grains were again found to develop after the IA treatment, **Fig. 5.9(b)**. In this regard, some study reported that an intermediate annealing treatment was essential to ensure the survival of Goss orientation during cold rolling (Song et al. 2021). This can be true if Goss oriented grains developed after HBA remained the only source of Goss orientation. In case of SCR, in addition to increase in the density of shear bands, the percentage of Goss orientation was reduced further as shown in **Table 5.1**. The shear bands act as the preferential nucleation site during recrystallization since high deformation is concentrated inside those bands, **Fig. 5.15(b)**. And Goss oriented grains started originating from the shear band region, **Fig. 5.8(e)**. It demonstrated that here, the source of Goss orientation during subsequent annealing treatment was not the preexisting Goss oriented grains which existed before cold rolling. Similarly, Atake et al. (Atake et al. 2015) also demonstrated that the recrystallization texture shows no sign of the formation of Goss orientation when there was no shear banding occurred during cold rolling. Therefore, the intermediate annealing should not be considered as an essential step to achieve Goss orientation.

After SCR, the steel was subjected to PR to achieve strain free recrystallized grains without considerable grain growth (Lin et al. 1996, Shimizu et al. 1989). In the present investigation, Fe-Si steel started recrystallizing on and above 625° C. The through thickness EBSD study clearly demonstrate that Goss oriented grains were present in the primary recrystallized structures, **Fig. 5.10(b-d)**. Abnormal grain growth of primary recrystallized Goss oriented grains was expected to take place during SR.

However, in the present study abnormal grain growth of Goss oriented grains could not be achieved, and the final texture achieved after SR was not Goss orientation, **Fig. 5.11, 5.12**. Many theories in the literature have been presented on the growth advantage of Goss orientation in CRGO steel (Inokuti 1996, Hayakawa et al. 1998, Ushigami et al. 1998, Hayakawa et al. 2002, Guo et al. 2010). Different factors which were expected to influence the abnormal grain growth, have been considered separately to identify the reason(s) for not achieving Goss orientation in the final microstructure. Grain size and grain boundary character of Goss oriented grains may have a significant role. The weighted average grain size of Goss oriented grains has been compared with those of the overall grains after PR and SR as listed in **Table 5.2**. Clearly, the Goss oriented grains had size advantage similar to other studies (Hillert 1965).

Table 5.2: Weighted average grain size of Goss oriented grains and all grains after PR (650° C and 675° C) and SR (950° C and 1000° C)

Sample	PR at 650° C	PR at 675° C	SR at 950° C	SR at 1000° C
wt. average grain size of Goss oriented grains	43.8	83.1	68.1	155.4
wt. average grain size of all grains	43.7	51.0	58.8	91.4

The boundary distribution based on misorientation angle of Goss oriented grains has also been compared with all grains as shown in **Fig. 5.17(a-d)**. Park et al. (Park et al. 2009) reported that the low angle grain boundaries (<15° misorientation) inside the Goss oriented grains, induces low grain boundary movement which further impose growth restriction during SR and enhanced the growth of randomly oriented grains. However, in the present, the Goss oriented grains were free from low angle boundaries (<15°), **Fig. 5.17(a-d)**. The percentage of grain boundaries after PR having misorientation angle between 20°-45° was found to be around 65-70%, whereas those covered by Goss oriented primary grains were in between

70-80%, **Fig. 5.17(a-d)**. The grain boundaries having misorientation angle between 20°-45° were considered to be HE grain boundaries which promotes high grain boundary diffusion and migration rates (Hayakawa et al. 1998, Rajmohan, J. . Szpunar, et al. 1999). The higher percentage of these HE grain boundaries, surrounding Goss oriented primary grains, were then expected to have growth advantage.

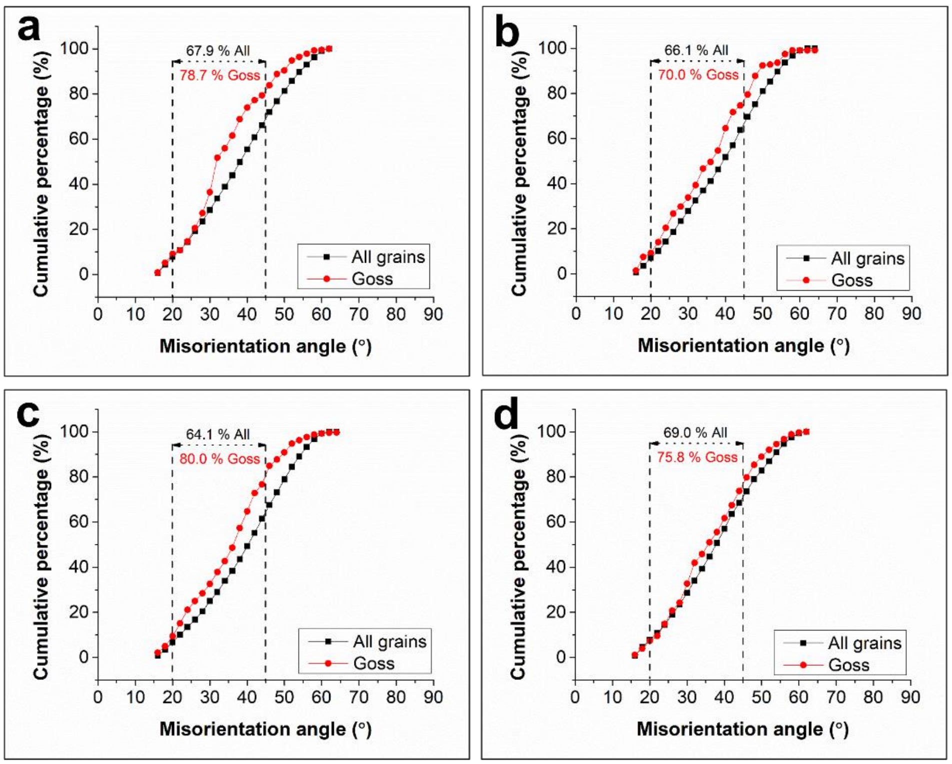

Figure 5.17: Cumulative percentage of the grain boundaries based on the misorientation angle after PR conducted at (a) 650° C and (b) 675° C for 30 minutes in air, and (c, d) after SR performed at (c) 950° C and (d) 1000° C for 1 minute under vacuum

Similarly, the CSL (Σ3-Σ35) boundary fraction has also been evaluated separately for Goss oriented grains and all other grains. The CSL boundary percentage has been found to be extremely low (<1%) and were almost constant for both the cases in all PR and SR samples. Some studies reported that low fraction of CSL boundaries is inappropriate for selective grain growth (Imamura et al. 2013, Hayakawa 2017). Grain boundary curvature is among one of the major factors reported to be responsible for abnormal grain growth (Searcy 1986). In case of recrystallized microstructure, the pressure difference arising because of the difference of the grain boundary curvature was expected to provide growth advantage to the grains having convex boundaries (Andersen et al. 1995, Lu et al. 2020). These convex boundaries promote grain growth in the direction towards the center of the curvature and in this process the neighboring grains having concave boundaries were expected to be consumed. The grain boundary curvature has been calculated for all the grains and Goss oriented grains (within 15° deviation) evolved during different conditions of PR (650° C and 675° C) and SR (900° C, 950° C and 1000° C) as depicted in **Fig. 5.18(a-f)**. The estimated curvature (1/r) of a single Goss oriented grain has been represented in **Fig. 5.18(a)**. Here the convex boundaries are having negative curvature which are indicated by blue color. Similarly, the distribution of boundary curvature has been estimated separately for Goss oriented grains and all grains for given PR and SR conditions, **Fig. 5.18(b-f)**. The analysis indicates that the percentage of concave boundaries were always higher than convex boundaries for both the groups (all grains and Goss oriented grains) in all samples. But when the percentage of convex boundaries around Goss oriented grains and all grains were compared, the Goss oriented grains showed higher magnitude. Therefore, the Goss grains had an advantage from curvature perspective over grains having different orientations, though, it might not be sufficient to cause abnormal grain growth since major boundaries were concave in nature.

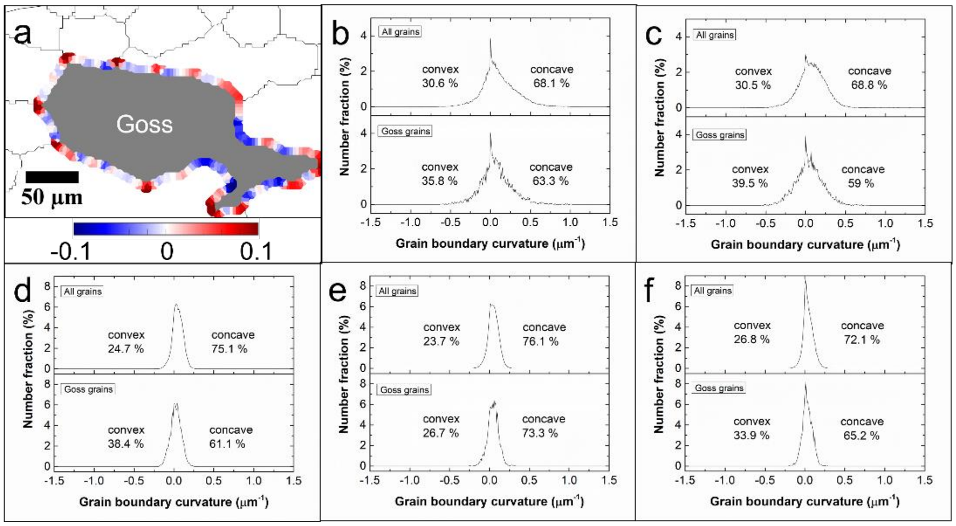

Figure 5.18: (a) Grain boundary curvature plot for single Goss oriented grain, (b) Number fraction (%) of grain boundary curvature for Goss oriented grains and all grains after primary recrystallization done at (b) 650° C and (c) 675° C, and after secondary recrystallization done at (d) 900° C, (e) 950° C, and (f) 1000° C

Many studies reported that the role of precipitates or inhibitors is significant in case of abnormal grain growth (Park et al. 2002, Fang et al. 2016, Fang et al. 2017, Bao et al. 2017). In the present study, some indication on the formation of MnS precipitates has been obtained by conducting DSC test as shown in **Fig. 5.13(a, b).** However, the presence MnS could not be confirmed in FESEM. A detailed precipitation study employing transmission electron microscope is necessary to get further insight.

5.14 Conclusions

The following conclusions can be drawn from the present study:

a) Goss oriented grains were developed during hot rolling and hot band annealing stages. Subsequently, these pre-existing Goss oriented grains become unstable during cold rolling. Macrotexture study revealed that the volume fraction of Goss orientation was negligible after cold rolling.

b) Shear bands were formed inside {111}<112> component of γ-fiber texture during cold rolling. Partial recrystallization study indicates that Goss oriented grains were developed inside those shear bands.

c) The optimum primary recrystallization was found in between 650-675° C. Subsequently, secondary recrystallization was attempted between 900° C to 1200° C. Despite the presence of considerable amount of Goss oriented grains, abnormal grain growth was not achieved in the final microstructure.

d) The percentage of concave grain boundaries was found to be higher than that of convex boundaries after primary and initial stage of secondary recrystallization. But the percentage of convex boundaries around Goss oriented grains were higher compared to those around other grains. However, it was found insufficient to cause abnormal grain growth.

CHAPTER 6

Origin of Goss texture in cold rolled grain oriented steel: Role of shear bands

6.1 Introduction

Goss oriented grains usually evolves as recrystallized grains during primary recrystallization step which subsequently develop Goss texture during the secondary recrystallization by abnormal grain growth (Hayakawa 2017). Despite of its various advancement in performance and production route, the exact mechanism of the evolution of Goss texture in high silicon polycrystalline GO steel is still debatable in scientific community (T Haratani et al. 1984, Matsuo et al. 1986, Mishra et al. 1986, Böttcher et al. 1993, I Samajdar et al. 1998, SHIN et al. 2008, Atake et al. 2015, Kim et al. 2014) as shown in **Table 6.1**.

It was reported that the Goss oriented grains, originated during hot rolling at the surface of the rolled plate due to shear deformation, gets retained after cold rolling which subsequently develops Goss texture during the final annealing processes (Kim et al. 2014, Matsuo et al. 1986, Mishra et al. 1986, Böttcher et al. 1993). Dorner et al. (Dorner et al. 2007) showed that Goss orientation rotates towards {111}<112> component of γ-fiber texture during cold rolling subjected to the formation of shear bands and microbands. They indicated that the change in slip systems inside the microbands compensated the overall rotation of the matrix retaining the initial Goss oriented grains. Moreover, a recent work (Mehdi et al. 2019) demonstrated three possible locations of Goss orientation such as shear bands and microbands in {111}<112> oriented grains and the grain boundaries between {111}<112> and {113}<361> oriented grains in the polycrystalline Fe-2.8%Si steel. The initial Goss oriented grains were reported to get retained after cold rolling irrespective of their location of existence. Another recent work by Giri et al. (Giri et al. 2020) has also suggested that Particle Stimulated Nucleation (PSN) can be the primary origin of Goss orientation in CRGO steel.

Furthermore, some studies (Ushioda et al. 1989, T Haratani et al. 1984) on the single crystal of Fe-Si steel have suggested that Goss orientation may evolve through the shear band formation during cold rolling. Severe deformation during the cold rolling process causes dislocation pile up and further deformation induces instability leading to the formation of shear bands. It has been showed that shear bands may form in different single crystal orientations such as {111}<112> and {110}<110> orientations owning high Taylor factor accompanied by geometrical softening phenomenon (Nguyen-Minh et al. 2012, Mehdi et al. 2020, Dillamore et al. 1979, T Haratani et al. 1984, Ushioda et al. 1989). Goss oriented grains were reported to be evolved from the shear bands of {111}<112> oriented single crystal during the recrystallization (Murakami et al. 2012, T Haratani et al. 1984, Ushioda et al. 1989). A few studies have also reported the evolution of Goss orientation from shear bands in the polycrystalline Fe-Si steel (Park et al. 2003, Lee et al. 2018, I Samajdar et al. 1998). However, conclusions are drawn based on the observation of Goss orientation after recrystallization rather than providing any direct evidence of the Goss texture development inside the shear bands. Direct observation of texture evolution inside the shear bands is cumbersome due to high strain accumulation. At the same time, the feasibility of the formation of Goss oriented grains inside the shear bands considering crystal rotation and subsequent geometrical softening has not been explored in detail. Besides, Goss orientation is also said to be unstable under plane strain deformation (Hölscher et al. 1991, Raabe et al. 2002, Mehdi et al. 2019) and the retention of Goss oriented grains during cold rolling stage become highly uncertain irrespective of whether they were found before cold rolling or not. The above arguments significantly raise questions on the origin of Goss texture.

Therefore, complete understanding on the evolution of Goss oriented grains inside the shear bands along with the identification of the primary source of Goss orientation in polycrystalline CRGO steel is an absolute necessity and sets the primary objective of the present study.

Table 6.1: Various experiments done on single crystal and polycrystalline high Fe-Si steel

Authors	Experimental	Findings
(Böttcher et al. 1993)	Cold rolling of polycrystalline Fe-3.16%Si regular grain oriented steel	Goss oriented grains originated due to shear deformation at the surface of the hot rolled plate. The Goss oriented grains retained during cold rolling subsequently were reported to be related to the surface layers of the hot rolled plate.
(Dorner et al. 2007)	Cold rolling of Goss oriented single crystal of Fe-3.24%Si steel	Rotation of Goss orientation towards {111}<112> orientation with the formation of shear bands and microbands. Initial Goss orientation was said to be the origin of Goss orientation inside the microbands.
(Mehdi et al. 2019)	Cold rolling of polycrystalline Fe-2.8%Si non oriented electrical steel	Demonstrated three possible locations of Goss orientation such as shear bands and microbands in {111}<112> oriented grain and the grain boundary between {111}<112> and {113}<361> oriented grains. The initial Goss oriented grains before cold rolling were said to be the source of remaining 1% Goss oriented grains after cold rolling irrespective of their location of existence.
(Giri et al. 2020)	Hot plane strain compression of Fe-3%Si CRGO steel by Gleeble deformation simulator	Particle stimulated nucleation (PSN) of recrystallized grain was reported to be the primary source of Goss orientation.

(T Haratani et al. 1984)	Cold rolling of {111}<112> oriented single crystal of Fe-3%Si steel	Formation of positive and negative slope type shear bands inside {111}<112> single crystals. Goss oriented grains evolving at the early stage of primary recrystallization from inside these shear bands.
(Ushioda et al. 1989)	Cold rolling of {111}<112> oriented single crystal of Fe-3%Si steel	Goss oriented grains developed inside high angle (35°) shear bands during the early stage of primary recrystallization within 10° spread and high orientation spread for Goss oriented grains were found among recrystallized grains of low angle (17°) shear bands.
(I Samajdar et al. 1998)	Cold rolling of polycrystalline Fe-3% Si steel	During early stage of primary recrystallization, Goss oriented grains are reported to be evolved from low angle (20°) shear bands within 5° spread whereas Goss oriented grains originating from high angle (37°) shear bands formed within 20° spread.

6.2 Intermediate Cold rolling

Fig. 6.1(a) shows the through thickness microstructure of 3.78% Si CRGO steel after intermediate cold rolling from surface to center (50% of thickness). Microstructure is found to be composed of single phase ferrite as confirmed by XRD analysis. Deformation due to cold rolling was heterogeneous. The magnitude of deformation was highest at the surface with severe shear deformation whereas it was minimum at the center. As a result, large elongated grains remained undeformed at the center of the cold rolled sheet. In addition to that some other grains have been found to be deformed heavily irrespective of their position along the thickness. EBSD analysis has also been performed through the thickness from surface to center to reveal further details, **Fig. 6.1(b)**. The band contrast maps of the cold rolled sample is shown in **Fig. 6.1(b, c)**. High accumulation of shear strain or overlapping pattern reduces the sharpness of the pattern thus results in low band contrast (Engler et al. 2009, Choi et al. 2004, Wright et al.

2011). The inclined dark colored lines in **Fig. 6.1(b, c)** infer low band contrast which may be due to the presence of shear bands. The coarse grains present in the hot band annealed microstructure, **Fig. 5.4(a, b)**, may have contributed to the development of these shear bands. The high magnification band contrast image, **Fig. 6.1(c)**, clearly shows the presence of two different kinds of shear bands. The first type (Type-I) of shear bands is having high inclination angle (25°) comprised with lower spread (21° to 28°) and larger width. Whereas the other type of shear bands (Type-II) has lower inclination angle (15°) covering wider spread from 3° to 18° and comparatively smaller width. The different kinds of shear bands formed after cold rolling with variation in the inclination angles from the rolling direction were also reported in previous studies (I Samajdar et al. 1998, Ushioda et al. 1989). The Type-I shear bands generally develop on the macroscopic plane (inclined plane from RD) on which maximum shear stress prevails. Further, because of the formation of Type-I shear bands (defects), high shear stress was expected to develop on another inclined plane (macroscopic) in opposite direction, between two parallel Type-I shear bands. This high shear stress on another inclined plane may have contributed towards the formation of Type-II shear bands. However, the same could not be confirmed in the present study.

The ODF construction from the region shown in **Fig. 6.1(b)** has been represented in **Fig. 6.1(d)**. α- (RD||<110>) and γ- (ND||<111>) fiber are the major texture components (Raphanel et al. 1985, Hölscher et al. 1991) found to develop whereas no trace of Goss orientation has been observed after intermediate cold rolling.

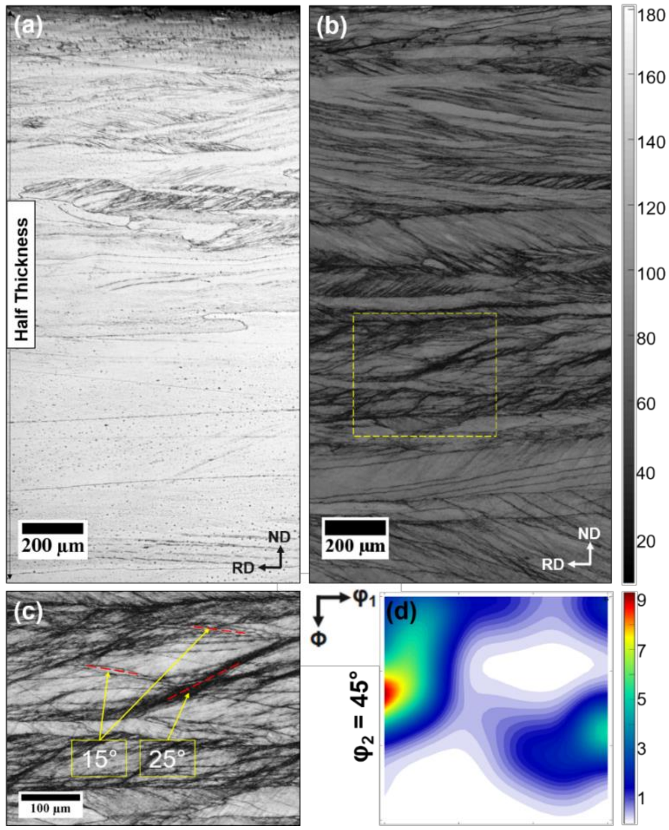

Figure 6.1: (a) Through thickness microstructure from surface to center after 50% cold rolling CRGO steel, (b) EBSD scan showing band contrast map from surface to center after 50% cold rolling infer heterogeneous deformation, (c) EBSD scan showing band contrast map of the rectangular area marked by yellow color in (b) indicate two types of shear bands generated inclined at an angle of 15° and 25° from the rolling direction, (d) ODF with φ_2 = 45° as per Bunge notation after 50% cold rolling CRGO steel showing highly intensified α-fiber texture compared to low intensity of γ-fiber texture

Shear bands are found to develop mostly inside the γ-fiber (ND||<111>) oriented grains. A typical case of shear bands formation inside the {111}<112> oriented ferrite grain is shown by the IPF map in **Fig. 6.2(a)**. The orientation developed inside the Type-II shear bands of {111}<112> oriented grain is clearly rotated cube, $(001)[1\bar{1}0]$ as shown in **Fig. 6.2(a)**. The development of a highly thin region of different orientation at a certain inclination angle as shown in **Fig. 6.2(a)** further validate the development of shear bands. Interestingly, in some of the regions at the intersection of shear bands, the Goss orientation is found to develop, **Fig. 6.2(a)**. But most of the regions inside the Type-I shear bands were unindexed and scans with lower step size of 50-100 nm were performed to reveal the internal details. The magnification has been gradually increased to reveal the orientation developed inside Type-I shear band, as shown by the IPF maps in **Fig. 6.2(b, c, d)**. Mostly, the orientation observed inside the Type-I shear band is $(111)[\bar{1}\bar{1}2]$ which is same as the orientation of the parent grain. The other observed orientation was $(221)[\bar{1}\bar{1}4]$, highlighted in the **Fig. 6.2(c, d)**, which is at 20° deviation from the ideal Goss $(110)[001]$ orientation. The ODFs constructed from the regions of **Fig. 6.2(a)**, **6.2(b)** and **6.2(c)** are also shown in **Fig. 6.2(e)**, **6.2(f)** and **6.2(g)**, respectively. The orientation inside the shear band was found to be rotating towards the Goss orientation from the matrix $(111)[\bar{1}\bar{1}2]$ orientation.

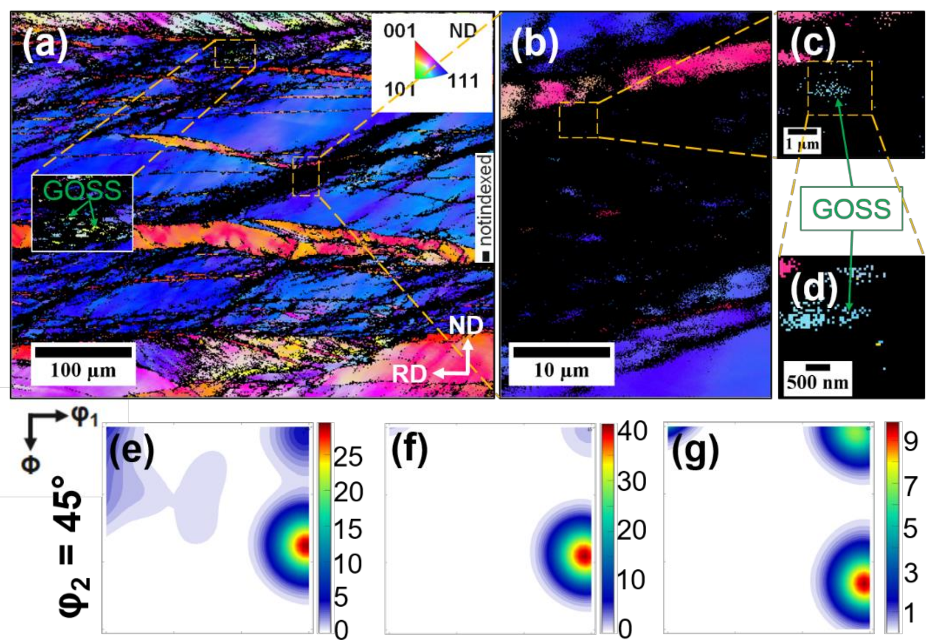

Figure 6.2: (a) ND-IPF map for a shear band region shown in Fig. 6.1(c) within longitudinal ND-RD section of CRGO steel after 50% cold rolling where Type-I and Type-II shear bands formed in {111}<112> orientation, (b) ND-IPF map for the rectangular region marked in (a) at x150 magnification and EBSD scan with 8x8 binning size showing Type-I shear

band region of {111}<112> orientation, (c) ND-IPF map for the rectangular region marked in (b) at x3000 magnification and EBSD scan with 4x4 binning size showing occurrence of $(221)[\bar{1}\bar{1}4]$ orientation which is 20° deviated from the ideal Goss ($(110)[001]$) orientation inside Type-I shear band region of $(111)[\bar{1}\bar{1}2]$ orientation, (d) ND-IPF map for the rectangular region marked in (c) at x3000 magnification and EBSD scan with 2x2 binning size showing increase in fraction of $(221)[\bar{1}\bar{1}4]$ orientation formed inside Type-I shear band region of $(111)[\bar{1}\bar{1}2]$ orientation, (e) ODF with φ_2 = 45° as per Bunge notation generated for the shear band region shown in (a) referring to γ-fiber texture having strong intensity of $(111)[\bar{1}\bar{1}2]$ component, (f) ODF with φ_2 = 45° as per Bunge notation generated for the Type-I shear band region shown in (b) referring to $(111)[\bar{1}\bar{1}2]$ orientation, (g) ODF with φ_2 = 45° as per Bunge notation generated for the region shown in (c) referring to $(111)[\bar{1}\bar{1}2]$ orientation rotating towards Goss ($(110)[001]$) orientation

6.3 Single stage cold rolling

The microstructure developed after single stage cold rolling process is shown in **Fig. 6.3(a)**. The presence of slip lines, as indicated by yellow arrows in **Fig. 6.3(a)** has been observed in some of the regions. The band contrast map, **Fig. 6.3(b, c)** shows the presence of both Type-I and Type-II shear bands. The density and percentage of Type-I shear bands are also found to increase compared to the intermediate cold rolled sample. In addition, the Type-I shear bands become thicker compared to the Type-I shear bands found in the intermediate cold rolled sample. However, the inclination angle of both Type-I and Type-II shear bands remained unchanged on increase in the amount of strain during cold rolling. The ODF constructed from region shown in **Fig. 6.3(b)** is represented in **Fig. 6.3(d)**. The shear bands are found to form at different thickness level but mainly inside the grains with approximately $(112)[3\bar{5}1]$ and $(111)[\bar{1}\bar{1}2]$ orientations. The formation of shear bands inside rotated cube ($(001)[1\bar{1}0]$) component has not been observed in any case.

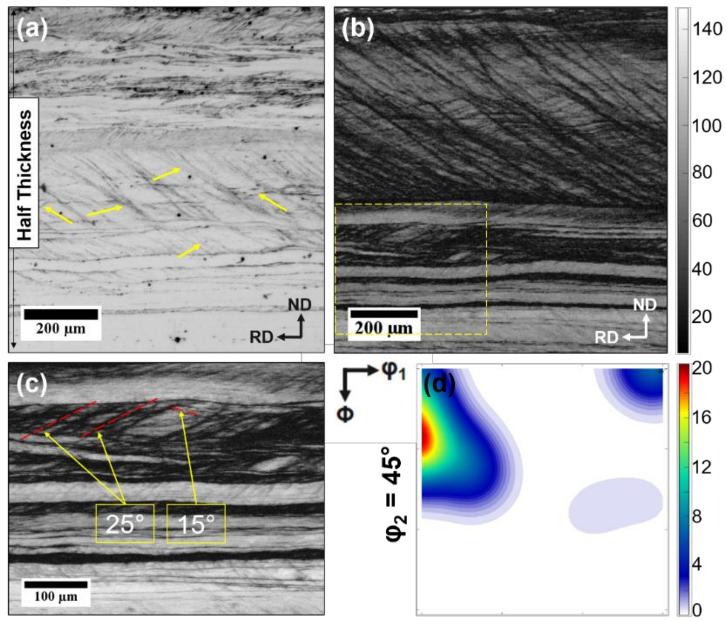

Figure 6.3: (a) Through thickness microstructure from surface to center after cold rolling CRGO steel where slip lines can be visualized marked by yellow arrows, (b) EBSD scan showing band contrast map from surface to center after single stage cold rolling infer severe inhomogeneous deformation, (c) EBSD scan showing band contrast image of the rectangular area marked by yellow color in (b) indicate shear bands generated inclined at an angle of 15° and 25° from the rolling direction, (d) ODF with $\varphi_2 = 45°$ as per Bunge notation after single stage cold rolling of CRGO steel showing highly intensified α-fiber texture compared to highly low intensity of γ-fiber texture

To understand the overall texture development, macrotexture was conducted after single stage cold rolling as shown in **Fig. 5.9(d)**. ODF reveals the presence of three major components, such as {001}<110>, {111}<112> and {111}<110>. The volume fraction of Goss orientation was found to be negligible (<1%) after single stage cold rolling.

An attempt has been made to understand the development of orientation inside the shear bands after single stage cold rolling process. A small band of grain having initial $(111)[\bar{1}\bar{1}2]$ orientation has been chosen in this case as shown by the IPF map in **Fig. 6.4(a)**. But unfortunately, EBSD analysis was not competent to infer clarity about the crystallographic texture developed inside the shear bands since most of the points inside the shear band regions were unindexed. High strain accumulation inside the Type-I shear bands may be the reason behind this. The orientation inside the Type-II shear bands has been identified in a separate high magnification scan having grain with (111)[1$\bar{1}$0] initial orientation, as shown by the IPF map in **Fig. 6.4(b)**. (001)[1$\bar{3}$0] orientation belongs to cube fiber (ND||<001>) texture was found to develop inside the Type-II shear band, **Fig. 6.4(b)**.

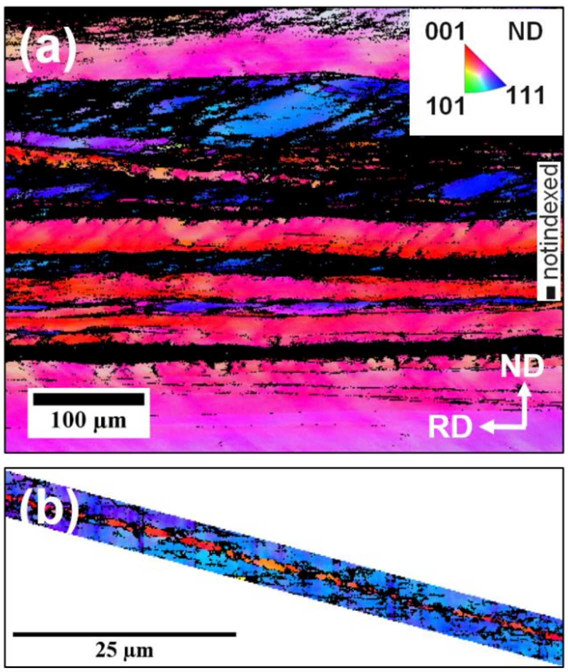

Figure 6.4: (a) ND-IPF map for a shear band region shown in Fig. 6.3(c) within longitudinal ND-RD section of CRGO steel after single stage cold rolling where shear band formation can be seen occurring in (111)[$\bar{1}\bar{1}$2] orientation, (b) ND-IPF map at high magnification showing the presence of thin Type-II shear band region in (111)[1$\bar{1}$0] orientation

6.4 Partial recrystallization of single stage cold rolled plate

IPF map shown in **Fig. 6.5(a)** illustrates partial recrystallization of single stage cold rolled sample at 650° C for 10 min. The shear bands possess high stored energy due to localized deformation and therefore expected to act as a nucleation site for the recrystallization (Hutchinson 1999, Xu et al. 2018, Choi et al. 2004). As expected, new grains started forming from shear band regions. The grains recrystallized inside the shear bands were seen growing in the direction of the bands. As compared to Type-II shear bands, Type-I shear bands were preferred for recrystallization. The low grain orientation spread (GOS) value of the small grains along the shear bands as shown in **Fig. 6.5(b)** again confirms that the grains are recrystallized. The recrystallized grains consist of several orientations with some fraction of Goss oriented grains.

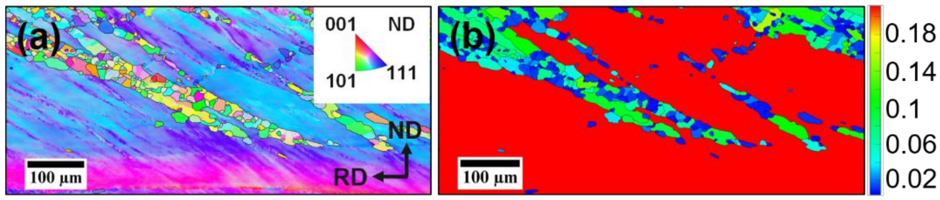

Figure 6.5: (a) ND-IPF map for a smaller region in the longitudinal NR-RD section after partial recrystallization of single stage cold rolled CRGO steel done at 650° C for 10 minutes shown with widely spread grains recrystallizing among Type-I shear bands in the direction of the bands, (b) Grain orientation spread (GOS) map showing large amount of orientation spread within γ-fiber texture representing high strain accumulation from which grains started recrystallizing

The IPF map of the sample partially recrystallized at 650° C for 20 min is shown in **Fig. 6.6(a)**. Some of the Type-II shear bands were remained unrecrystallized as indicated by the black arrows in **Fig. 6.6(a)**. The ODF constructed from that region as shown in **Fig. 6.6(b)** clearly shows the strong presence of Goss orientation. A separate unique color map considering only Goss oriented grains up to 15° spread from the ideal Goss orientation is shown in **Fig. 6.6(c)**. A histogram showing cumulative area percentage of grains vs deviation from the ideal Goss orientation has been represented in **Fig. 6.6(d)**. It appears that around 10% of the area possess less than 15° deviation from the ideal Goss orientation whereas, around 0.5% of the area consist of sharp Goss orientation with less than 5° deviation. Therefore, it is confirmed that the Goss oriented grains originated from the Type-I shear band regions during the recrystallization.

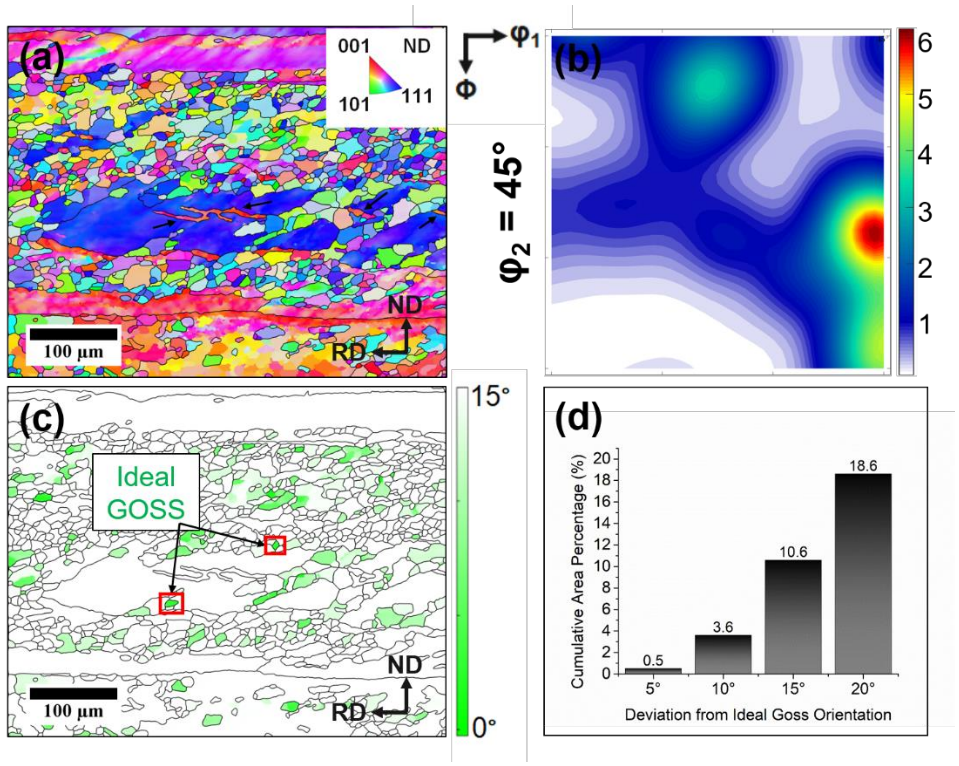

Figure 6.6: ND-IPF map for a shear band region after partial recrystallization of single stage cold rolled CRGO steel done at 650° C for 20 minutes showing some region remained unrecrystallized, (b) ODF at φ_2 = 45° section as per Bunge notation generated from the region shown in (a) indicating strong intensity of {111}<112> orientation along with the presence of Goss ((110)[001]) orientation, (c) Unique color map for the same region shown in (a) considering Goss orientation within 15° spread from the ideal Goss orientation inferring recrystallized Goss oriented grains among the shear band region, (d) Cumulative area fraction vs deviation from the ideal Goss orientation graph showing around 10% of the area appeared in (c) covered by Goss oriented grains which consists only around 0.5% of sharp Goss oriented grains within 5° of deviation

6.5 VPSC model predictions

VPSC model has been utilized for simulation to predict the orientation developed inside the shear band region considering voce hardening parameters shown in **Table 3.5**. The shear bands were found to develop inside the γ-fiber (ND||<111>) textured grains. In this section, the development of different texture components has been explored focusing on {111}<112> initial orientation only.

The mode of deformation inside the shear bands is pure shear on an inclined plane which is oriented at an angle (θ) with respect to rolling direction. And the velocity gradient tensor on reference frame of shear band can be written as follows:

$$L_{SB} = \begin{vmatrix} 0 & 0 & 1 \\ 0 & 0 & 0 \\ 0 & 0 & 0 \end{vmatrix} \tag{6.1}$$

The average inclination angles of the shear bands were found to be 25° and 15° for Type I and Type-II shear bands, respectively. More specifically, the Type -I and Type-II shear bands are in opposite directions and inside {111}<112> oriented grain Type -I and Type-II shear bands are found to be inclined in counter-clockwise and clockwise direction, respectively. Therefore, velocity gradient on sample reference can be obtained by incorporating the inclination angle (θ) in tensor transformation.

For 25° counter-clockwise rotation in Type-I shear band:

$$L_{25} = \begin{vmatrix} 0.38 & 0 & 0.82 \\ 0 & 0 & 0 \\ -0.17 & 0 & -0.38 \end{vmatrix} \tag{6.2}$$

For 15° clockwise rotation in Type-II shear band:

$$L_{15} = \begin{vmatrix} -0.25 & 0 & 0.93 \\ 0 & 0 & 0 \\ -0.06 & 0 & 0.25 \end{vmatrix} \tag{6.3}$$

The {111}<112> orientation was subjected to shear deformation at 25° inclination angle (counter-clockwise) with respect to rolling direction. Orientation developed at different strain level (or thickness reduction) is shown in **Fig. 6.7**. The γ-fiber (ND||<111>) is expected to form at 0.1 applied strain, **Fig. 6.7(b)**. On further increment of applied strain to 2.1, two other intermediate orientations, such as $(221)[1\bar{1}0]$ and near Goss

((221)[$\bar{1}\bar{1}$4]) were expected to develop, **Fig. 6.7(e)**. And finally, the Goss orientation developed along with the Rotated Goss component when the true strain becomes equal to 2.2 as shown in **Fig. 6.7(g)**. But on further increment of strain the Goss orientation was found to rotate again, **Fig. 6.7(h, i)**. The inclination angle (θ) of the shear band has been varied and possibility of the development of Goss orientation has been explored. It has been found that for any value of inclination angle from 15° to 25°, Goss orientation may develop. But the required strain increases with the inclination angle as shown in **Fig. 6.8**. The strain requirement for the development of Goss orientation at 25° inclination angle was predicted to be high around 2.2.

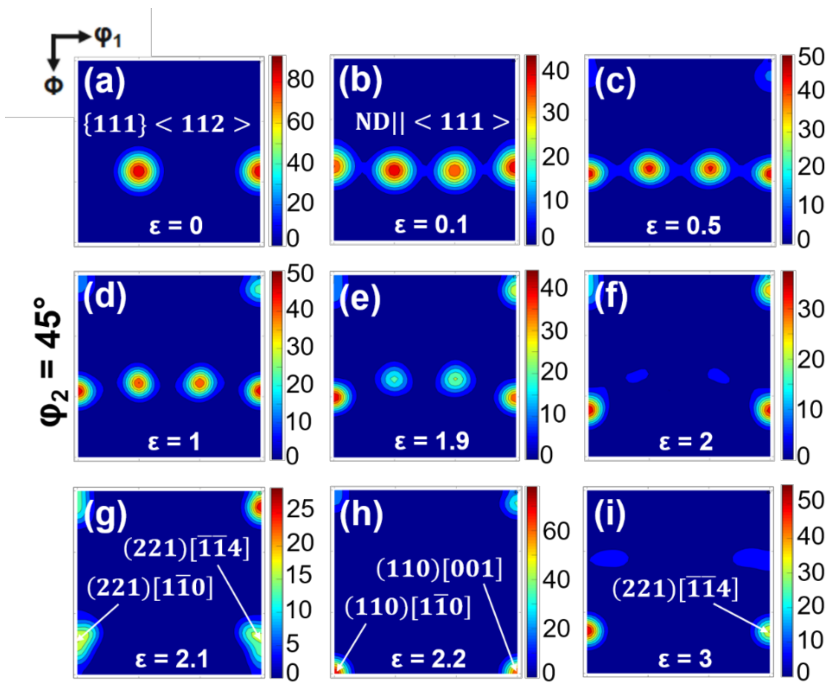

Figure 6.7: (a, b, c, d, e, f, g, h, i) ODF results with $\varphi_2 = 45°$ as per Bunge notation generated by VPSC simulation done starting with {111}<112> orientation (ε = 0) subjected to shear deformation at angle of 25° counterclockwise from rolling direction at strain (ε) (a) 0 (b) 0.1 (c) 0.5 (d) 1 (e) 1.9 (f) 2 (g) 2.1 (h) 2.2 (i) 3 showing a possibility of lattice rotation taking place inside shear band towards Goss ((110)[001]) orientation achieved at ε = 2.2

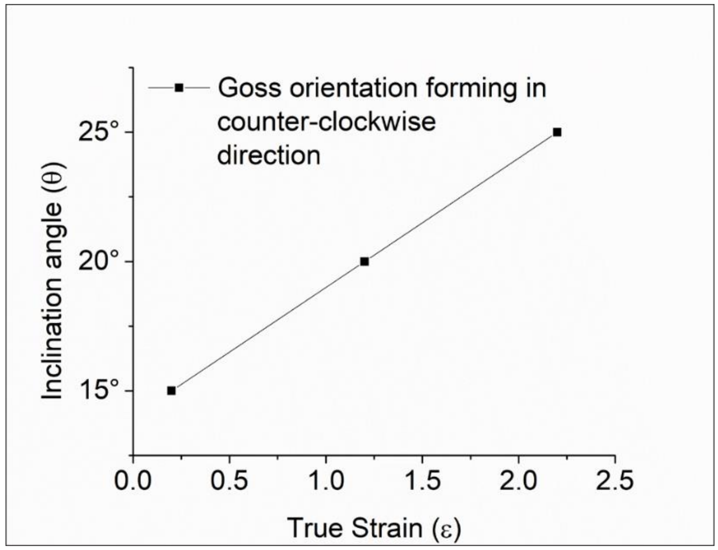

Figure 6.8: Plot showing the variation in required true stain (ε) in thickness direction for the development of Goss orientation for different inclination angle (θ) counterclockwise from rolling direction

Orientation developed at different strain level (thickness reduction) for {111}<112> initial orientation and 15° inclination angle (clockwise) is shown in **Fig. 6.9**. Rotated cube component is expected to be developed at 2.1 strain, **Fig. 6.9(g)**. But on increment of strain, the rotated cube component further reoriented itself towards other orientations belonging to α-fiber (RD||<110>) texture, **Fig. 6.9(h, i)**. The true strain requirement for the formation of rotated cube orientation also increases with inclination angle (θ) as shown in **Fig. 6.10**. It has been found that rotated cube orientation may develop for an inclination angle as low as 5° (clockwise) **Fig. 6.10**. And the corresponding strain requirement is also low, around 0.7, **Fig. 6.10**.

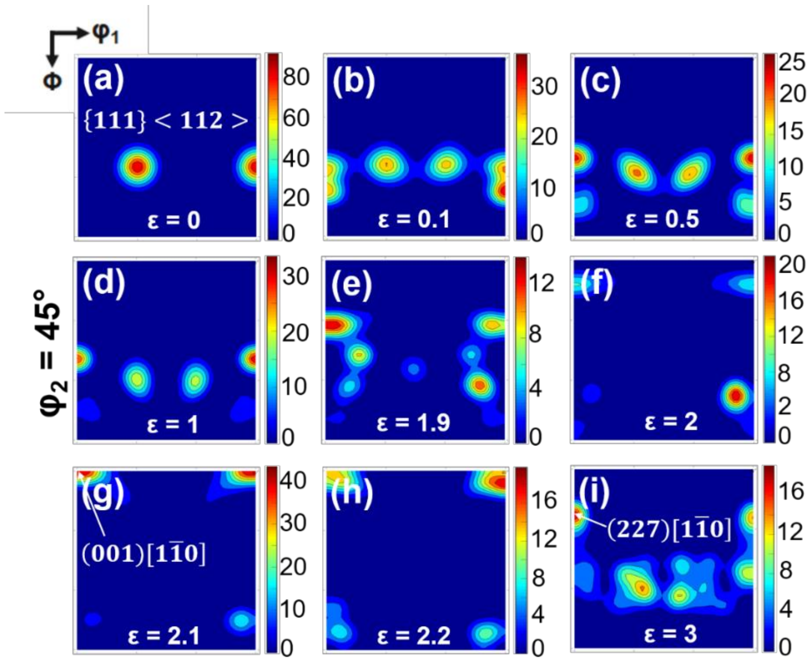

Figure 6.9: (a, b, c, d, e, f, g, h, i) ODF results with $\varphi_2 = 45°$ as per Bunge notation generated by VPSC simulation done starting with {111}<112> orientation (ε = 0) subjected to shear deformation at angle of 15° clockwise from rolling direction at strain (ε) (a) 0 (b) 0.1 (c) 0.5 (d) 1 (e) 1.9 (f) 2 (g) 2.1 (h) 2.2 (i) 3 showing a possibility of lattice rotation taking place inside shear band towards rotated cube orientation achieved at ε = 2.1

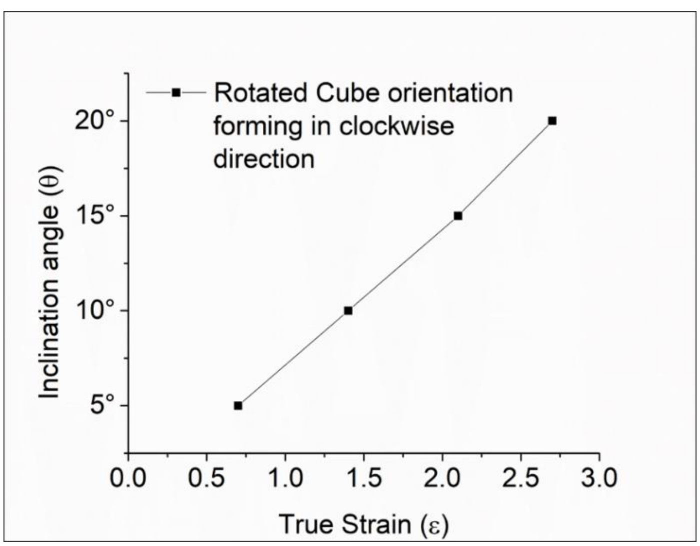

Figure 6.10: Plot showing the variation in required true stain (ε) in thickness direction for the development of rotated cube orientation for different inclination angle (θ) clockwise from rolling direction

Therefore, VPSC modelling also predicts that of Goss and rotated cube orientation may form inside the Type-I and Type-II shear band respectively in $(111)[\bar{1}\bar{1}2]$ oriented grain.

6.6 Discussion

The ODF of the single stage cold rolled sample, as shown in **Fig. 5.9(d)** reveals that both the components {111}<112> and {111}<110> of γ-fiber texture evolved during cold rolling along with strong rotated cube ({001}<110>) orientation. The intensity of Goss ((110)[001]) orientation was found to be insignificant or negligible. The shear bands developed preferentially inside the γ-fiber textured components such as {111}<112> and {111}<110>. But shear bands were never found to form inside the rotated cube ({001}<110>) oriented grains.

Consideration of Taylor factor provide further insight on the preference of orientation for shear band formation and associated geometrical softening process. The Taylor factor signify the increment in total shear strain which develops on different slip systems for unit increment of imposed equivalent strain (Piehler 2009). In the present study, Taylor factor for different possible crystal orientation under plane strain compression and pure shear deformation mode has been calculated considering Bishop Hill stress and maximum work principle (Piehler 2009) and represented in **Fig. 6.11(a, b)**.

The formation of shear bands is attributed to the high Taylor factor of γ-fiber components under plane strain compression (Samajdar et al. 1997, Nguyen-Minh et al. 2012, Mehdi et al. 2020) as shown in **Fig. 6.11(a)**. High Taylor factor contributes to higher slip activity and thus high dislocation density (Rajmohan 1997). The strain hardening in γ-fiber textured grains due to high deformation, restricts its further homogeneous deformation. Therefore, the localized deformation or instability in the form of shear bands is preferred inside the γ-fiber textured components.

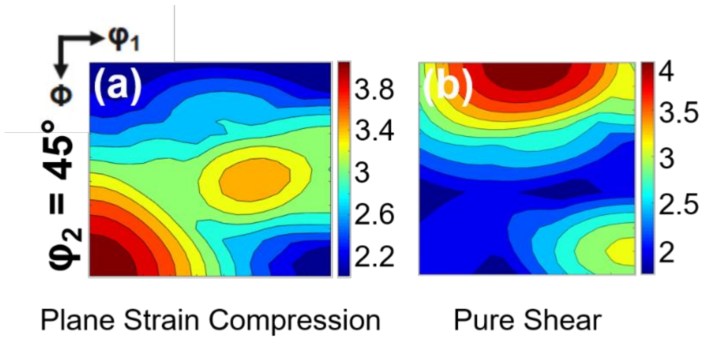

Figure 6.11: Calculated Taylor Factor maps with respect to ODF with φ_2 = 45° as per Bunge notation generated under (a) plane strain compression, (b) pure shear

Experimentally, the near Goss orientation is found to develop inside the Type-I shear bands in {111}<112> oriented grain of partially cold rolled sample whereas the orientation inside the Type-I shear bands could not be detected in fully cold rolled sample. Development of cube fiber (ND||<001>) has been confirmed inside Type-II shear bands in both the samples.

For further understanding, the shear band texture was simulated using VPSC model considering {111}<112> initial orientation, **Fig. 6.7** and **6.9**. In case of 25° inclination angle, the initial {111}<112> orientation rotates toward Goss orientation up to 2.2 true strain. Whereas for 15° inclination angle crystal rotates toward the rotated cube orientation up to 2.1 true strain. The intermediate orientations originated during the crystal rotation inside the shear band can also be seen in the **Fig. 6.7(a-h)** and **6.9(a-g)**. Most of the intermediate orientations originated during the crystal rotation possess lower Taylor factor and expected to contribute to the geometrical softening (T Haratani et al. 1984, Ushioda et al. 1989). Therefore, it further promotes the plastic instability due to shear band formation.

The main limitation of the VPSC simulation done in the present study was the consideration of pure shear deformation which holds good until the condition of instability inside the shear band prevails. When the crystal rotation inside the shear band no longer contribute to geometrical softening, the condition for instability violates and the region inside the shear band will not be deformed anymore under simple shear (Nguyen-Minh et al. 2012). Therefore, the predicted intermediate orientations may not develop inside the shear band if they don't contribute to geometrical softening. Although the Goss and rotated cube component developed at certain strain level, they are predicted not to be remained stable on further increment of strain. In case of the 15° inclination angle, VPSC simulation predicts that the rotated cube orientation will reorient to $(227)[1\bar{1}0]$ component, **Fig. 6.9(i)** on further deformation above 2.1 true strain which is unlikely to happen since deformation condition will not remain pure shear then. Similarly, against the VPSC prediction as shown in **Fig. 6.7(i)**, Goss orientation will not reorient further to $(221)[\bar{1}\bar{1}4]$ component since that would have contributed to the geometrical hardening rather than geometrical softening.

In the same way, the orientations, which are not contributing to the geometrical softening, such as Rotated Goss as predicted in case of 25° inclination angle (**Fig. 6.7(h)**), is unlikely to develop. In line with the above argument no Rotated Goss orientation has been observed inside the Type-I shear bands experimentally. And indirect consequence is the lower accumulation of shear strain inside the Type-II shear band where geometrical softening ceased after 0.7-2.1 (5° to 15° inclination angle) strain as compared to Type-I shear band where geometrical softening continues up to 1.2-2.2 (20° to 25° inclination angle) true strain.

On partial recrystallization of fully cold rolled sample, Goss grains are found to develop from the Type-I shear bands in {111}<112> oriented grain, **Fig. 6.6**. The only possible mechanism for the formation of these Goss oriented grains is the crystal rotation inside the shear bands.

Goss oriented grains were present after hot band annealing and has been indicated by arrows in **Fig. 5.4(b, c)**. However, in the present study it has been shown that Goss orientation originates inside the Type-I shear bands in γ-fiber oriented grains. A similar observation was earlier reported in (111)[$\bar{1}\bar{1}$2] oriented single crystal study by Haratani et al. (T Haratani et al. 1984) and Ushioda et al. (Ushioda et al. 1989). From another perspective, the Goss orientation developed inside the shear bands during the cold rolling may not be stable under plane strain compression (Mehdi et al. 2019, Hölscher et al. 1991, Raabe et al. 2002). Therefore, there is a high probability that the Goss orientation will again transform into γ-fiber due to rotation under plane strain compression, as shown in **Fig. 6.12**. But Goss orientation may again develop inside the shear bands in the γ-fiber textured grain. These two contradicting processes may continue to operate in cycle during the cold rolling process. And as a consequence, there would be always some amount of Goss texture retained in the cold rolled sample. As per the presented hypothesis, the volume fraction of Goss oriented grains is not expected to increase with the shear band formation in the cold rolling process because the two contradicting processes are operating simultaneously. In line with the prediction, the intensity of Goss oriented grains was found to be negligible after cold rolling. But sufficient amount of Goss oriented grains developed during the partial recrystallization.

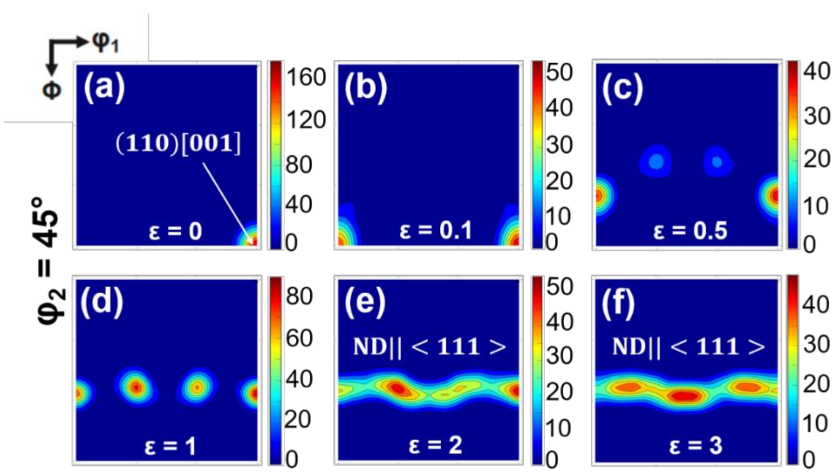

Figure 6.12: (a, b, c, d, e, f) ODF results with $\varphi_2 = 45°$ as per Bunge notation generated by VPSC simulation done starting with Goss ((110)[001]) orientation (ε = 0) subjected to plane strain compression at strain (ε) (a) 0

(b) 0.1 (c) 0.5 (d) 1 (e) 2 (f) 3 showing instability of Goss orientation under plane strain compression

On the other hand, the operating deformation mode is pure shear close to the surface. Goss/near Goss orientation have high Taylor factor under pure shear loading, as shown in **Fig. 6.11(b)**. Therefore, it is expected to exhibit higher resistance for homogeneous shear deformation. Consequently, Goss orientation developed inside the shear bands is expected to be retained at the rolled plate surface.

The present work is in the opinion that the Goss orientation developed inside the shear bands are the primary origin of Goss orientation in CRGO steel.

6.7 Conclusions

The following conclusions can be derived from the present work:

(a) Shear bands preferentially formed inside the grains having γ-fiber orientation during the cold rolling operation in polycrystalline CRGO steel.

(b) High magnification EBSD analysis inside the Type-I shear band of $(111)[\bar{1}\bar{1}2]$ oriented grain provides direct evidence of the development of near Goss ($(221)[\bar{1}\bar{1}4]$) orientation.

(c) Cube fiber (ND||<001>) orientation is found to develop inside the Type-II shear band in γ-fiber (ND||<111>) textured grain.

(d) In line with the experimental results, Crystal plasticity based simulation also predicts that the Goss orientation may develop due to pure shear deformation on a plane having 15°-25° inclination angle inside the $(111)[\bar{1}\bar{1}2]$ oriented grain.

CHAPTER 7

Role of silicon concentration on the feasibility of cracking and Goss texture development in cold rolled grain oriented steel

7.1 Introduction

In general, silicon contributes to the solid solution strengthening in iron. At the same time, it reduces the fracture stress and increases the ductile to brittle transition temperature (Gerberich et al. 1981). In a study, it has been reported that in the as-cast samples of Fe-Si steels, the steel having higher amount of silicon possesses higher yield strength which further increases during deformation (Ros-Yanez et al. 2007). Witting et al. (Wittig et al. 2008) also showed that the increase in silicon content from 4.5 to 6.4 wt.% increases hardness by 40% and yield stress by 23.33%.

In ferritic steels, varying the amount of alloying elements in iron can give rise to the combination of slip systems which becomes active during deformation. It was observed in a study that different slip systems were active in the varieties of steels having different chemical compositions (Takenaka et al. 2018b). In general, silicon contributes to the solid solution strengthening in iron. In a single crystal study, it has been reported that temperature independent part of CRSS increases due to increase in silicon concentration in Fe-Si steel (Novák et al. 1976). The role of crystallographic slip becomes crucial as different slip activities can induce significant changes in the development of crystallographic texture during cold rolling (Houbaert et al. 2007). Few studies have reported that higher silicon content can give rise to favorable recrystallization texture in Fe-Si steels (Kestens et al. 1996, C.-K. Hou 1996). However, the development of various crystallographic orientations due to varying silicon content in Fe-Si steel during deformation is not studied in detail.

Moreover, the understanding of Goss texture development in CRGO steel is not clear. Goss orientation is generally unstable under plane strain deformation (Hölscher et al. 1991, Raabe et al. 2002). Many researchers showed that the development of Goss oriented grains were related to shear band formation during cold rolling which develops on subsequent primary recrystallization stage (T Haratani et al. 1984, Ushioda et al. 1989, I Samajdar et al. 1998). Recently, a clear evidence has been provided on the formation of Goss oriented grains inside the shear bands of {111}<112> component of γ-fiber texture during cold rolling (Jain, Modak, et al. 2022). It was demonstrated that the development of Goss orientation was achieved due to crystal rotation inside shear bands which was associated with the geometrical softening phenomenon. However, increasing the amount of silicon content in CRGO steel can increase the strain hardening during cold rolling, which can lead to change in the shear band formation, and thus may affect the development of Goss orientation.

The present study demonstrates the effect of silicon concentration on the feasibility of cracking during cold rolling in Fe-Si steel by incorporating stress-based analysis using finite element method. The microstructure and texture development during hot and cold rolling in three different Fe-Si steels with varying silicon content is also compared. Crystal plasticity based analysis was incorporated to understand the development of crystallographic texture during cold rolling by considering different hardening parameters of two primary ({110}<111>) and secondary ({112}<111>) slip systems in BCC-ferrite. The predictions were correlated with the experimental observations in three kinds of Fe-Si steels. Furthermore, the study also focuses on the effect of varying silicon content on the development of Goss orientation in CRGO steel.

7.2. Finite element method simulation

To understand the role of Si addition on the possibility of crack formation, Finite Element Method (FEM) based stress analysis has been carried out with different material models. The flow curves of three alloys have been estimated based on the measured hardness. Initially the yield strength (YS) and ultimate tensile strength (UTS) of the alloys was predicted by employing the following empirical relationships (equations (4) and (5), respectively) (Hsu 1986, Pavlina et al. 2008):

$$\text{UTS} = \left(\frac{H}{2.9}\right)\left(\frac{n}{0.217}\right)^{n} \tag{7.1}$$

$$\text{YS} = \left(\frac{H}{3}\right)(0.1)^{n} \tag{7.2}$$

Further, the complete flow curve (stress vs strain) was estimated assuming 210 GPa Young's modulus, 0.3 Poisson's ratio, and 0.2 strain hardening exponent. It was also assumed that all the alloys will comply with the following empirical relationship (equation (6)) proposed by Hollomon et al. (Hertzberg et al. 1985):

$$\sigma = K(\varepsilon)^{n} \tag{7.3}$$

Finally, different flow stress curves derived from the hardness of HSI, MSI and LSI steels were incorporated as different material models to predict the analytical stress expected to develop during cold rolling process. The FEM model with the same boundary conditions as described in Chapter 4 was employed to simulate the rolling process using ABAQUS. Thereby, **Fig. 7.1** shows the simulated roll force vs time graphs which represent the rolling loads required for 20% thickness reduction of HSI, MSI and LSI steels. The steady-state zone during rolling simulation was between 5 s to 12 s in which the steels were completely under the rollers. The maximum rolling load for all three steels appeared at 5.8 s in the steady-state zone. It was observed that the maximum rolling load increases from 1.1 x 10^6 N to 1.3 x 10^6 N on increasing the Si content from 2.98 wt.% to 3.78 wt.%. In chapter 4, it was demonstrated that high tensile stresses during cold rolling of Fe-Si steel having high silicon content (3.78 wt.%) leads to the formation of edge crack and alligator crack (Jain, Patra, et al. 2022). Similarly, the tensile stress expected to develop during different stages of cold rolling process of HSI, MSI and LSI steels has been demonstrated in **Figs. 7.2** and **7.3**. A tensile stress along y(ND)-direction (S22) which promote alligator crack was expected to develop at the mid-thickness during the initial stage (2.5 s) in all the cases. The magnitude of this tensile stress was highest (70.7 MPa) in case of HSI and smallest (61.8 MPa) in case of LSI. The increase in hardness (15%) and the increase in maximum tensile stress (14.5%) were almost similar for increasing Si concentration from 2.98 wt.% to 3.78 wt.%. On the other hand, the tensile stress along x(RD)-direction (S11) which promote edge crack was maximum at end-width during the steady-state zone (5.8 s). The similar 15% change in magnitude has been observed for increase in Si content from 2.98 wt.% to 3.78 wt.%.

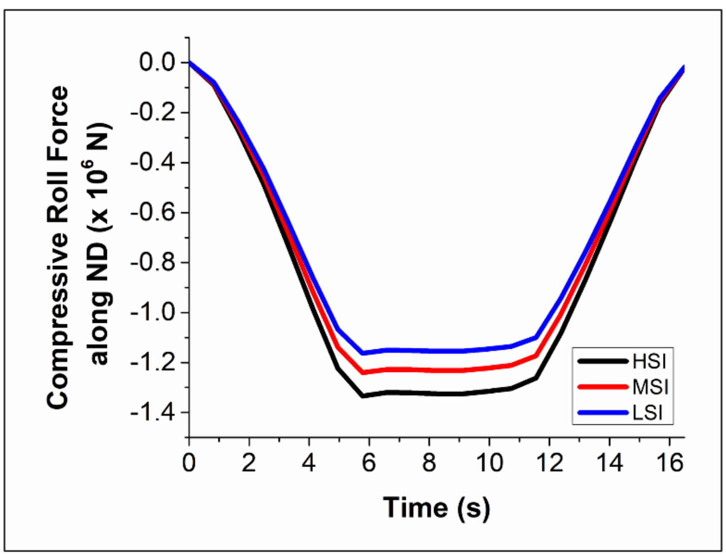

Figure 7.1: Simulated roll force vs time graph for HSI, MSI and LSI Fe-Si steels by using FEM based analysis

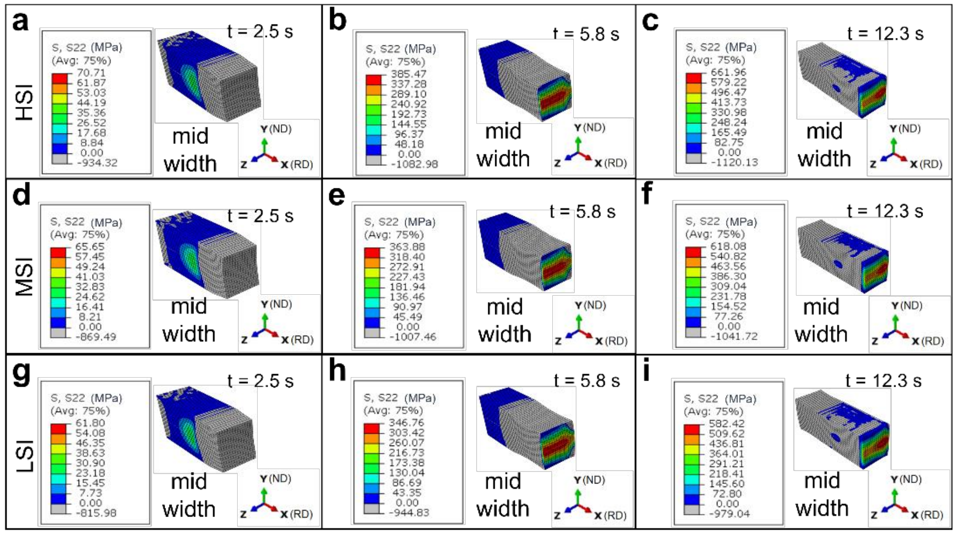

Figure 7.2: Stress distribution along y(ND)-direction (S22) along mid-width after rolling simulation of HSI steel at (a) entry stage (2.5 s), (b) maximum Roll force in the steady-state zone (5.8 s) and (c) exit stage (12.3 s), after rolling simulation of MSI steel at (d) entry stage (2.5 s), (e) maximum Roll force in the steady-state zone (5.8 s) and (f) exit stage (12.3 s), and after rolling simulation of LSI steel at (g) entry stage (2.5 s), (h) maximum Roll force in the steady-state zone (5.8 s) and (i) exit stage (12.3 s)

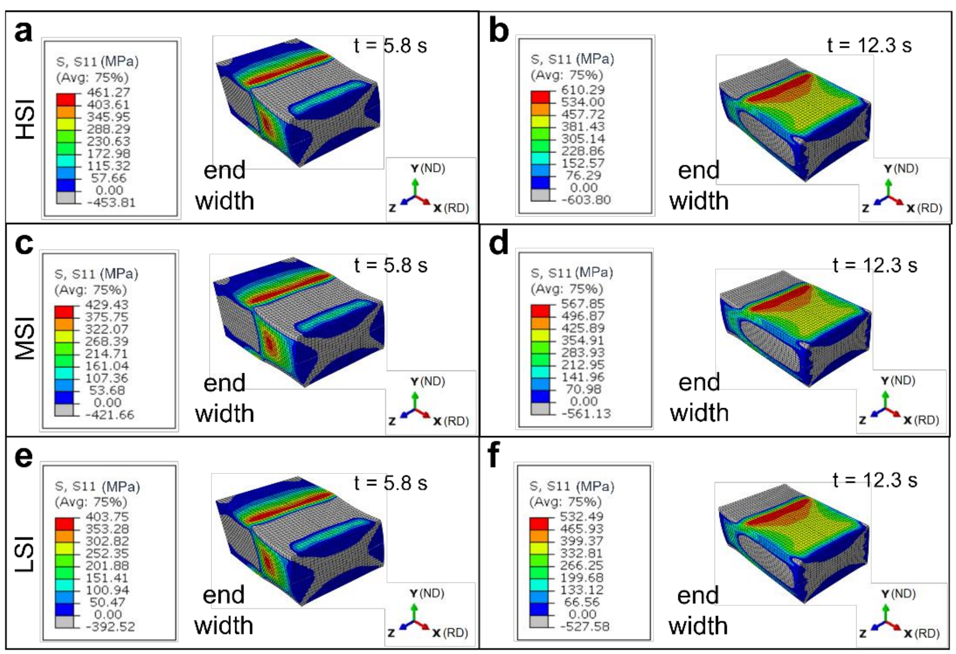

Figure 7.3: Stress distribution along x(RD)-direction (S11) along end-width after rolling simulation of HSI steel at (a) maximum Roll force in the

steady-state zone (5.8 s) and (b) exit stage (12.3 s), after rolling simulation of MSI steel at (a) maximum Roll force in the steady-state zone (5.8 s) and (b) exit stage (12.3 s), and after rolling simulation of LSI steel at (a) maximum Roll force in the steady-state zone (5.8 s) and (b) exit stage (12.3 s)

7.3 Hot rolling and hot band annealing

The microstructures of HSI, MSI and LSI steels after HR are shown in **Fig. 7.4(a-c)**, respectively. Large deformed grains elongated along RD were formed during HR in all three Fe-Si steels. Some small recrystallized grains were also developed along the boundaries of the large columnar grains which are indicated by white arrows in **Fig. 7.4(a-c)**. Most probably, these small recrystallized grains in the hot rolled structure were the product of dynamic recrystallization. ND-Inverse Pole Figure (IPF) maps of HSI, MSI and LSI steels after HR and HBA are shown in **Fig. 7.4(d-i)**. Large deformed bands in the hot rolled structure were observed throughout the cross section in all three Fe-Si steels, **Fig. 7.4(d, f, h)**. After HBA, the recrystallized grains mostly appeared near the surface layers and/or along the grain boundaries of large deformed bands, **Fig. 7.4(e, g, i)**. However, large columnar grains remained unrecrystallized in all the cases. The microstructure and crystallographic texture developed during HR and subsequent HBA were almost identical in all Fe-Si steels.

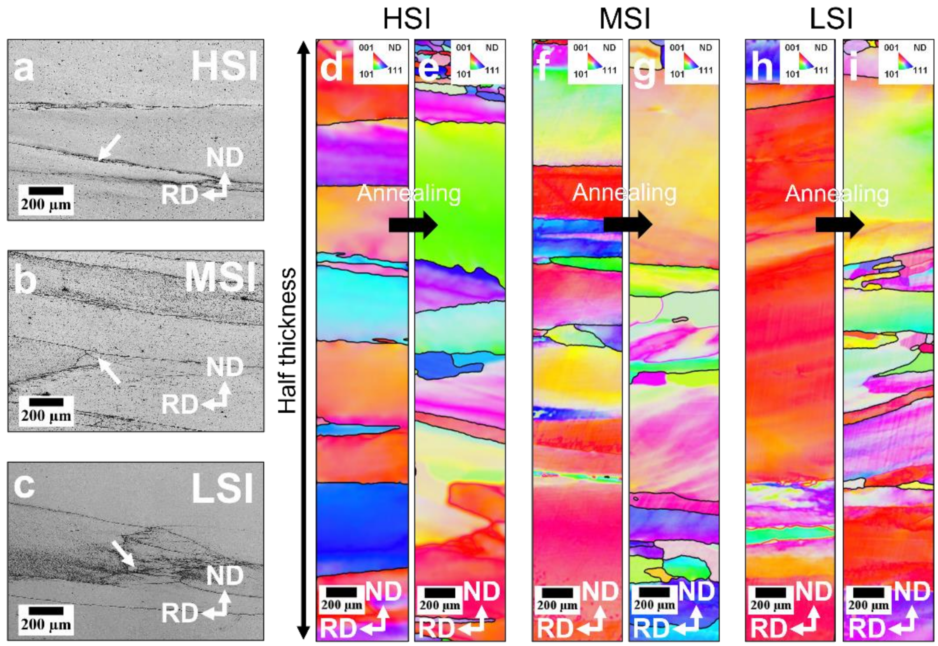

Figure 7.4: Microstructures showing large deformed bands and small recrystallized grains along the boundaries formed during hot rolling of (a) HSI, (b) MSI, (c) LSI, and ND-IPF maps along ND-RD longitudinal section from surface to center after hot rolling and hot band annealing of (d, e) HSI, (f, g) MSI, and (h, i) LSI, respectively

7.4 Microtexture analysis after different stages of cold rolling

7.4.1 Intermediate cold rolling

Band contrast maps from surface to center along ND-RD section of the ICR samples are shown in **Fig. 7.5(a-c)**. The dark colored regions having low band contrast value represent the regions of heavy deformation. MSI sample was less deformed as compared to HSI and LSI samples, **Fig. 7.5(a-c)**. However, inhomogeneous deformation in the form of shear bands was observed in all three Fe-Si steels. Dark colored lines inclined from RD indicates the shear bands, **Fig. 7.5(a-c)**. The shear bands formed during ICR were relatively thicker and widely spread in HSI compared to those formed in MSI and LSI. On the other hand, the fraction of low band contrast regions in LSI was higher compared to that in MSI and HSI steels. The fraction of low band contrast regions in LSI may have been higher due to the higher extent of grain fragmentation. ND-IPF maps of the ICR samples of HSI, MSI and LSI steels are shown in **Fig. 7.5(d-f)**, respectively. Orientation distribution Function (ODF) maps were also constructed for regions shown in **Fig. 7.5(d-f)** which are exhibited in **Fig. 7.5(g-i)**. Mostly, α, γ and θ-fiber texture components were developed in HSI having highest intensity of {112}<110> crystallographic orientation. In MSI, most of the deformed grains have either rotated cube or close to {112}<131> orientations. On the other hand, high intensity of {112}<110> component of α-fiber texture was observed in LSI. Weak intensity of Goss orientation was also found to remain in MSI and LSI steels after ICR which are indicated by white arrows in **Fig. 7.5(e, f)**. The shear bands in HSI were mostly developed inside {111}<112> component of γ-fiber crystallographic texture as highlighted with dotted white rectangular block in **Fig. 7.5(d)**. Whereas in MSI and LSI, the shear bands were found to develop inside grains having either {112}<131> or {112}<110> orientations which are shown by dotted white rectangular blocks in **Fig. 7.5(e)** and **Fig. 7.5(f)**, respectively.

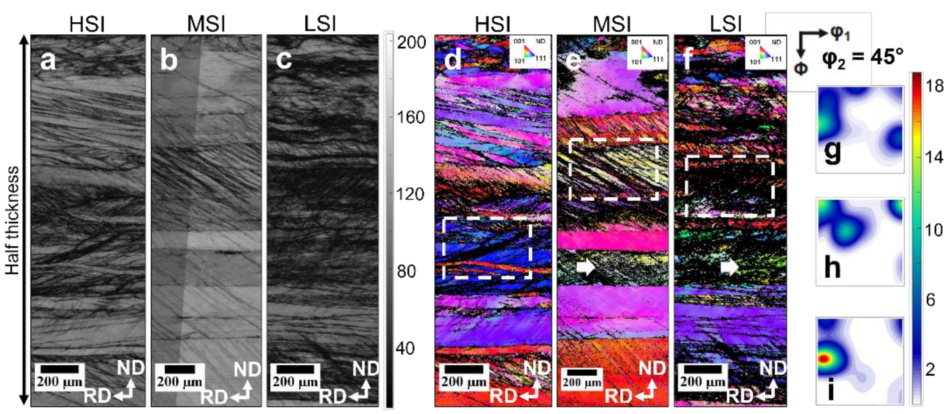

Figure 7.5: Band contrast maps along ND-RD longitudinal section from surface to center after intermediate cold rolling of (a) HSI, (b) MSI, (c) LSI, ND-IPF maps of the intermediate cold rolled samples of (d) HSI, (e) MSI, (f) LSI, and (g, h, i) $\varphi_2 = 45°$ ODF maps (as per Bunge notation) of regions shown in (d, e, f), respectively

7.4.2 Single stage cold rolling

Band contrast maps of the SCR samples of HSI, MSI and LSI, are shown in **Fig. 7.6(a-c)**. Heterogeneity in the form of shear bands was prominent in the cold rolled structure of all three alloys and the extent of shear band formation was almost similar in HSI, MSI and LSI after increasing the amount of thickness reduction during SCR. ND-IPF maps of HSI, MSI and LSI steels after SCR are shown in **Fig. 7.6(d-f)**, respectively. ODF maps were generated for the regions shown in **Fig. 7.6(d-f)** which are shown in **Fig. 7.6(g-i)**. Mostly, components of α, γ, and θ-fiber crystallographic textures were developed after SCR. Noticeably, in all three alloys, θ-fiber textured grains were found to be almost undeformed, and no shear bands were observed inside those grains.

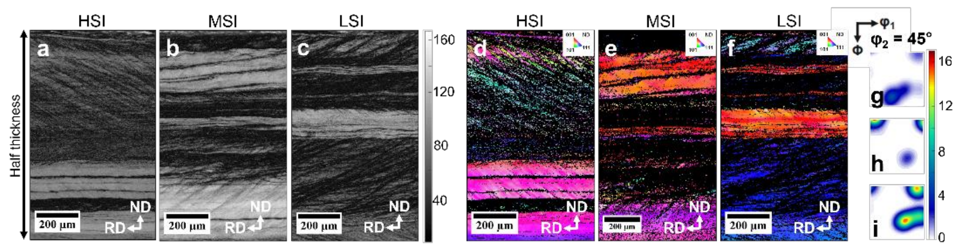

Figure 7.6: Band contrast maps from surface to center along ND-RD longitudinal section after single stage cold rolling of (a) HSI, (b) MSI, (c) LSI, ND-IPF maps of the single stage cold rolled samples of (d) HSI, (e) MSI, (f) LSI, and (g, h, i) φ_2 = 45° ODF maps (as per Bunge notation) for regions shown in (a, b, c), respectively

7.5 Macrotexture analysis after intermediate and single stage cold rolling

To represent the overall crystallographic texture covering larger sample volume, macrotexture analysis was performed after different stages of cold rolling (ICR and SCR) on RD-TD plane at 1/4th thickness. The ODFs (φ_2=45° cross section) of HSI, MSI, and LSI steels after ICR and SCR are shown in **Fig. 7.7(a-c)** and **Fig. 7.7(d-f)**, respectively. The volume % of different crystallographic orientations such as, Goss, rotated cube ({001}<110>), {111}<112>, and {111}<110>, was also estimated from the corresponding ODF considering 15° threshold as given in **Table 7.1**. In HSI, the volume fraction of rotated cube orientation was significantly higher after ICR (4%) and SCR (7.6%) compared to that formed in MSI and

LSI (<3%). Although, the volume % of {111}<110> orientation of γ-fiber texture component was higher in HSI and MSI after SCR, it was also significantly developed in LSI steel. Moreover, a considerable amount (>8%) of {111}<112> component was present in all the steels after both ICR and SCR. Most interestingly, the volume % of Goss orientation was lower than 2% after ICR which further reduced to less than 1% after SCR in all three Fe-Si steels. Nevertheless, the volume fraction of Goss orientation was estimated to be higher in LSI (0.9%) compared to that in MSI (0.1%) and HSI (0.3%) after SCR. Such small variation (0.1-0.9%) may have occurred due to the experimental uncertainties.

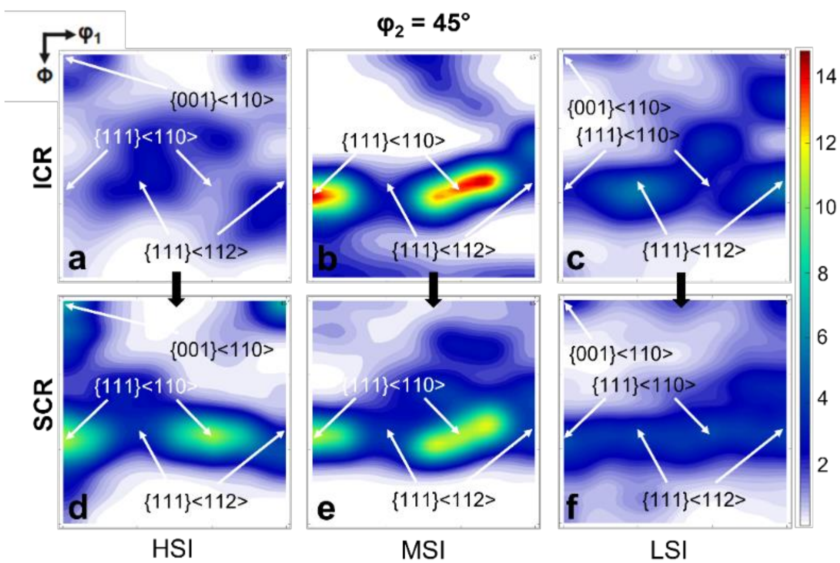

Figure 7.7: φ_2 = 45° ODF maps (as per Bunge notation) showing macrotexture analysis conducted after intermediate cold rolling of (a) HSI, (b) MSI, and (c) LSI, and after single stage cold rolling of (d) HSI, (e) MSI, and (f) LSI

Table 7.1: Volume % of various orientations based on macrotexture analysis shown in Fig. 7.7(a-f) in HSI, MSI and LSI samples after different stages of cold rolling

Sample	**Cold Rolling stage**	**{110}<001> (Goss)**	**{111}<112>**	**{111}<110>**	**{001}<110>**
HSI	ICR	0.7	8.0	5.2	4.0
	SCR	0.3	12.3	21.7	7.6

MSI	ICR	1.5	13.2	22.4	0.6
	SCR	0.1	13.5	23.5	2.3
LSI	ICR	0.3	12.5	9.3	2.9
	SCR	0.9	11.0	11.9	3.0

7.6 Microhardness

The microhardness testing was conducted along ND-RD longitudinal section after HR, HBA, ICR and SCR of three Fe-Si steels. Hardness was measured on at least 10 points through the thickness and the average values are shown in **Fig. 7.8**. The hardness of the hot rolled samples decreased from 223.2 HV to 201.0 HV due to reduction in the silicon content. Interestingly, the hardness was found to increase after HBA in all the alloys containing different amount of Si. Such hardness increment may be attributed to the reduction in grain size, **Fig. 7.4(e, g, i)**. The larger grains resulted in lower hardness in the hot rolled samples as compared to the hot band annealed samples. As expected, the hardness was found to increase with increase in the cold rolling reduction. In case of LSI, hardness increased from 203 HV to 297.5 HV after ICR. On further increasing the cold rolling reduction, the hardness increased up to 342.5 HV after SCR in LSI steel. A similar trend has been observed in all the alloys. ICR sample showed higher hardness in LSI steel compared to MSI which could be due to the lower cold rolling strain in MSI (ε = 0.5) compared to that of LSI steel (ε = 0.94). The microstructure after ICR also appeared less deformed in MSI steel as compared to HSI and LSI steels, **Fig. 7.5(a-c)**. After completing cold rolling (SCR), the hardness of HSI, MSI and LSI increased to 349.9, 339.9 and 342.5 HV, respectively.

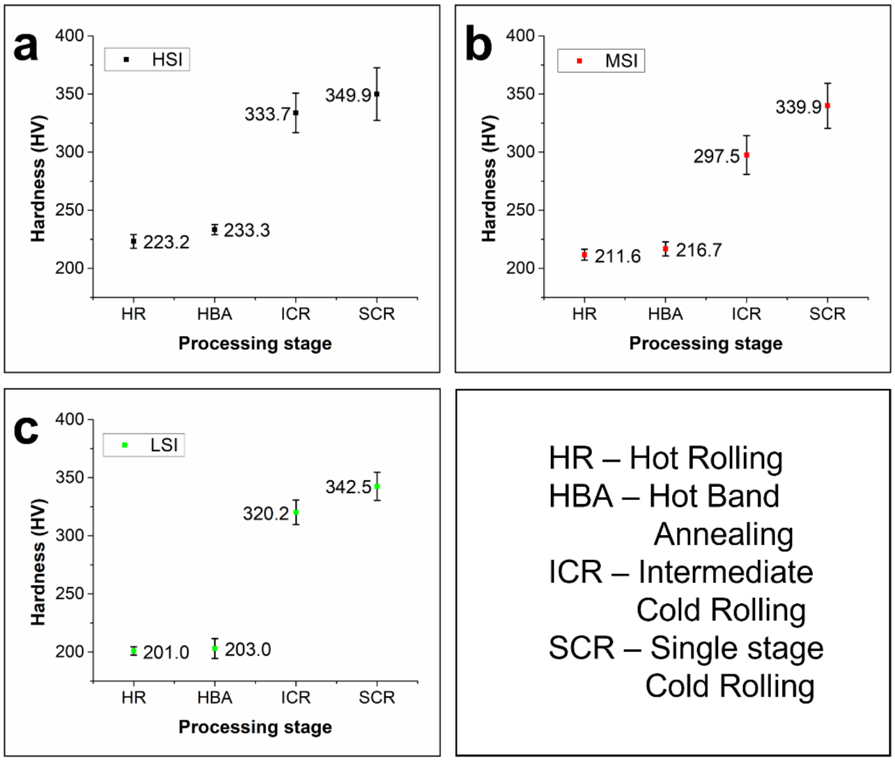

Figure 7.8: Microhardness (average of at least 10 measured values) after HR, HBA, ICR and SCR of (a) HSI, (b) MSI and (c) LSI steels through the thickness along ND-RD longitudinal section

7.7. VPSC model predictions

The starting crystallographic texture before cold rolling was assumed to be random. Plane strain compression with the following velocity gradient tensor (equation(3)) was considered to simulate the rolling texture.

$$L = \begin{bmatrix} 1 & 0 & 0 \\ 0 & 0 & 0 \\ 0 & 0 & -1 \end{bmatrix} \tag{7.4}$$

{110}<111> and {112}<111> slip systems were considered to be operative during plastic deformation in all three alloys. In pure iron {110}<111> slip system is expected to be the primary slip system with lowest CRSS and {112}<111> slip system act as the secondary slip system with slightly higher CRSS (Du et al. 2018). However, the addition of Si was anticipated to reduce the CRSS difference between {110}<111> and {112}<111> slip systems, and the same can cause some considerable difference in the overall texture development. In the present study, to incorporate the role of Si content, three different combinations of hardening parameters were assumed as shown in **Tables 3.5**, **3.6** and **3.7**.

The predicted texture developed under plane strain compression after increasing the strain level for cases I, II and III starting from random texture is shown in **Fig. 7.9**. α- and γ-fiber textures were expected to develop at 0.5 true strain in all three cases with no significant variation. The volume fraction of major texture components was estimated considering 15° threshold for different thickness reduction and are listed in **Table 7.2**. With increase in strain, the volume % of {111}<112> component increased in all the cases. At 2.0 strain, the volume fraction of {111}<112> was maximum (around 47%) in case-I and minimum (around 34%) in case-III. On the other hand, the amount of {111}<110> component decreased with the increment in strain. Interestingly, the rotated cube texture was found to increase up to 35 % for 2.0 strain in case-I whereas in other cases (case-I and case-II) it decreased up to <10% for 2.0 strain. The volume % of Goss orientation in the starting random texture was around 7.4% which reduced to <0.5% on application of 1.0 true strain. VPSC simulation again confirms the instability of Goss orientation under plane strain compression.

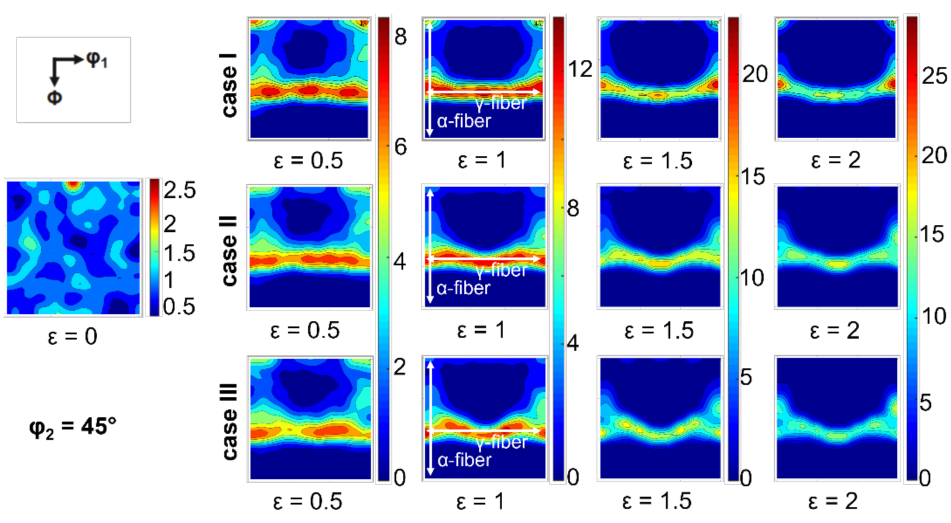

Figure 7.9: φ_2 = 45° ODF maps (as per Bunge notation) generated during VPSC simulation starting from random texture (ε = 0) subjected to plane

strain compression at true strain ε = 0.5, ε = 1, ε = 1.5, and ε = 2 for cases I, II and II mentioned in Tables 3.5, 3.6 and 3.7, respectively

Table 7.2: Volume % of different orientations based on VPSC simulation for cases I, II and III at different true strains (ε = 0, ε = 0.5, ε = 1, ε = 1.5 and ε = 2)

	Volume % of different orientations in case I			
True strain	**Goss**	**{111}<112>**	**{111}<110>**	**{001}<110>**
0	7.36	6.09	9.24	8.58
0.5	1.65	15.45	26.76	25.17
1	0.41	28.18	25.86	29.13
1.5	0	40.61	17.86	32.36
2	0	46.8	15.7	34.92
	Volume % of different orientations in case II			
True strain	**Goss**	**{111}<112>**	**{111}<110>**	**{001}<110>**
0	7.36	6.09	9.24	8.58
0.5	1.84	15.02	28.42	22.49
1	0.04	27.17	31.46	17.21
1.5	0	33.62	28.01	13.75
2	0	37.07	22.21	10.17
	Volume % of different orientations in case III			
True strain	**Goss**	**{111}<112>**	**{111}<110>**	**{001}<110>**
0	7.36	6.09	9.24	8.58
0.5	1.86	15.46	29.56	22.21
1	0.01	27.53	35.79	14.49
1.5	0	31.95	33.44	9.03
2	0	33.88	26.45	5.25

7.8. Discussion

The cracking phenomenon was found to be directly related with the Si content in Fe-Si steel, **Fig. 4.2(a, b)**. High Si was expected to increase the flow stress and thereby increase the hardness, **Fig. 7.8**. FEM analysis revealed that the rolling load, **Fig. 7.1**, and tensile stresses, **Figs. 7.2, 7.3**, developed during rolling increases with the increase in flow stress of the F-Si alloy. In fact, the increase in hardness (15%) and the increase in maximum tensile stress (14.5%) along both ND and RD was almost similar for increasing Si from 2.98 wt.% to 3.78 wt.%. On the other hand, Si was also reported to promote fracture as it reduces the cleavage fracture stress (Gerberich et al. 1981). All these factors contributed to the formation of edge cracks and alligator crack in HSI steel, **Fig. 4.2(a, b)**.

The macrotexture results after ICR and SCR showed that, two γ-fiber texture components, {111}<112> and {111}<110>, were prominent in all three Fe-Si steels, **Fig. 7.7(a-f)**. However, the volume fraction of rotated cube orientation was higher in HSI, **Table 7.1**. Similar observation was reported in another study where it was shown experimentally that the activation of secondary slip system(s) contributes to the development of rotated cube orientation during cold rolling of Fe - Si alloy (Taoka et al. 1966). The amount of rotated cube orientation in the cold rolled microstructure may be crucial. As the grains having rotated cube orientation remain almost undeformed during cold rolling, it is expected that those grains do not take part in the subsequent primary recrystallization. The unrecrystallized rotated cube oriented grains may thereby influence the abnormal grain growth of Goss orientation during secondary recrystallization (Song et al. 2021, Wang, Xu, Zhang, Fang, Lu, Misra, et al. 2015). In the present study, with the help of VPSC simulation, the rotated cube ({001}<110>) orientation was expected to develop with high intensity when the hardening parameters of {110}<111> and {112}<111> slip systems were equivalent (case I), **Fig. 7.9**. However, rotated cube orientation was predicted to be unstable when CRSS of {110}<111> slip system was gradually decreased (case II and III). The experimental observations also validate the predictions made by employing VPSC simulation. On the other hand, Goss texture was found negligible in different cold rolled samples (ICR and SCR) in all three Fe-Si steels, **Table 7.1**. Also, crystal plasticity based analysis predicted that Goss texture was not expected to evolve under plane strain compression in any of the three cases, **Fig. 7.9**. In fact, the activation of different slip systems did not play any role in the stability of Goss orientation. In all the cases the Goss texture was found to be highly unstable under plane strain compression.

The development of shear bands during cold rolling was found to be dependent on the Si level of Fe-Si steel. The shear bands in HSI after 50% thickness reduction (ICR) was thicker and widely spread, **Fig. 7.5(a, d)**, compared to the shear bands which formed in MSI, **Fig. 7.5(b, e)**. The width of shear bands further becomes thinner and were closely spaced in LSI after ICR, **Fig. 7.5(c, f)**. Although shear banding is an inhomogeneous deformation process, the crystallographic slip may have an impact on shear band formation (Dorner et al. 2005). In general, CRSS of primary and secondary slip systems in BCC-ferrite are in close proximity, and varying chemical composition in Fe-Si steel may alter the close packing of planes. It was reported that increasing the carbon content in Fe-3wt.% Si steels can promote the activation of secondary and tertiary slip systems during deformation (Takenaka et al. 2018b). Moreover, in some other studies, the activation of secondary slip systems has also been observed in Fe-Si steels even when silicon content reaches 4.4 wt.% (Takeuchi et al. 1967, Taoka et al. 1966). The activation of more slip systems contributes to strain hardening. Therefore, high strain hardening due to more active slip systems might have promoted higher instability in the form of thick shear bands in HSI steel compared to MSI and LSI alloys after ICR ($\varepsilon = 0.82$), **Fig. 7.5(a-f)**. Apart from higher glide stress of dislocations, higher strain hardening might have also contributed to high microhardness in HSI, **Fig. 7.8.** Since the increase in Si content increases the solid solution strengthening in iron and may as well promote the activation of secondary slip systems. As a result, the increase in Si concentration increases the strain hardening irrespective of the crystallographic orientation and hence increases the intensity of shear band formation in γ-fiber textured grains. More specifically, higher Si content is expected to reduce the degree of homogeneous deformation before the onset of shear bands in γ-fiber texture and thereby accelerate the shear band formation. However, on increasing strain during SCR (ε = 1.67), the deformation then continued to take place inside the shear bands and the difference in the width of shear bands in three different Fe-Si steels disappeared, **Fig. 7.6(a-f)**.

Further to confirm the capacity of shear bands in different alloys in originating the Goss orientation, partial recrystallization study has been carried out. Partial recrystallization was conducted at 650° C for 10 minutes on the SCR samples of HSI and LSI steels as shown in the IPF maps in **Fig. 7.10(a, b)**, respectively. ODF maps were also constructed for the regions shown in **Fig. 7.10(a, b)**, which are depicted in **Fig. 7.10(c, d)**. Clearly, the partially recrystallized regions are the shear band regions, as the grains started recrystallizing in the direction of shear bands due to high strain accumulation. Importantly, Goss oriented grains were found to develop among those recrystallized grains, **Fig. 7.10(a-d)**. However, no difference was found in the development of Goss oriented grains in two varieties of CRGO steel. In our other work, it was demonstrated in detail that the shear bands of {111}<112> component of γ-fiber texture were the origin of Goss orientation (Jain, Modak, et al. 2022). Although, with the increasing in Si concentration, the intensity of γ-fiber texture components was predicted to increase, **Fig. 7.9** and **Table 7.2**. No clear evidence was found in support of it. Macrotexture study revealed that the volume fraction of {111}<112> component was almost same in all the cases with an exception in ICR sample of HSI. The shear bands formed inside {111}<112> component of γ-fiber texture during cold rolling can act as the source of Goss orientation in CRGO steel, and hence, their development on subsequent primary recrystallization was not expected to get affected by changing Si concentration.

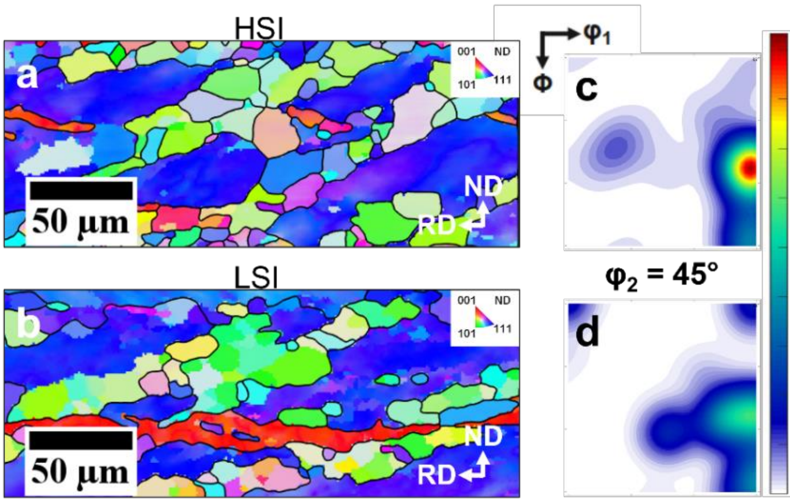

Figure 7.10: Partially recrystallized shear band regions after annealing single stage cold rolled samples of (a) HSI and (b) LSI at 650° C for 10 minutes, and (c, d) $\varphi_2 = 45°$ ODF maps (as per Bunge notation) of regions shown in (a) and (b), respectively

7.9. Conclusions

The following conclusions can be drawn from the present study:

a) Cracking phenomenon was observed during cold rolling of HSI steel, whereas cold rolling of MSI and LSI steels was successful. FEM based study suggests that increase in silicon content in Fe-Si steel gives rise to rolling load and tensile stresses, which resulted in the formation of edge cracks and alligator crack in HSI steel.

b) After cold rolling, the volume % of rotated cube orientation increased in HSI, compared to MSI and LSI steels. Crystal plasticity based analysis suggests that the reduction in the difference between critical resolved shear stress of primary ({110}<111>) and secondary ({112}<111>) slip systems in BCC-ferrite leads to the development of rotated cube orientation in HSI.

c) Goss orientation was found negligible after cold rolling in all three Fe-Si steels. Crystal plasticity based analysis indicates that Goss orientation was unstable under plane strain deformation, and its stability does not depend up on the activation of secondary ({112}<111>) slip systems.

d) Partial recrystallization study showed that the development of Goss oriented grains inside shear bands of {111}<112> component of γ-fiber texture was similar in different Fe-Si steels. These shear bands can act as the source of Goss orientation in cold rolled grain oriented steel, and its development on subsequent primary recrystallization stage does not depend up on the silicon content.

CHAPTER 8

Study on the development of Goss texture in cold rolled grain oriented steel: Role of sheet thickness

8.1 Introduction

Goss orientation was shown to originate at the surface layers due to high shear deformation during hot rolling (Matsuo et al. 1986, Mishra et al. 1986, Böttcher et al. 1993, Humane et al. 2015). Buttcher et al. (Böttcher et al. 1993) delineated that the removal of hot rolled surface layers has a detrimental effect on the development of Goss texture at the end during secondary recrystallization. A few authors have shown that the Goss oriented grains were initially formed during hot rolling, which gets diminished during cold rolling but redevelops subsequently after primary recrystallization at surface regions as a result of texture memory effect (Mishra et al. 1986, INOKUTI et al. 1983, Inokuti 1996). Dorner et al. (Dorner et al. 2007) also demonstrated that the Goss oriented sub-grain structure developed inside the microbands of γ-fiber (ND||<111>) texture during cold rolling was related to the initial Goss orientation. On the contrary, Heo et al. (Heo et al. 1999) showed that the new Goss oriented grains formed during cold rolling were not related to the pre-existing Goss oriented grains. Song et al. (Song et al. 2017) have also studied the microstructure and texture development in the CRGO steel and exhibited that despite no Goss orientation formed in the hot rolled structure, sharp Goss texture developed during secondary recrystallization.

Several studies have reported that the evolution of Goss oriented grains during cold rolling were related to the shear band formation (I. Samajdar et al. 1998, Park et al. 2003, Song et al. 2017, Ushioda et al. 1989). The development of shear bands generally depends up on various factors such as grain size, crystallographic orientation, and strain rate. Different crystallographic orientations were shown susceptible to shear band formation owing to high Taylor factor (SHIN et al. 2008, Nguyen-Minh et al. 2012, Mehdi et al. 2020). But, due to high strain, it often becomes difficult to examine the orientations developed inside those shear bands. Nevertheless, a clear evidence has been given in a study, in which Goss oriented grains were shown to develop inside the shear bands of {111}<112> oriented grains during cold rolling (Jain, Modak, et al. 2022). Furthermore, in some studies, it was shown that shear bands at the surface layers constitutes relatively high fraction of Goss oriented grains compared to those formed at mid-thickness region of the cold rolled sheet (Park et al. 2011, Park et al. 2013). Whereas other studies illustrated that the Goss oriented grains which evolved during intermediate annealing and primary recrystallization after different cold rolling stages, were irregularly formed at different positions throughout the thickness inside shear bands (Park et al. 2003, Wang, Xu, Zhang, Fang, Lu, Liu, et al. 2015). These above arguments raise questions on the formation of shear bands depending up on the thickness of the cold rolled sheet which may affect the development of Goss orientation during subsequent primary recrystallization stage.

Present study explores the formation of Goss oriented grains at different thickness level during cold rolling process. Crystal plasticity based analysis has been incorporated to understand the stability of Goss orientation during cold rolling. The aim of the present work is to provide an insight on the development of Goss texture in CRGO steel based on sheet thickness.

8.2 Microtexture analysis from hot rolling to single stage cold rolling

IPF-ND map of the hot rolled and hot band annealed samples are shown in **Fig. 8.1(a, b)**, respectively. Extremely large columnar grains with θ-fiber texture were found to remain underformed during hot rolling. After annealing, such underformed grains remained unrecrystallized, while the recrystallized grains were observed at surface and along the grain boundaries. Large Goss oriented grains were also present in the hot rolled sample which remained unrecrystallized after hot band annealing as indicated by black arrows in **Fig. 8.1(a, b)**. Most probably, these large Goss oriented grains were derived from the reheated microstructure. On the other hand, the recrystallized Goss oriented grains were also found in the hot band annealed structure. These Goss oriented grains were observed either at the surface or near the grain boundaries as indicated by red arrows in **Fig. 8.1(b)**. EBSD analysis was conducted on the intermediate cold rolled sample which is shown in the IPF-ND map (50% thickness) in **Fig. 8.1(c)**. The microstructure and texture development were inhomogeneous through the thickness. Some of the grains were heavily deformed and high strain accumulation inside those regions was responsible for the non-indexed points. The fragments of Goss oriented grains were found in the intermediate cold rolled sample as indicated by white arrows in **Fig. 8.1(c)**. Through thickness IPF-ND map of the single stage cold rolled sample is shown in **Fig. 8.1(d)**. Although, low deformation was observed inside some of the large grains at the mid-thickness region. Most of the regions through thickness underwent severe deformation during single stage cold rolling. The inhomogeneous deformation in the form of shear bands was observed to develop. Most of the shear band formation was found to occur inside γ-fiber textured grains. Importantly, no trace of Goss orientation was found after single stage cold rolling, **Fig. 8.1(d)**.

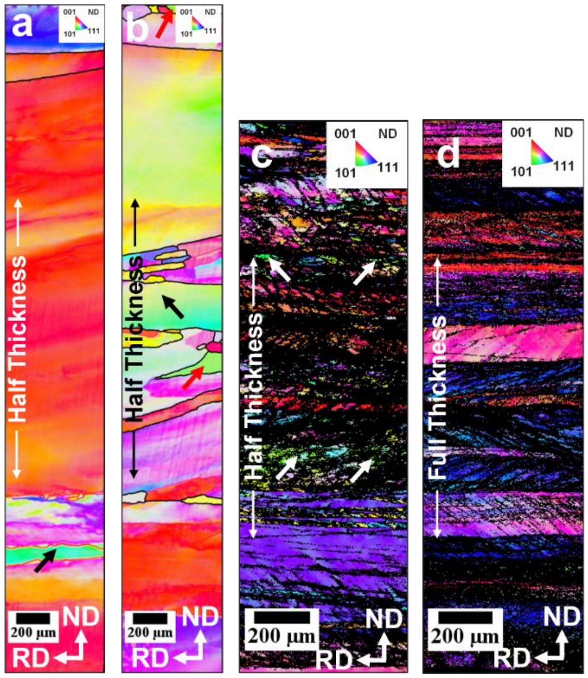

Figure 8.1: Half thickness IPF-ND maps of ND-RD longitudinal section (a) after hot rolling, (b) after hot band annealing at 800° C for 30 minutes in air, and (c) of intermediate cold rolled sample attaining 0.82 true strain, and (d) Full thickness IPF-ND map along ND-RD longitudinal section of the single stage cold rolled sample achieving 1.67 true strain

8.3 Through thickness macrotexture analysis after single stage cold rolling

Macrotexture analysis was conducted at different thickness level on the plane parallel to RD-TD of the single stage cold rolled sample. The ODF maps calculated at different regions along thickness (surface, 1/8th from surface, 1/4th from surface, 3/8th from surface and center) are shown in **Fig. 8.2(a-e)**. The volume % of different orientations were also calculated based on those ODFs as shown in **Table 8.1**. Mostly, α-, γ- and θ-fiber textures were developed after single stage cold rolling and volume fraction of the respective orientations were found to vary through the thickness. The center region was mostly occupied by θ-fiber texture and similar observation was also made in microtexture study, **Fig. 8.1(d)**. On the other hand, the volume fraction of Goss orientation was found be negligible (<1%) in all the cases. Interestingly, the volume fraction of rotated cube texture was found to decrease with increase in distance from the surface except at the center region. Moreover, the volume % of {111}<112> and {111}<110> components of γ-fiber texture was increased significantly with increase in distance from the surface and the magnitude of increment was higher for {111}<112> orientation.

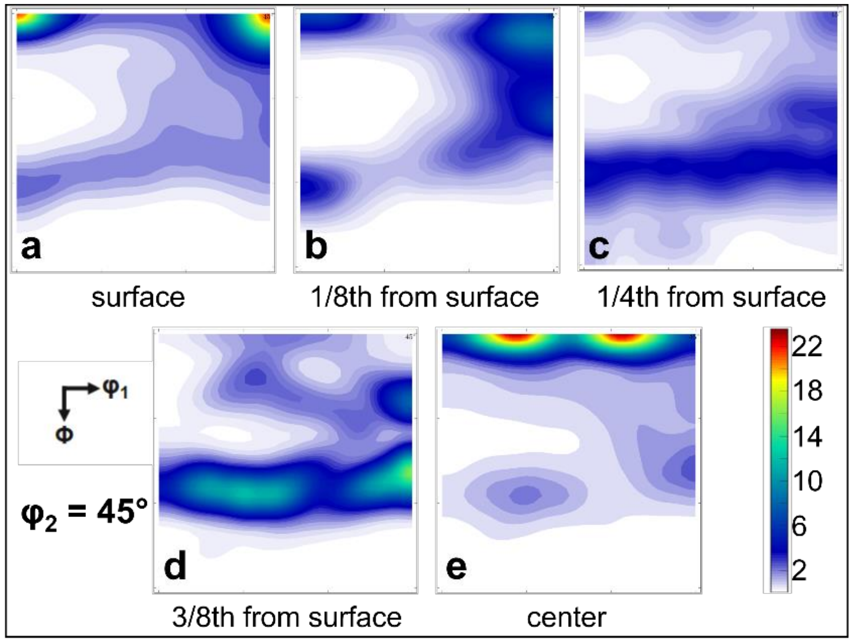

Figure 8.2: φ_2 = 45° ODF maps based on Bunge notation showing macrotexture analysis conducted on single stage cold rolled sample at (a) surface, (b) 1/8th from surface, (c) 1/4th from surface, (d) 3/8th from surface, and (e) center

Table 8.1: Volume % of various orientations based on macrotexture analysis on single stage cold rolled sample at different thickness level

Thickness level	{110}<001> (Goss)	{111}<112>	{111}<110>	{001}<110>
surface	0.5	6.4	6.4	16.5
1/8th from surface	0.3	4.8	7.5	11.0
1/4th from surface	0.9	11.0	11.9	3.0
3/8th from surface	0.2	22.9	14.3	1.2
center	0.3	5.9	3.4	8.1

8.4 Through thickness microtexture analysis after single stage cold rolling

Fig. 8.3(a) shows band contrast map of the single stage cold rolled sample. Shear bands were formed at different location through the thickness of the cold rolled sheet which were identified as the dark colored regions inclined at certain angle from RD, **Fig. 8.3(a)**. The shear band regions close to surface, close to quarter thickness and close to center are marked as 1, 2 and 3, respectively. EBSD analysis was then conducted separately on these shear band regions at higher magnification. IPF-ND maps of shear band regions 1, 2 and 3 are shown in **Fig. 8.3(b, c, d)**, respectively. ODF maps were also constructed for these three regions which are shown in **Fig. 8.3(e, f, g)**. Clearly, in all the cases the shear bands were found to develop inside {111}<112> component of γ-fiber texture. No significant difference between those shear bands with respect to sheet thickness was noticed.

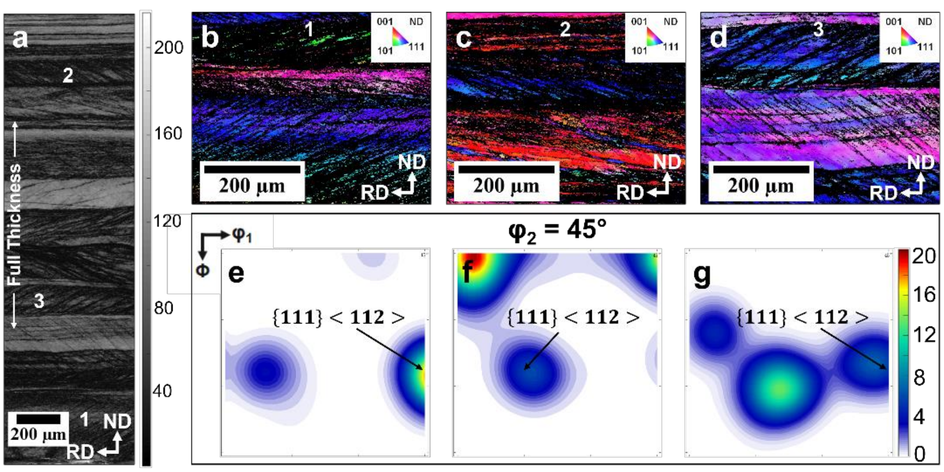

Figure 8.3: (a) Full-thickness band contrast map of ND-RD longitudinal section after single stage cold rolling, (b, c, d) IPF-ND maps of shear band regions developed close to surface, close to quarter thickness, and close to center marked in (a) as 1, 2 and 3, respectively, and (e, f, g) $\varphi_2 = 45°$ ODF as per Bunge notation for regions 1, 2 and 3 shown in (b, c, d), respectively

8.5 Discussion

The Goss oriented grains were found to exist in the hot rolled and hot band annealed microstructure, **Fig. 8.1(a, b)**. However, during intermediate cold rolling, Goss oriented grains were found to be heavily deformed irrespective of their position through the thickness, **Fig. 8.1(c)**. Further, after single stage cold rolling, the Goss orientated grains were completely diminished, **Fig. 8.1(d)**. Macrotexture analysis revealed that the volume fraction of Goss orientation after single stage cold rolling was less than 1% at various locations throughout the thickness, **Fig. 8.2(a-e)**. The instability of Goss orientation under plane strain deformation has been reported earlier (Hölscher et al. 1991, Raabe et al. 2002). It signifies that even though Goss oriented grains were significantly developed at the surface and grain boundaries prior to cold rolling, the survival of Goss orientation becomes highly uncertain during cold rolling. Experimental results confirm that not only at the mid-thickness region, but it was also highly improbable that the Goss oriented grains would be able to survive even if they were present near the surface of the hot rolled sheet. In general, at the mid thickness of a rolled sheet plane strain condition prevails with zero shear components. However, friction between roller's surface and the sheet surface leads to the evolution of non-zero shear component (L_{13}) in the velocity gradient tensor close to the plate surface (Engler et al. 2000). In addition to the evolution of different texture components, the shear deformation also plays a crucial role on the stability of different texture components such as, Goss texture, during cold rolling. To understand whether Goss orientation is expected to be stable under the shear deformation at the plate surface, VPSC simulation has been carried out considering only shear deformation with the following velocity gradient:

$$L = \begin{bmatrix} 0 & 0 & 1 \\ 0 & 0 & 0 \\ 0 & 0 & 0 \end{bmatrix} \tag{8.1}$$

The ODFs constructed after applying different amount of shear strain (ε_{13}) are represented in **Fig. 8.4**. Interestingly, it has been found that Goss orientation was expected to be stable up to 1.5 true strain (ε_{13}). On the other hand, the stability of Goss orientation under plane strain compression was discussed in **Chapter 6**, **Fig. 6.12**. It was found that Goss orientation was not stable on and above 0.5 true strain (ε_{33}) under plane strain compression. Although the Goss texture was expected to survive up to 1.5 strain under only shear loading, experimentally the volume fraction of Goss orientation was found to be negligible (<1%) at the surface, **Fig. 8.2(a)**. Most probably, in the present case no shear loading acted near to the surface otherwise, Goss orientation would have existed in more amount. Detailed FEM analysis is required to confirm the nonoccurrence of shear component in velocity gradient tensor.

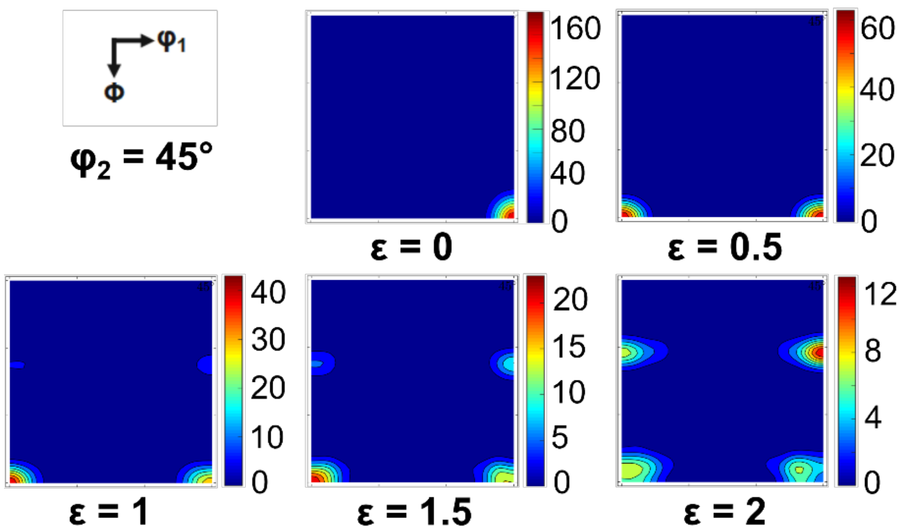

Figure 8.4: φ_2 = 45° ODF maps based on Bunge notation showing VPSC simulation starting with Goss orientation subjected to shear deformation at true strain (ε) 0, 0.5, 1, 1.5 and 2

On the other hand, shear bands were developed during single stage cold rolling. The formation of shear bands was observed at different locations throughout the thickness, **Fig. 8.1(d)** and **8.3(a)**. All these shear bands were formed inside {111}<112> component of γ-fiber texture as shown in **Fig. 8.3(b-g)**. Moreover, no change in the inclination angle of the shear bands at various thickness has been noticed. Taylor factor helps in understanding about the preference of orientation which can develop shear bands (Piehler 2009). Taylor factor map was generated for different orientations under plane strain and shear deformation mode as shown in **Fig. 8.5(a, b)**, respectively. High Taylor factor infers that larger slip activities leading to increase in dislocation densities can cause instability during high deformation (SHIN et al. 2008, Nguyen-Minh et al. 2012, Mehdi et al. 2020). Taylor factor of {111}<112> component was estimated to be 3.18 and 2.02 under plane strain compression and shear deformation, respectively, **Fig. 8.5(a, b)**. Therefore, the shear banding was not expected inside {111}<112> orientation if we assume that the mode of deformation was shear at the surface, since the corresponding Taylor factor is low (2.02). High strain hardening inside γ-fiber texture components under plane strain during cold rolling may have caused shear band formation irrespective of its position along the thickness. However, due to high strain accumulated inside narrow shear bands, it becomes difficult to investigate the orientations formed inside them, **Fig. 8.3(b-d)**.

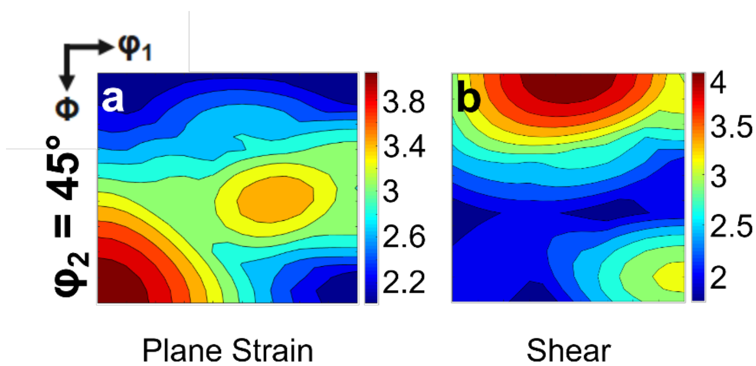

Figure 8.5: Taylor factor calculated for different orientations under (a) plane strain and (b) shear deformation superimposed over $\varphi_2 = 45°$ ODF map as per Bunge notation

Partial recrystallization was performed on single stage cold rolled sample at 625° C for 5 minutes to examine the orientations developed inside the shear bands. Full-thickness IPF-ND map of the partially recrystallized sample is shown in **Fig. 8.6(a)**. Grains started recrystallizing from inside high strained regions such as shear bands, throughout the thickness, while other regions remained unrecrystallized. Partially recrystallized shear band regions close to surface and close to center are marked as 1 and 2, respectively, **Fig. 8.6(a)**. EBSD analysis was further performed on regions 1 and 2 at higher magnification and the IPF-ND maps are shown in **Fig. 8.6(b, c).** ODF maps were also constructed for those regions which are exhibited in **Fig. 8.6(d, e)**, respectively. Most of the recrystallized grains developed inside the shear bands of {111}<112> oriented grains have Goss orientation. In Chapter 6, it was demonstrated that Goss oriented grains were developed inside shear bands of {111}<112> oriented grains due to crystal rotation associated with geometrical softening phenomenon. Taylor factor of Goss component was estimated to be 2.12 and 3.0 (3.18) under plane strain compression and shear deformation, respectively, **Fig. 8.5(a, b)**. Therefore, the plane strain compression was expected to cause geometrical softening, whereas under shear deformation the shear band would have been accompanied by geometrical hardening which is not feasible. In the present study, there was no significant difference found in the development of Goss oriented grains inside those shear bands at different positions of the cold rolled sheet.

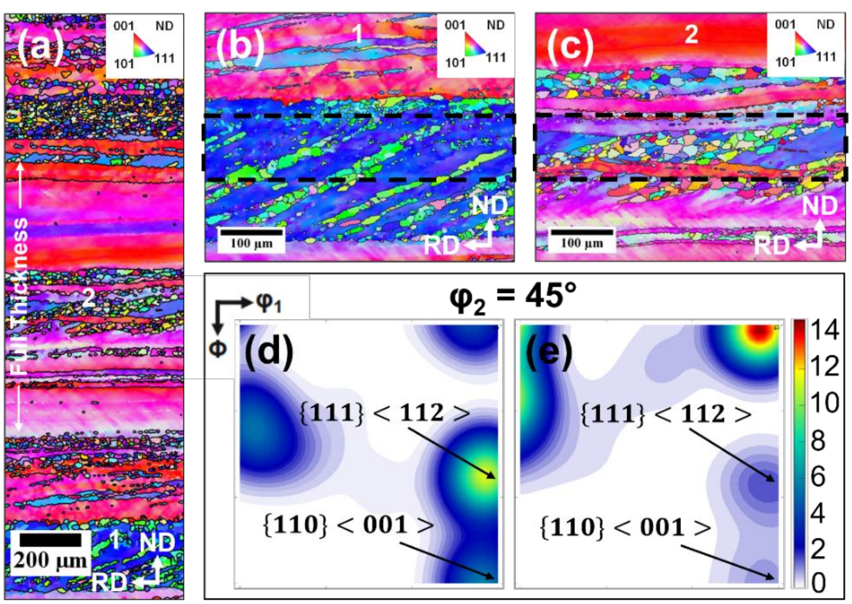

Figure 8.6: (a) Full-thickness IPF-ND map of ND-RD longitudinal section after partial recrystallization of single stage cold rolled sample at 625° C for 5 minutes, (b, c) IPF-ND maps of regions 1 and 2 marked in (a), respectively, showing the grains recrystallized inside shear bands located at

different position along the thickness, (d, e) $\varphi_2 = 45°$ ODF maps as per Bunge notation for region 1 and 2 shown in (b, c), respectively

Further, the partially recrystallized shear band regions 1 and 2 was considered to evaluate the difference in the development of Goss oriented grains based on thickness level as marked by dotted black color rectangular regions in **Fig. 8.6(b, c)**. The area fraction of Goss oriented grains, deviated up to 15° from the ideal Goss orientation, was calculated with respect to area of the selected region as shown in **Table 2**. Goss oriented grains developed near the surface layers during partial recrystallization, were slightly higher (10%) than at the regions close to the centre, **Fig. 8.6(b-e)** and **Table 2**. However, the main constituent responsible for the development of these Goss oriented grains was the shear bands formed inside large grains having {111}<112> orientation during cold rolling. Hence, the Goss oriented grains evolving inside the shear bands of {111}<112> oriented grains can act as the source of Goss texture in CRGO steel irrespective of the position along the thickness. But it is important to state that in correlation with the actual industrial rolling, since the actual final sheet thickness is around 0.2 mm, the shear bands forming at the regions close to surface may have greater contribution on the Goss texture development in CRGO steel.

Table 2: Area fraction of the Goss oriented grains, deviated up to 15° from the ideal Goss orientation, with respect to the selected region inside partially recrystallized shear bands of {111}<112> oriented grains

Shear band region of {111}<112> oriented grain (500x100 μm^2)	Deviation angle from the ideal Goss orientation	Area fraction (%) of Goss oriented grains w.r.t. shear band region
Region 1	5°	6.1
	10°	17.0
	15°	22.3
Region 2	5°	3.6
	10°	7.1
	15°	13.1

8.6 Conclusions

The following conclusions can be drawn from the above study:

a) Goss oriented grains formed during hot rolling and hot band annealing, did not remain stable during cold rolling operation even at the surface. However, crystal plasticity based analysis suggests that Goss orientation is expected to be stable under shear deformation.

b) Shear bands were formed inside grains having {111}<112> component of γ-fiber texture during cold rolling irrespective of the sheet thickness. Despite low Taylor factor of {111}<112> orientation under shear deformation, shear bands were found to form at the surface of the cold rolled sheet inside {111}<112> oriented grains.

c) Partial recrystallization study revealed that the development of Goss orientation inside the shear bands of {111}<112> oriented grains does not depend up on sheet thickness.

CHAPTER 9

Conclusions and future scope of work

9.1 Conclusions

Three CRGO steels having silicon content 2.98 wt.%, 3.23 wt.% and 3.78 wt.% were prepared in the present study. Step by step development of microstructure and texture has been studied to understand the development of Goss texture in Fe-3.78wt. % Si CRGO steel. Moreover, crystal plasticity based analysis has been incorporated to understand the origin of Goss texture. An attempt has also been made to understand the state of stress during rolling simulation using finite element method. The major conclusions of the present study are summarized below:

- Cold rolling down to 1.5 mm thickness was successfully achieved without any intermediate annealing treatment for up to 3.23 wt.% silicon.
- Edge crack and alligator crack developed in 3.78wt.% silicon steel were successfully eliminated after providing hot band annealing and intermediate annealing treatments, respectively.
- The development of Goss orientation in cold rolled grain oriented steel was not dependent on silicon content.
- Goss oriented grains developed prior to cold rolling were unstable during cold rolling irrespective of their position along the thickness.
- Shear bands formed inside {111}<112> component of γ-fiber texture were the origin of Goss orientation developed during primary recrystallization.
- Intermediate annealing between cold rolling passes is not essential to develop Goss texture in cold rolled grain oriented steel.
- Abnormal grain growth of Goss oriented grains has not been observed in the final microstructure after secondary recrystallization.

However, it is important to state that the above conclusions are drawn based on the experiments performed in the laboratory scale where the final sheet thickness was around 1.5 mm. In actual industrial practice, sheet thickness around 0.15-0.22 mm is achieved. Therefore, careful consideration of other factors is required before generalizing the results for industrial production.

9.2 Future scope of work

Based on the present study, the following points can be considered as the future scope:

- Computational studies can further be carried out to understand the limits of Taylor factor ratios (between different crystallographic orientations) which leads to cracking due to strain incompatibility.
- A detailed TEM study needs to be carried out to characterize and quantify the nature and size of the precipitates at different locations such as grain interior, Goss grain boundaries and other grain boundaries.
- Future study can be addressed on the secondary recrystallization behavior of intermediate cold rolled samples.
- Study on the sharpness of Goss texture needs to be conducted in detail as less deviation from the ideal Goss orientation can improve the magnetic properties of grain oriented electrical steel.
- In order to understand the contribution of shear components in the velocity gradient tensor (L_{13}, L_{31}) at different level of sheet thickness during different stages of rolling, detailed FEM analysis needs to be carried out.
- The magnetic properties should be evaluated after achieving the desired Goss orientation in the final microstructure.

Appendix-A

Effect of tilt and twist angles on the cleavage crack propagation in ferritic steel

A.1 Introduction

The phenomenon of catastrophic cleavage fracture in BCC material limits its application at low temperature and high strain rate conditions. The resistance to cleavage fracture or ductile to brittle transition temperature of BCC material can be improved by modifying the grain structure, specifically by reducing the grain size and increasing the grain boundary misorientation angle (Knott 1973). The effect of reduction in grain size on cleavage fracture resistance is well studied and well understood (Knott 1973, Ghosh et al. 2013, Chakrabarti et al. 2009). As compared, less attention has been paid on how the grain boundary misorientation can influence the crack propagation. One of the major obstacles in addressing the above question lies in the difficulties associated with the Electron Back-Scatter Diffraction (EBSD) analysis on the fracture surface. Therefore, only a limited number of studies have been carried out to correlate cleavage fracture surface morphology with grain orientation (Bhattacharjee et al. 2002, Randle et al. 2005, Slavik et al. 1993). One of the pioneering works has been done by Bhattacharjee et al. (Bhattacharjee et al. 2002) by carrying out automatic EBSD scan over the fracture surface of low-C ferritic steel. They concluded that the angular misorientation up to 12° (considering the angle-axis pair) can exist within a single cleavage facet, defining the effective grain size (Kim et al. 1986, 2000). The justification provided for 12° threshold misorientation angle was 5% reduction in crack driving force. However, the reduction in crack driving force depends on the tilt and twist angle rather than misorientation angle. The quantitative measurement of change in fracture energy associated with crack deviation at grain boundary is very complex and requires extensive mathematical calculation (Qiao et al. 2003, Vasudevan et al. 2020) specially in Charpy impact tested sample. Furthermore, the crystallographic nature of the cleavage plane can be obtained from inverse pole figure, if the cleavage facet is parallel to the macroscopic fracture plane, which is improbable mostly. A stereological correction before EBSD scan is necessary to characterize the crystallographic cleavage plane, as reported by Randle et al. (Randle et al. 2005). EBSD analysis on the fracture surface is very challenging and there exists a high risk of wrong interpretation of results. Moreover, a disagreement regarding the correctness of EBSD data on the fracture surface persists since the facet deviates from an ideal 70° tilt condition.

In our previous work (Ghosh et al. 2014), it has been shown that the cleavage crack deviation depends on the angular difference between adjacent cleavage planes along the propagating crack, and the experimental observations of crack deviations were correlated with that angle considering the angle of projection on the observed surface. However, the role of these angular differences on the cleavage fracture surface morphology, and their effect on imposing a barrier to cleavage crack propagation have not been studied in detail to date. Understanding the role of grain boundary nature on crack deviation is crucial, and recently it has been reported that grain boundary nature severely affects the overall impact toughness (Ghosh et al. 2016, Chatterjee et al. 2018).The present work does not aim to correlate the grain boundary character with the overall property, rather it focuses on how the tilt and/or twist angle of the grain boundary character influence the cleavage crack propagation with the formation of different features at grain boundary.

A.2 Experimental details

Standard Transverse-Longitudinal (T-L) oriented Charpy impact sample of ferritic steel was subjected to impact loading at −196° C. To study the fracture surface, specimens were cut along the plane parallel to the macroscopic fracture plane with roughly 2 mm thickness using a slow speed diamond cutter, followed by ultrasonic cleaning and drying. Special caution has been taken to keep the flat cut surface exactly perpendicular to TD, as shown in **Fig. A.1**. A sample was placed on the 70° pre-tilted holder to carry out EBSD analysis. In the present case, although the actual fracture surface was not at 70° tilt condition and the tilting angle varies a great extent from facet to facet, the condition of 70° tilting about the reference axis (in this case TD) remains constant for all the cleavage facets. Therefore, the orientation obtained by EBSD analysis from different regions of the fracture surface was correct irrespective of their tilt angle. Instead, because of the arbitrary inclination of the neighboring cleavage facets, the Kikuchi pattern generated from a facet could not reach up to the camera. Therefore, the Kikuchi pattern recorded on the camera used to have some partial obstacles and may not be suitable for automatic analysis. So, in the present study, EBSD analysis has been carried out manually, point by point. In addition, the indexing of the Kikuchi pattern has been restricted to the obstructer free portion of the recorded pattern which was chosen manually. The orientation data was collected from at least five neighboring points for a single facet, and the grain boundary misorientation angle between different points of a single facet was always found to be less than 0.5°.

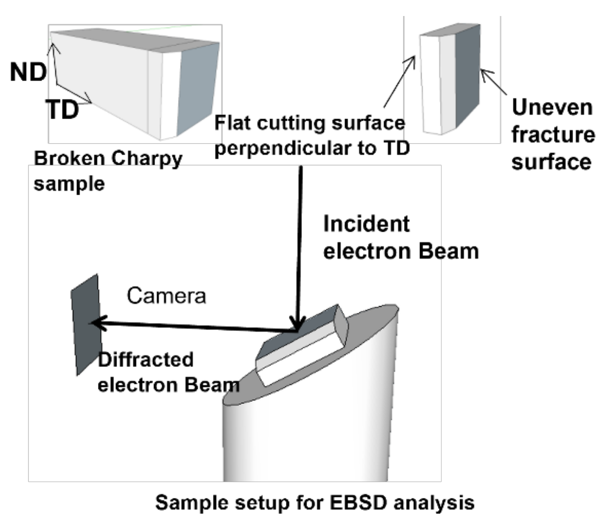

Figure A.1: Details of sample preparation and setup configuration for EBSD analysis

A.3 Results and Discussion

The fractographic region chosen for EBSD analysis is shown in **Fig. A.2**. The mode of fracture is completely transgranular cleavage as expected since the Charpy impact test was carried out at −196° C. The fracture surface is flat and consists of several cleavage facets. Different types of boundaries between the facets are observed and indicated by red arrows in **Fig. A.2**. Cleavage crack follows a path of a specific type of crystallographic plane during its propagation and deviates at grain boundary depending upon the orientation of neighboring grains. It is well established that in ferritic and martensitic steel, the cleavage fracture occurs along {001} planes (Randle et al. 2005, Bhattacharjee et al. 2002, Bhattacharjee et al. 2004, Kim et al. 2000, Kim et al. 1986) and the same has been considered to be the cleavage plane in the present study. The resistance and deviation of cleavage crack at grain boundary primarily depends on the grain boundary character. Bhattacharjee et al. (Bhattacharjee et al. 2004) followed a simplified approach to show that the crack deviation depends on grain boundary misorientation angle (i.e., angle-axis pair). The representation of grain boundary based on tilt and twist angle will be advantageous in terms of correlating the fractographic morphology at facet boundary with the nature of grain boundary. The possible tilt (α) and twist (φ) angle between the cleavage planes of the deviated crack at the grain boundary has been calculated by incorporating the orientation of neighboring crystals, grain boundary plane and the cleavage plane, following the approach proposed by (King et al. 2011, Zhai et al. 2000):

$$\varphi = cos^{-1}[(P_{gb}\ x\ P_{c1}) \cdot (P_{gb}\ x\ P_{c2})] \qquad \text{(a.1)}$$

$$twist\_axis = P_{gb}$$

where, P_{gb} is the unit normal to grain boundary plane, P_{c1} and P_{c2} are unit normal to the cleavage plane of two neighboring crystals in the sample reference frame. P_{c1} and P_{c2} can be obtained by incorporating the orientation of the crystals as follows:

$$P_{c1} = g_1^{-1} \cdot C_{c1} \tag{a.2}$$

$$P_{c2} = g_2^{-1} \cdot C_{c2} \tag{a.3}$$

where, g_1 and g_2 are orientation matrices of the crystals and C_{c1} and C_{c2} are the cleavage planes in crystal reference frame which is considered to be {001} plane.

Now, tilt angle can be obtained after eliminating the twisting effect as follows:

$$P'_{c2} = Rot_{twist}\ x\ P_{c2}; \tag{a.4}$$

Here, Rot_{twist} represents the rotation about P_{gb} axis with the twist angle φ. Hence, the tilt angle (α) can be measured by the following equation:

$$\alpha = cos^{-1}[P_{c1} \cdot P'_{c2}] \tag{a.5}$$

$$tilt\_axis = P_{c1}\ x\ P'_{c2};$$

The orientations of the crystals (g_1, g_2) containing the facets has been obtained by EBSD analysis on the fracture surface and allow us to estimate the possible tilt and twist angle at the grain boundary for the given combination of cleavage planes. Now, there are three possible cleavage planes (i.e., (001), (010) and (100)) in each crystal; therefore, there can be nine possible combinations of tilt and twist angles between the neighboring grains or there are nine possible paths for cleavage crack propagation. The direct experimental measurement of tilt and twist angle could be used to determine the selected crack path, but we could not perform the measurement of tilt and twist angle at the grain boundary on the fracture surface due to the extreme complexity of the experiment (Merson et al. 2016). In the present study it has been assumed that the crack is following the cleavage planes corresponding to lowest tilt and twist angle. And considering the lowest tilt and twist angle, the expected geometrical features at the boundary are compared with the fractographic features.

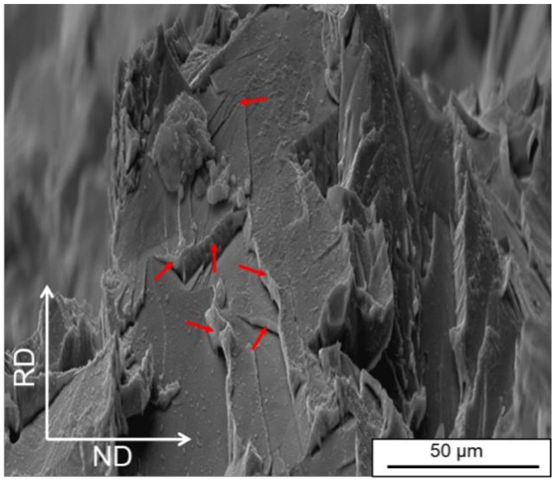

Figure A.2: FESEM image of the fracture surface showing the presence of cleavage facets and different types of boundaries

In the following section, different types of facet boundaries are studied considering the tilt-twist angle and fractographic features appeared at the grain boundary due to crack deviation.

Case I

The cleavage facets of interest are indicated by region 1 and region 2 in the fractograph shown in **Fig. A.3a**. The boundary between these regions is a typical example of tilt boundary. Kikuchi patterns collected from region 1 and region 2, are shown in **Fig. A.3b, c** respectively. The orientation obtained by EBSD analysis on region 1 and region 2 is given in **Table A.1**. Since, the Charpy samples were prepared from the warm rolled annealed plate, most of the grain boundaries are perpendicular to the ND of the rolling plate (King et al. 2011, Ghosh et al. 2016). The grain boundary plane in the present case is parallel to RD. The nine possible combinations of tilt and twist angles considering the orientations of regions 1 and 2 are calculated and reported in **Table A.2**. Twist angle is minimum (i.e. 1.8°) for the combination of (010)–(010) cleavage planes, while the combination of (001)–(001) cleavage planes have minimum possible tilt angle (i.e., 1.2°). The actual cleavage crack is expected to follow the combination of cleavage planes where it suffers less deviation or lowest possible reduction in fracture energy. And both tilt and twist components contribute to the crack deviation. Therefore, the combination of (001)–(001) cleavage planes are expected to provide the lowest resistance to cleavage crack since both the tilt and twist angles are very small (<4°) unlike other possible combinations. In line with the predicted tilt-twist angle, the actual tilt-twist angle between the facets in the fractograph, **Fig. A.3a**, seems to be very low. The relative orientation of neighboring facets considering (001)–(001) cleavage planes (or 1.2° tilt angle and corresponding 3.6° twist angle) is shown in the schematic presented in the inset of **Fig. A.3a** which showed very good agreement with the fractographic features at the grain boundary. However, in the present study, the actual tilt and twist angle between the cleavage facets are not measured experimentally. In this case, the neighboring grains, having low misorientation angle (i.e., 7.8°, **Table A.1**) do not provide any significant fractographic features at the grain boundary. Therefore, it seems to be ineffective in restricting cleavage crack propagation.

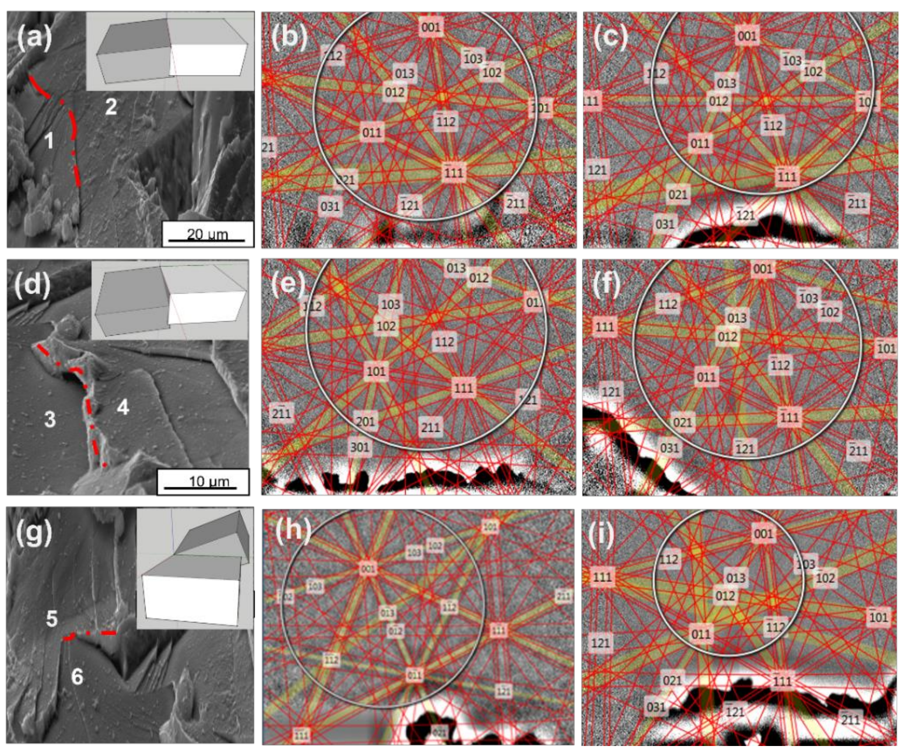

Figure A.3: (a, d, g) FESEM fractographs showing cleavage facets separated by different types of boundaries with schematic in inset showing relative orientation of neighboring facets, constructed based on the predicted tilt-twist angle, and (b, c, e, f, h, i) the Kikuchi patterns obtained from the regions 1,2,3,4,5 and 6, respectively, marked in the fractographs (a, d, g)

Table A.1: Euler's angle with the Mean Angular Deviation (MAD) and misorientation angle as obtained from the point of EBSD analysis on the cleavage face

Region	Orientation in Euler angle (°)			MAD (°)	Misorientation angle (°)
	φ_1	ϕ	φ_2		
1	7.88	82.89	56.21	0.45	7.83
2	4.26	84.07	63.48	0.63	
3	128.41	25.89	47.96	0.51	14.72
4	9.92	80.36	60.16	0.56	
5	69.99	74.9	5.88	0.34	41.6
6	125.87	24.3	48.5	0.75	

Table A.2: Calculated values of tilt and twist angles for the different combinations of cleavage planes

Case 1 (Grain boundary Perpendicular to ND)				Case 2 (Grain boundary Perpendicular to ND)				Case 3 (Grain boundary Perpendicular to RD)			
Twist angle (°)				**Twist angle (°)**				**Twist angle (°)**			
Cleavage Plane	100	010	001	Cleavage Plane	100	010	001	Cleavage Plane	100	010	001
100	2.4	17.1	75.9	100	32.8	11.1	73.4	100	60.1	21.8	69.2
010	12.8	1.8	88.9	010	63.2	84.9	10.6	010	24.4	73.7	15.3
001	81.9	83.4	3.6	001	12.2	34.0	61.5	001	75.7	22.4	66.6
Tilt angle (°)				**Tilt angle (°)**				**Tilt angle (°)**			
Cleavage Plane	100	010	001	Cleavage Plane	100	010	001	Cleavage Plane	100	010	001
100	7.3	38.2	49.6	100	39.9	22.7	28.6	100	51.9	15.5	37.9
010	29.4	7.1	39.4	010	75.8	12.4	21.8	010	54.1	19.1	29.2
001	70.0	19.3	1.2	001	5.3	54.3	54.5	001	43.2	62.2	45.6

Case II

A ridge zone is observed between the two facets at regions 3 and 4, **Fig. A.3d**. The Kikuchi patterns corresponding to the regions 3 and 4 are shown in **Fig. A.3e, f**, respectively. The misorientation angle between two facets is around 14.7°, **Table A.1**. Here, the lowest possible twist angle is 11.1° between (100)–(010) cleavage planes but the corresponding tilt angle is high, 22.7°. On the other hand, the minimum tilt angle (5.3°) is between (001) and (100) cleavage planes where the corresponding twist angle (12.2°) is also very close to theminimum twist angle value (11.1°), **Table A.2**. Therefore, considering both tilt and twist angle, the selected combination of cleavage planes is expected to be (001)–(100) cleavage planes, **Table A.2**. The relative orientation of neighboring facets based on the predicted tilt-twist angle is shown in the schematic presented in the inset of **Fig. A.3d**. Following the prediction, in the actual case, a clear microstructural feature comprising of a ridge zone is observed at the facet boundary, **Fig. A.3d**. The formation of ridge zone at the facet boundary is also expected to consume some energy and thus the facet boundary with 14.7° misorientation angle provide a significant barrier for cleavage crack propagation (Ghosh et al. 2016, Chatterjee et al. 2018).

Case III

A classical angular step formation has been observed at the boundary between regions 5 and 6, **Fig. A.3g**. The Kikuchi pattern corresponding to the regions 5 and 6 are shown in **Fig A.3h, i**, respectively. The boundary between these two facets is perpendicular to the RD, unlike the other two cases. The misorientation angle between these two regions is 41.6°, **Table A.1**. The calculated minimum possible twist angle is around 15.3°, and the corresponding tilt angle is 29.2°, for the combination of (010)–(001) cleavage plane, **Table A.2**. Another equal probable combination of cleavage plane is (100)–(010) where the corresponding twist and tilt angles are 21.8° and 15.5°, respectively. Here, the unambiguous prediction of actual crack path is not possible. But irrespective of the two possibilities, the twist angle is expected to be higher (>15°) in both the cases. The presence of angular step at facet boundary, **Fig. A.3g** indicates the existence of large twist angle. The schematic in inset, **Fig. A.3g**, shows the relative orientation of neighboring facets considering the combination of (100)–(010) cleavage plane where the twist angle was higher compared to the combination of (010)–(001) cleavage plane, is consistent with the fractographic observation made at the facet boundary, **Fig. A.3g**. Therefore, the angular step at the boundary between these two facets, having 41.6° misorientation angle, imposes a strong barrier to the cleavage crack propagation due to the formation of an additional surface.

In summary, the EBSD analysis on fracture surface allowed us to estimate the possible tilt and twist angle between the cleavage planes at the grain boundaries. The cleavage crack is assumed to propagate along the cleavage planes which possess lowest tilt and twist angles. The comparison between the schematic, showing relative orientation of neighboring facets, and the fractographic observation shows very good agreement.

A.4 Conclusions

The following conclusions can be derived from the above study:

a) Grain boundary character based on tilt and twist angle correlates to the fractographic features at facet boundary.
b) Both tilt and twist angle at grain boundary play a significant role in deciding the cleavage crack deviation at grain boundary.
c) High twist angle is responsible for the formation of new surface, ridge zone and angular step at facet boundary.

REFERENCES

Abbruzzese G.C., Fortunati S., and Campopiano A. (1992), On the Parameters Controlling the Kinetics of Secondary Recrystallization in Grain Oriented Silicon Iron, Mater. Sci. Forum, 94–96, 405–412 (10.4028/www.scientific.net/MSF.94-96.405)

Andersen I., Grong Ø., and Ryum N. (1995), Analytical modelling of grain growth in metals and alloys in the presence of growing and dissolving precipitates—II. Abnormal grain growth, Acta Metall. Mater., 43, 2689–2700 (10.1016/0956-7151(94)00489-5)

Atake M., Barnett M., Hutchinson B., and Ushioda K. (2015), Warm deformation and annealing behaviour of iron–silicon–(carbon) steel sheets, Acta Mater., 96, 410–419 (10.1016/j.actamat.2015.05.018)

Bao S., et al. (2017), Microstructure, texture and precipitates of grain-oriented silicon steel produced by thin slab casting and rolling process, J. Iron Steel Res. Int., 24, 91–96 (10.1016/S1006-706X(17)30013-4)

Barlow K.N., and Lancaster P.R. (1976), Investigation of internal flow occurring during a square-diamond rolling pass, using plasticine:as a model material, Met. Technol., 3, 503–509 (10.1179/030716976803391782)

Barlow K.N., Lancaster P.R., and Maddison R.T. (1984), Examination of surface defects induced during hot rolling of high-alloy steel bar and rod, Met. Technol., 11, 14–19 (10.1179/030716984803275214)

Bhattacharjee D., and Davis C.L. (2002), Influence of processing history on mesotexture and microstructure-toughness relationship in control-rolled and normalised steels, Scr. Mater., 47, 825–831 (10.1016/S1359-6462(02)00324-X)

Bhattacharjee D., Knott J.F., and Davis C.L. (2004), Charpy-impact-toughness prediction using an ‘effective’ grain size for thermomechanically controlled rolled microalloyed steels, Metall. Mater. Trans. A, 35, 121–130 (10.1007/s11661-004-0115-7)

Bhattacharya D., Poddar G.P., and Misra S. (2016), Centreline defects in strips produced through thin slab casting and rolling, Mater. Sci. Technol., 32, 1354–1365 (10.1080/02670836.2015.1125600)

Bhattacharya Diptak, Roy T.K., and Mahashabde V. V. (2016), A Study to Establish Correlation Between Intercolumnar Cracks in Slabs and Off-Center Defects in Hot-Rolled Products, J. Fail. Anal. Prev., 16, 95–103 (10.1007/s11668-015-0050-5)

Bode O., Schwerdtfeger K., Geck H.G., and Höfer F. (2008), Influence of casting parameters on void volume and centre segregation in continuously cast 100Cr6 blooms, Ironmak. Steelmak., 35, 137–145 (10.1179/030192307X233511)

Böttcher A., and Lücke K. (1993), Influence of subsurface layers on texture and microstructure development in RGO electrical steel, Acta Metall. Mater., 41, 2503–2514 (10.1016/0956-7151(93)90331-L)

Byon S.M., Roh Y.-H., Yang Z., and Lee Y. (2021), A roll-bending approach to suppress the edge cracking of silicon steel in the cold rolling process, Proc. Inst. Mech. Eng. Part B J. Eng. Manuf., 235, 112–124 (10.1177/0954405420949221)

Calvillo P.R., Ros-Yanez T., Ruiz D., Colás R., and Houbaert Y. (2006), Plane strain compression of high silicon steel, Mater. Sci. Technol., 22, 1105–1111 (10.1179/174328406X114207)

Campos M.F. De, et al. (2004), Effect of the Hot Band Grain Size and Intermediate Annealing on the Deformation and Recrystallization Textures in Low Silicon Electrical Steels, ISIJ Int., 44, 591–597 (10.2355/isijinternational.44.591)

Chakrabarti D., Strangwood M., and Davis C. (2009), Effect of Bimodal Grain Size Distribution on Scatter in Toughness, Metall. Mater. Trans. A, 40, 780–795 (10.1007/s11661-009-9794-4)

Chang S.K. (2005), Influence of Hot Band Normalizing on Recrystallization Behaviour in Grain Oriented Silicon Steels, Steel Res. Int., 76, 660–665 (10.1002/srin.200506072)

Chang S.K. (2007), Texture change from primary to secondary recrystallization by hot-band normalizing in grain-oriented silicon steels, 453, 93–98 (10.1016/j.msea.2006.10.118)

Chatterjee A., et al. (2018), Role of hierarchical martensitic microstructure on localized deformation and fracture of 9Cr-1Mo steel under impact loading at different temperatures, Int. J. Plast., 104, 104–133 (10.1016/j.ijplas.2018.02.002)

Chen J.H., Zhu L., and Ma H. (1990), On the scattering of the local fracture stress, Acta Metall. Mater., 38, 2527–2535 (10.1016/0956-7151(90)90264-H)

Chen N., Zaefferer S., Lahn L., Günther K., and Raabe D. (2003), Effects of topology on abnormal grain growth in silicon steel, Acta Mater., 51, 1755–1765 (10.1016/S1359-6454(02)00574-8)

Choi S.-H., and Jin Y.-S. (2004), Evaluation of stored energy in cold-rolled steels from EBSD data, Mater. Sci. Eng. A, 371, 149–159 (10.1016/j.msea.2003.11.034)

de Dafé S.S.F., Paolinelli S.D.C., and Cota A.B. (2011), Influence of thermomechanical processing on shear bands formation and magnetic properties of a 3% Si non-oriented electrical steel, J. Magn. Magn. Mater., 323, 3234–3238 (10.1016/j.jmmm.2011.07.015)

Dillamore I.L., Roberts J.G., and Bush A.C. (1979), Occurrence of shear bands in heavily rolled cubic metals, Met. Sci., 13, 73–77

(10.1179/msc.1979.13.2.73)

Dodd B., and Boddington P. (1980), The causes of edge cracking in cold rolling, J. Mech. Work. Technol., 3, 239–252 (10.1016/0378-3804(80)90045-5)

Dorner D., and Zaefferer S. (2005), Microstructure and Texture of Shear Bands in Cold Rolled Silicon Steel Single Crystals of Goss Orientation, Solid State Phenom., 105, 239–244 (10.4028/www.scientific.net/SSP.105.239)

Dorner D., Zaefferer S., and Raabe D. (2007), Retention of the Goss orientation between microbands during cold rolling of an Fe3%Si single crystal, Acta Mater., 55, 2519–2530 (10.1016/j.actamat.2006.11.048)

Du C., Maresca F., Geers M.G.D., and Hoefnagels J.P.M. (2018), Ferrite slip system activation investigated by uniaxial micro-tensile tests and simulations, Acta Mater., 146, 314–327 (10.1016/j.actamat.2017.12.054)

Engler O., and Randle V. (2009), Introduction to Texture Analysis, CRC Press.(10.1201/9781420063660)

Engler O., Tomé C.N., and Huh M.Y. (2000), A study of through-thickness texture gradients in rolled sheets, Metall. Mater. Trans. A, 31, 2299–2315 (10.1007/s11661-000-0146-7)

Fang F., et al. (2016), Inhibitor induced secondary recrystallization in thin-gauge grain oriented silicon steel with high permeability, Mater. Des., 105, 398–403 (10.1016/j.matdes.2016.05.091)

Fang F., et al. (2017), The impact of niobium on the microstructure, texture and magnetic properties of strip-cast grain oriented silicon steel, J. Magn. Magn. Mater., 442, 1–7 (10.1016/j.jmmm.2017.06.058)

Gangli P., and Szpunar J.A. (1994), The role of σ5 coincidence boundaries in the growth selection of Fe—3% Si, J. Mater. Process. Technol., 47, 167–184 (10.1016/0924-0136(94)90093-0)

Gerberich W.W., Chen Y.T., Atteridge D.G., and Johnson T. (1981), Plastic flow of Fe-binary alloys—II. Application of the description to the ductile-brittle transition, Acta Metall., 29, 1187–1201 (10.1016/0001-6160(81)90069-9)

Gerberich W.W., and Kurman E. (1985), New contributions to the effective surface energy of cleavage, Scr. Metall., 19, 295–298 (10.1016/0036-9748(85)90317-5)

Gheorghies C., and Doniga A. (2009), Evolution of texture in grain oriented silicon steels, J. Iron Steel Res. Int., 16, 78–83 (10.1016/S1006-706X(09)60065-0)

Ghosh A. (2001), Segregation in cast products, Sadhana, 26, 5–24 (10.1007/BF02728476)

Ghosh A., Kundu S., and Chakrabarti D. (2014), Effect of crystallographic texture on the cleavage fracture mechanism and effective grain size of ferritic steel, Scr. Mater., 81, 8–11 (10.1016/j.scriptamat.2014.02.007)

Ghosh A., Patra S., Chatterjee A., and Chakrabarti D. (2016), Effect of Local Crystallographic Texture on the Fissure Formation During Charpy Impact Testing of Low-Carbon Steel, Metall. Mater. Trans. A, 47, 2755–2772 (10.1007/s11661-016-3458-y)

Ghosh A., Ray A., Chakrabarti D., and Davis C.L. (2013), Cleavage initiation in steel: Competition between large grains and large particles, Mater. Sci. Eng. A, 561, 126–135 (10.1016/j.msea.2012.11.019)

Giri S.K., Durgaprasad A., Mehtani H., Kundu S., and Samajdar I. (2020), Origin of Goss (110)⟨001⟩ Grains in Hot-Worked Grain-Oriented Steel, Metall. Mater. Trans. A, 51, 5268–5284 (10.1007/s11661-020-05920-z)

González F., and Houbaert Y. (2013), A review of ordering phenomena in iron-silicon alloys, Rev. Metal., 49, 178–199 (10.3989/revmetalm.1223)

Günther K., Abbruzzese G., Fortunati S., and Ligi G. (2005), Recent Technology Developments in the Production of Grain-Oriented Electrical Steel, Steel Res. Int., 76, 413–421 (10.1002/srin.200506030)

Guo W., and Mao W. (2010), Abnormal Growth of Goss Grains in Grain-oriented Electrical Steels, J. Mater. Sci. Technol., 26, 759–762 (10.1016/S1005-0302(10)60120-X)

Haiji H., Okada K., Hiratani T., Abe M., and Ninomiya M. (1996), Magnetic properties and workability of 6.5% Si steel sheet, J. Magn. Magn. Mater., 160, 109–114 (10.1016/0304-8853(96)00128-X)

Han M.H., et al. (1999), Analysis and prevention of edge cracking phenomenon during hot rolling of non-oriented electrical steel sheets, Mater. Sci. Eng. A, 264, 47–59 (10.1016/S0921-5093(98)01114-9)

Harase J. (1992), Effect of Cross Rolling Reduction on the Texture Evolution by Grain Growth in Fe-3% Si Alloy, Mater. Sci. Forum, 94–96, 419–424 (10.4028/www.scientific.net/MSF.94-96.419)

Harase J., and Shimizu R. (1988), Distribution of {110}⟨001⟩ Oriented Grains in the Primary Recrystallized 3% Si–Fe Alloy, Trans. Japan Inst. Met., 29, 388–398 (10.2320/matertrans1960.29.388)

Harase J., Shimizu R., and Dingley D.J. (1991), Texture evolution in the presence of precipitates in Fe−3% Si alloy, Acta Metall. Mater., 39, 763–770 (10.1016/0956-7151(91)90276-7)

Haratani T., Hutchinson W.B., Dillamore I.L., and Bate P. (1984), Contribution of shear banding to origin of Goss texture in silicon iron, Met. Sci., 18, 57–66 (10.1179/030634584790420258)

Haratani T, Hutchinson W.B., Dillamore I.L., and Bate P. (1984), Contribution of shear banding to origin of Goss texture in silicon iron, Met. Sci., 18, 57–66 (10.1179/030634584790420258)

HASHIMOTO O. (1988), Formation Mechanism of Goss Texture in Hot Rolled 3% Silicon Steel, Tetsu-to-Hagane, 74, 1633–1640 (10.2355/tetsutohagane1955.74.8_1633)

Hayakawa Y. (2017), Mechanism of secondary recrystallization of Goss grains in grain-oriented electrical steel, Sci. Technol. Adv. Mater., 18, 480–497 (10.1080/14686996.2017.1341277)

Hayakawa Y., and Kurosawa M. (2002), Orientation relationship between primary and secondary recrystallized texture in electrical steel, Acta Mater., 50, 4527–4534 (10.1016/S1359-6454(02)00271-9)

Hayakawa Y., Muraki M., and Szpunar J.A. (1998), The changes of grain boundary character distribution during the secondary recrystallization of electrical steel, Acta Mater., 46, 1063–1073 (10.1016/S1359-6454(97)00303-0)

Hayakawa Y., and Szpunar J.A. (1997), The role of grain boundary character distribution in secondary recrystallization of electrical steels, Acta Mater., 45, 1285–1295 (10.1016/S1359-6454(96)00251-0)

Hayakawa Y, and Szpunar J.A. (1997), A new model of Goss texture development during secondary recrystallization of electrical steel, Acta Mater., 45, 4713–4720 (10.1016/S1359-6454(97)00111-0)

Heo N.H., Chai K.H., Na J.G., Kim J., and Woo J.S. (1999), Nucleation and development of Goss texture and magnetic induction in thin-gauged 3% Si–Fe alloy, J. Appl. Phys., 85, 6022–6024 (10.1063/1.369069)

Hertzberg R.W., and Saunders H. (1985), Deformation and Fracture Mechanics of Engineering Materials (2nd Edition), J. Press. Vessel Technol., 107, 309–311 (10.1115/1.3264456)

Hillert M. (1965), On the theory of normal and abnormal grain growth, Acta Metall., 13, 227–238 (10.1016/0001-6160(65)90200-2)

Hölscher M., Raabe D., and Lücke K. (1991), Rolling and recrystallization textures of bcc steels, Steel Res., 62, 567–575 (10.1002/srin.199100451)

Hou C.-K. (1996), Effect of silicon on the loss separation and permeability of laminated steels, J. Magn. Magn. Mater., 162, 280–290 (10.1016/S0304-8853(96)00268-5)

Hou C. (1996), Effect of Hot Band Annealing Temperature on the Magnetic Properties of Low-carbon Electrical Steels., ISIJ Int., 36, 563–571 (10.2355/isijinternational.36.563)

Houbaert Y., Ros-Yáñez T., Rodriguez-Calvillo P., Barros J., and Kestens L. (2007), On the Effect of Texture in Experimental Grades of High-Silicon Electrical Steel, Mater. Sci. Forum, 539–543, 3341–3346 (10.4028/www.scientific.net/MSF.539-543.3341)

Van Houtte P., Delannay L., and Samajdar I. (1999), Quantitative Prediction of Cold Rolling Textures in Low-Carbon Steel by Means of the Lamel Model, Textures Microstruct., 31, 109–149 (10.1155/TSM.31.109)

Hsu C. (1986), Correlation of hot-microhardness with elevated-temperature tensile properties of low activation ferritic steel, J. Nucl. Mater., 141–143, 518–522 (10.1016/S0022-3115(86)80093-9)

Hu W.L., et al. (2021), Applying crystallographic orientation analysis for exploring deformation mechanism of 6.5 wt.% Si electrical strip during twin-roll thin strip casting process, J. Mater. Res. Technol., 13, 1980–1991 (10.1016/j.jmrt.2021.06.002)

Hughes G.M., Smith G., Crocker A.G., and Flewitt P.E.J. (2005), An examination of the linkage of cleavage cracks at grain boundaries, Mater. Sci. Technol., 21, 1268–1274 (10.1179/174328405X69542)

Hughes I.F. (1971), The effect of finishing temperature on the texture and structure of hot rolled 1 pct Si steel, Metall. Trans., 2, 929–936 (10.1007/BF02664221)

Humane M.M., Thool K.S., Minz R.K., and Kestens L.A.I. (2015), Microstructures and Textures of Hot Rolled and Hot Rolled-Normalized 2.9 % Silicon Steel Sheets, Trans. Indian Inst. Met., 68, 371–381 (10.1007/s12666-014-0465-9)

Hutchinson B. (1999), Deformation microstructures and textures in steels, M. F. Ashby, F. J. Humphreys, C. M. Sellar, H. R. Shercliff, and M. J. Stowell (eds) Philos. Trans. R. Soc. London. Ser. A Math. Phys. Eng. Sci., 357, 1471–1485 (10.1098/rsta.1999.0385)

Imamura T., Shingaki Y., and Hayakawa Y. (2013), Effect of Cold Rolling Reduction Rate on Secondary Recrystallized Texture in 3 Pct Si-Fe Steel, Metall. Mater. Trans. A, 44, 1785–1792 (10.1007/s11661-012-1525-6)

Inokuti Y. (1996), Preferential Growth of Secondary Recrystallized Goss Grains During Secondary Recrystallization Annealing in Grain Oriented Silicon Steel Sheet, Textures Microstruct., 26, 413–426 (10.1155/TSM.26-27.413)

INOKUTI Y. (1984), Mechanism of Secondary Recrystallization in Grain Oriented Silicon Steel, Tetsu-to-Hagane, 70, 2033–2040

(10.2355/tetsutohagane1955.70.15_2033)

INOKUTI Y., MAEDA C., ITO Y., and SHIMANAKA H. (1983), Transmission Kossel study of origin of Goss texture in grain oriented silicon steel., Trans. Iron Steel Inst. Japan, 23, 440–449 (10.2355/isijinternational1966.23.440)

Jahangiri M.R., Bajgholi A., and Zhaam A.A. (2014), Development of a new three-stage cold rolling manufacturing technology for grain-oriented silicon steel sheets, Int. J. Adv. Manuf. Technol., 75, 1291–1298 (10.1007/s00170-014-6251-3)

Jain V., Modak P., Patra S., and Ghosh A. (2022), Origin of Goss texture in grain oriented electrical steel: Role of shear bands, Materialia, 22, 101398 (10.1016/j.mtla.2022.101398)

Jain V., Patra S., Halder C., Hasan S.M., and Ghosh A. (2022), Study on the formation of alligator crack and edge crack in high silicon grain oriented electrical steel during cold rolling, J. Appl. Phys., 132, 105101 (10.1063/5.0097174)

Joo M.S., Suh D.-W., Bae J.H., and Bhadeshia H.K.D.H. (2012), Role of delamination and crystallography on anisotropy of Charpy toughness in API-X80 steel, Mater. Sci. Eng. A, 546, 314–322 (10.1016/j.msea.2012.03.079)

Kawata I., Nakai H., and Aihara S. (2018), Experimental evaluation of effective surface energy for cleavage microcrack propagation across grain boundary in steels, Acta Mater., 150, 40–52 (10.1016/j.actamat.2018.02.057)

Kestens L., and Jacobs S. (2008), Texture Control During the Manufacturing of Nonoriented Electrical Steels, Texture, Stress. Microstruct., 2008, 1–9 (10.1155/2008/173083)

Kestens L., Jonas J.J., Van Houtte P., and Aernoudt E. (1996), Orientation selective recrystallization of nonoriented electrical steels, Metall. Mater. Trans. A, 27, 2347–2358 (10.1007/BF02651889)

Kim H., Kang M., Shin S.Y., and Lee S. (2013), Alligatoring phenomenon occurring during hot rolling of free-machining steel wire rods, Mater. Sci. Eng. A, 568, 8–19 (10.1016/j.msea.2013.01.018)

Kim J.K., Lee D.N., and Koo Y.M. (2014), The evolution of the Goss and Cube textures in electrical steel, Mater. Lett., 122, 110–113 (10.1016/j.matlet.2014.01.166)

Kim M.-C., Jun Oh Y., and Hwa Hong J. (2000), Characterization of boundaries and determination of effective grain size in Mn-Mo-Ni low alloy steel from the view of misorientation, Scr. Mater., 43, 205–211 (10.1016/S1359-6462(00)00392-4)

Kim N.J., Nakagawa A.H., and Nakagawa A.H. (1986), Effective grain size of dual-phase steel, Mater. Sci. Eng., 83, 145–149 (10.1016/0025-5416(86)90181-3)

King A., et al. (2011), Three-dimensional in situ observations of short fatigue crack growth in magnesium, Acta Mater., 59, 6761–6771 (10.1016/j.actamat.2011.07.034)

Knott J.F. (1973) (1973), Fundamentals of Fracture Mechanics - J.F. Knott.pdf,

Kumano T., Haratani T., and Ushigami Y. (2002), The Relationship between Primary and Secondary Recrystallization Texture of Grain Oriented Silicon Steel, ISIJ Int., 42, 440–448 (10.2355/isijinternational.42.440)

Kumano T., Haratani T., and Ushigami Y. (2003a), Influence of Primary Recrystallization Texture through Thickness to Secondary Texture on Grain Oriented Silicon Steel., ISIJ Int., 43, 400–409 (10.2355/isijinternational.43.400)

Kumano T., Haratani T., and Ushigami Y. (2003b), The Improvement of Primary Texture for Sharp Goss Orientation on Grain Oriented Silicon Steel, ISIJ Int., 43, 736–745 (10.2355/isijinternational.43.736)

Lebensohn R.A., and Tomé C.N. (1993), A self-consistent anisotropic approach for the simulation of plastic deformation and texture development of polycrystals: Application to zirconium alloys, Acta Metall. Mater., 41, 2611–2624 (10.1016/0956-7151(93)90130-K)

Lee H.H., Jung J., Yoon J.I., Kim J.-K., and Kim H.S. (2018), Modelling the evolution of recrystallization texture for a non-grain oriented electrical steel, Comput. Mater. Sci., 149, 57–64 (10.1016/j.commatsci.2018.03.013)

Li Y., Mao W., and Yang P. (2011), Inhomogeneous Distribution of Second Phase Particles in Grain Oriented Electrical Steels, J. Mater. Sci. Technol., 27, 1120–1124 (10.1016/S1005-0302(12)60006-1)

Li Z., Dang N., and Mi Z. (2016), Effect of Hot Deformation Temperature on Texture Formation Regularity of CGO Silicon Steel under High Deformation Rate, Adv. Mater. Sci. Eng., 2016, 1–8 (10.1155/2016/7010613)

Libovický S. (1971), Two modes of slip systems in iron silicon crystals, Czechoslov. J. Phys., 21, 1153–1162 (10.1007/BF01724945)

Lin K.C., and Jong-Sen Hsu (1995), Selection of silicon steel for transformer cores,. Proceedings:Electrical Electronics Insulation Conference and Electrical Manufacturing & Coil Winding Conference, 147–152. Electr. Manuf. & Coil Winding Assoc(10.1109/EEIC.1995.482355)

Lin P., Palumbo G., Harase J., and Aust K.T. (1996), Coincidence Site Lattice (CSL) grain boundaries and Goss texture development in Fe-

3% Si alloy, Acta Mater., 44, 4677–4683 (10.1016/S1359-6454(96)00140-1)

Littman M.F. (1982), Grain-oriented silicon steel sheets, J. Magn. Magn. Mater., 26, 1–10 (10.1016/0304-8853(82)90103-2)

Littmann M.F. (1975), Development of improved cube-on-edge texture from strand cast 3pct silicon-iron, Metall. Trans. A, 6, 1041–1048 (10.1007/BF02661358)

Liu J., Sha Y., Hu K., Zhang F., and Zuo L. (2014), Formation of Cube and Goss Texture After Primary Recrystallization in Electrical Steels, Metall. Mater. Trans. A, 45, 134–138 (10.1007/s11661-013-1917-2)

Lu N., et al. (2020), Dynamics of particle-assisted abnormal grain growth revealed through integrated three-dimensional microanalysis, Acta Mater., 195, 1–12 (10.1016/j.actamat.2020.04.049)

Maazi N., Rouag N., Etter A.L., Penelle R., and Baudin T. (2006), Influence of neighbourhood on abnormal Goss grain growth in Fe–3% Si steels: Formation of island grains in the large growing grain, Scr. Mater., 55, 641–644 (10.1016/j.scriptamat.2006.06.007)

Matsuo M. (1989), Texture control in the production of grain oriented silicon steels., ISIJ Int., 29, 809–827 (10.2355/isijinternational.29.809)

Matsuo M., Sakai T., and Suga Y. (1986), Origin and development of through-the-thickness variations of texture in the processing of grain-oriented silicon steel, Metall. Trans. A, 17, 1313–1322 (10.1007/BF02650112)

MATSUOKA T. (1967), Effect of Impurities on the Secondary Recrystallization in Silicon Iron, Tetsu-to-Hagane, 53, 1007–1023 (10.2355/tetsutohagane1955.53.8_1007)

Mehdi M., He Y., Hilinski E.J., Kestens L.A.I., and Edrisy A. (2019), The

Origins of the Goss Orientation in Non-Oriented Electrical Steel and the Evolution of the Goss Texture during Thermomechanical Processing, Steel Res. Int., 90, 1800582 (10.1002/srin.201800582)

Mehdi M., He Y., Hilinski E.J., Kestens L.A.I., and Edrisy A. (2020), The evolution of cube ({001}<100>) texture in non-oriented electrical steel, Acta Mater., 185, 540–554 (10.1016/j.actamat.2019.12.024)

Mehring M., and Weberruß V.A. (2001), Introduction to Magnetic Resonance,. Object-Oriented Magnetic Resonance, 322. Elsevier(10.1016/B978-0-08-051297-6.50025-3)

Merson E., et al. (2016), The Use of Confocal Laser Scanning Microscopy for the 3D Quantitative Characterization of Fracture Surfaces and Cleavage Facets., Procedia Struct. Integr., 2, 533–540 (10.1016/j.prostr.2016.06.069)

Mishra S., Därmann C., and Lücke K. (1986), New information on texture development in regular and high-permeability grain-oriented silicon steels, Metall. Trans. A, 17, 1301–1312 (10.1007/BF02650111)

Miyazaki M., Murao T., and Isobe K. (2013), Formation Mechanism and Modeling of Centerline Segregation, Nippon Steel Tech. Rep., 48–53

Molinari A., Canova G.R., and Ahzi S. (1987), A self consistent approach of the large deformation polycrystal viscoplasticity, Acta Metall., 35, 2983–2994 (10.1016/0001-6160(87)90297-5)

Moses A.J. (1990), Electrical steels: past, present and future developments, IEE Proc. A (Physical Sci. Meas. Instrumentation, Manag. Educ., 137, 233–245 (10.1049/ip-a-2.1990.0039)

Murakami K., Morishige N., and Ushioda K. (2012), The Effect of Cold Rolling Reduction on Shear Band and Texture Formation in Fe-3%Si Alloy, Mater. Sci. Forum, 715–716, 158–163 (10.4028/www.scientific.net/MSF.715-716.158)

Nakanishi D., Kawabata T., and Aihara S. (2016), An Observation of Brittle Crack Propagation in Coarse Grained 3% Silicon Steel, Procedia Struct. Integr., 2, 493–500 (10.1016/j.prostr.2016.06.064)

Nguyen-Minh T., Sidor J.J., Petrov R.H., and Kestens L.A.I. (2012), Occurrence of shear bands in rotated Goss ({110}〈110〉) orientations of metals with bcc crystal structure, Scr. Mater., 67, 935–938 (10.1016/j.scriptamat.2012.08.017)

Novák V., Saleeb K.Z., Kadečková S., and Šesták B. (1976), Work-hardening of Fe, Fe-0·5 wt% Si and Fe-0·9 wt% Si single crystals, Czechoslov. J. Phys., 26, 565–576 (10.1007/BF01586888)

Omura T., and Hayakawa Y. (2013), Influence of Primary-Recrystallization Texture on Selective Growth of Goss Grains, Mater. Trans., 54, 14–21 (10.2320/matertrans.M2012303)

Ouyang G., Chen X., Liang Y., Macziewski C., and Cui J. (2019), Review of Fe-6.5 wt%Si high silicon steel—A promising soft magnetic material for sub-kHz application, J. Magn. Magn. Mater., 481, 234–250 (10.1016/j.jmmm.2019.02.089)

Pan H., Zhang Z., and Xie J. (2016), Preparation of High Silicon Electrical Steel Sheets with Strong {100} Recrystallization Texture by the Texture Inheritance of Initial Columnar Grains, Metall. Mater. Trans. A, 47, 2277–2285 (10.1007/s11661-016-3371-4)

Pandey J.C., Raj M., and Choubey P.N. (2009), Split Ends and Cracking Problem During Hot Rolling of Continuously Cast Steel Billets, J. Fail. Anal. Prev., 9, 88–96 (10.1007/s11668-008-9194-x)

Park J.-T., and Szpunar J.A. (2003), Evolution of recrystallization texture in nonoriented electrical steels, Acta Mater., 51, 3037–3051 (10.1016/S1359-6454(03)00115-0)

Park J.-T., and Szpunar J.A. (2009), Effect of initial grain size on texture evolution and magnetic properties in nonoriented electrical steels, J. Magn. Magn. Mater., 321, 1928–1932 (10.1016/j.jmmm.2008.12.015)

Park J.Y., et al. (2002), Influence of primary annealing condition on texture development in grain oriented electrical steels, Acta Mater., 50, 1825–1834 (10.1016/S1359-6454(02)00034-4)

Park N.-J., Joo H.-D., and Park J.-T. (2013), Evolution of Goss Orientation during Thermal Heating with Different Heating Rate for Primary Recrystallization in Grain-oriented Electrical Steel, ISIJ Int., 53, 125–130 (10.2355/isijinternational.53.125)

Park N.-J., Lee E.-J., Joo H.-D., and Park J.-T. (2011), Evolution of Goss Orientation during Rapid Heating for Primary Recrystallization in Grain-oriented Electrical Steel, ISIJ Int., 51, 975–981 (10.2355/isijinternational.51.975)

Pavlina E.J., and Van Tyne C.J. (2008), Correlation of Yield Strength and Tensile Strength with Hardness for Steels, J. Mater. Eng. Perform., 17, 888–893 (10.1007/s11665-008-9225-5)

Pease N.C., Jones D.W., Wise M.H.L., and Hutchinson W.B. (1981), SEM study of origin of Goss texture in Fe-3.25Si, Met. Sci., 15, 203–209 (10.1179/030634581790426642)

Piehler H.R. (2009), Crystal-Plasticity Fundamentals,. Fundamentals of Modeling for Metals Processing, 232–238. ASM International(10.31399/asm.hb.v22a.a0005400)

Qiao Y., and Argon A.. (2003), Cleavage cracking resistance of high angle grain boundaries in Fe–3%Si alloy, Mech. Mater., 35, 313–331 (10.1016/S0167-6636(02)00284-3)

Qin J., Yang P., Mao W., and Ye F. (2015), Effect of texture and grain size on the magnetic flux density and core loss of cold-rolled high silicon steel sheets, J. Magn. Magn. Mater., 393, 537–543 (10.1016/j.jmmm.2015.06.032)

Raabe D. (1995), Simulation of rolling textures of b.c.c. metals considering grain interactions and crystallographic slip on {110}, {112} and {123} planes, Mater. Sci. Eng. A, 197, 31–37 (10.1016/0921-5093(94)09770-4)

Raabe D. (2003), Overview on Basic Types of Hot Rolling Textures of Steels, Steel Res. Int., 74, 327–337 (10.1002/srin.200300194)

Raabe D., and Lücke K. (1992), Texture and microstructure of hot rolled steel, Scr. Metall. Mater., 26, 1221–1226 (10.1016/0956-716X(92)90567-X)

Raabe D., Zhao Z., Park S.-J., and Roters F. (2002), Theory of orientation gradients in plastically strained crystals, Acta Mater., 50, 421–440 (10.1016/S1359-6454(01)00323-8)

Rajmohan N. (1997), Neutron diffraction method for stored energy measurement in interstitial free steel, Acta Mater., 45, 2485–2494 (10.1016/S1359-6454(96)00371-0)

Rajmohan N., and Szpunar J.. (2001), An analytical method for characterizing grain boundaries around growing goss grains during secondary recrystallization, Scr. Mater., 44, 2387–2392 (10.1016/S1359-6462(01)00941-1)

Rajmohan N., Szpunar J.., and Hayakawa Y. (1999), A role of fractions of mobile grain boundaries in secondary recrystallization of Fe–Si steels, Acta Mater., 47, 2999–3008 (10.1016/S1359-6454(99)00162-7)

Rajmohan N., and Szpunar J.A. (2000), Monte-Carlo simulation of Goss texture development in silicon steel in the presence of MnS particles, Mater. Sci. Eng. A, 289, 99–108 (10.1016/S0921-5093(00)00902-3)

Rajmohan N., Szpunar J.A., and Hayakawa Y. (1999), Importance of fractions of highly mobile boundaries in abnormal growth of Goss grains, Mater. Sci. Eng. A, 259, 8–16 (10.1016/S0921-5093(98)00879-X)

Randle V., and Davies P. (2005), Crystallography of brittle fracture and deformation twinning in ferritic steels, Mater. Sci. Technol., 21, 1275–1281 (10.1179/174328405X67003)

Raphanel J.L., and Van Houtte P. (1985), Simulation of the rolling textures of b.c.c. metals by means of the relaxed taylor theory, Acta Metall., 33, 1481–1488 (10.1016/0001-6160(85)90049-5)

Ray R.K., Jonas J.J., and Hook R.E. (1994), Cold rolling and annealing textures in low carbon and extra low carbon steels, Int. Mater. Rev., 39, 129–172 (10.1179/imr.1994.39.4.129)

Réger M., Verő B., Kardos I., and Varga P. (2010), The Effect of Alloying Elements on the Stability of Centerline Segregation, Defect Diffus. Forum, 297–301, 148–153 (10.4028/www.scientific.net/DDF.297-301.148)

Ros-Yanez T., Ruiz D., Barros J., Houbaert Y., and Colás R. (2007), Study of deformation and aging behaviour of iron–silicon alloys, Mater. Sci. Eng. A, 447, 27–34 (10.1016/j.msea.2006.10.075)

Rouag N., Vigna G., and Penelle R. (1990), Evolution of local texture and grain boundary characteristics during secondary recrystallisation of Fe-3% Si sheets, Acta Metall. Mater., 38, 1101–1107 (10.1016/0956-7151(90)90182-G)

Sakai T., Shiozaki M., and Takashina K. (1979), A study on AlN in high permeability grain-oriented silicon steel, J. Appl. Phys., 50, 2369–2371 (10.1063/1.327007)

Samajdar I, Cicale S., Verlinden B., Van Houtte P., and Abbruzzesse G.

(1998), Primary recrystallization in a grain oriented silicon steel: on the origin of goss {110}<001> grains, Scr. Mater., 39, 1083–1088 (10.1016/S1359-6462(98)00288-7)

Samajdar I., Verlinden B., and Houtte P. Van (1998), Developments in Macro and Micro Texture during Plane Strain Channel Die Compression of IF Steel., ISIJ Int., 38, 759–765 (10.2355/isijinternational.38.759)

Samajdar I., Verlinden B., Van Houtte P., and Vanderschueren D. (1997), γ-Fibre recrystallization texture in IF-steel: an investigation on the recrystallization mechanisms, Mater. Sci. Eng. A, 238, 343–350 (10.1016/S0921-5093(97)00455-3)

Samei J., Salib Y., Amirmaleki M., and Wilkinson D.S. (2019), The role of microstructure on edge cracks in dual phase and quench and partitioning steels subject to severe cold rolling, Scr. Mater., 173, 86–90 (10.1016/j.scriptamat.2019.08.012)

Sarkar A., and Chakravartty J.K. (2011), Application of Visco-Plastic Self Consistent Approach to Model Deformation Characteristics of Magnesium with Different Textures, Mater. Sci. Forum, 702–703, 80–84 (10.4028/www.scientific.net/MSF.702-703.80)

Sarkar A., Sanyal S., Bandyopadhyay T.K., and Mandal S. (2019), Implications of microstructure, Taylor factor distribution and texture on tensile properties in a Ti-added Fe-Mn-Al-Si-C steel, Mater. Sci. Eng. A, 767, 138402 (10.1016/j.msea.2019.138402)

Schneider J., Franke A., Stöcker A., and Kawalla R. (2016), Deformation Structure and Recrystallization of Ferritic FeSi Steels, Steel Res. Int., 87, 1054–1064 (10.1002/srin.201500447)

Searcy A.W. (1986), Origins of Planar, Concave, and Convex Boundaries During Exaggerated Grain Growth, J. Am. Ceram. Soc., 69, C-91-C–

92 (10.1111/j.1151-2916.1986.tb04776.x)

Shao Y., Yang P., Fu Y., and Mao W. (2013), Texture Evolution of Columnar Grains in Electrical Steel During Hot Rolling, J. Iron Steel Res. Int., 20, 99–106 (10.1016/S1006-706X(13)60184-3)

Shimizu R., and Harase J. (1989), Coincidence grain boundary and texture evolution in Fe-3%Si, Acta Metall., 37, 1241–1249 (10.1016/0001-6160(89)90118-1)

Shimizu Y., Ito Y., and Iida Y. (1986), Formation of the Goss orientation near the surface of 3 pct silicon steel during hot rolling, Metall. Trans. A, 17, 1323–1334 (10.1007/BF02650113)

SHIN S.M., BIROSCA S., CHANG S.K., and DE COOMAN B.C. (2008), Texture evolution in grain-oriented electrical steel during hot band annealing and cold rolling, J. Microsc., 230, 414–423 (10.1111/j.1365-2818.2008.02001.x)

Slavik D.C., Wert J.A., and Gangloff R.P. (1993), Determining fracture facet crystallography using electron backscatter patterns and quantitative tilt fractography, J. Mater. Res., 8, 2482–2491 (10.1557/JMR.1993.2482)

Song H.-Y., et al. (2016), Effects of Two-Stage Cold Rolling Schedule on Microstructure and Texture Evolution of Strip Casting Grain-Oriented Silicon Steel with Extra-Low Carbon, Metall. Mater. Trans. A, 47, 1770–1781 (10.1007/s11661-016-3334-9)

Song H.-Y., Liu H.-T., Wang Y.-P., and Wang G.-D. (2017), Microstructure and texture evolution of ultra-thin grain-oriented silicon steel sheet fabricated using strip casting and three-stage cold rolling method, J. Magn. Magn. Mater., 426, 32–39 (10.1016/j.jmmm.2016.11.038)

Song H.-Y., Wang Y.-P., Esling C., Wang G.-D., and Liu H.-T. (2021), The role of grain colony on secondary recrystallization in grain-oriented electrical steel: New insights from an original tracking experiment, Acta Mater., 206, 116611 (10.1016/j.actamat.2020.116611)

Sopko M., Kováč F., Petryshynets I., Molnárová M., and Gavendová P. (2014), Differential Scanning Calorimetry and Metallographic Analysis of Fe-Si Electrical Steel, Mater. Sci. Forum, 782, 129–132 (10.4028/www.scientific.net/MSF.782.129)

Sorbello F., Flewitt P.E.J., Smith G., and Crocker A.G. (2009), The role of deformation twins in brittle crack propagation in iron–silicon steel, Acta Mater., 57, 2646–2656 (10.1016/j.actamat.2009.02.011)

Srolovitz D.., Grest G.., and Anderson M.. (1985), Computer simulation of grain growth—V. Abnormal grain growth, Acta Metall., 33, 2233–2247 (10.1016/0001-6160(85)90185-3)

Sun Q., Zan D., Chen J., and Pan H. (2015), Analysis of edge crack behavior of steel sheet in multi-pass cold rolling based on a shear modified GTN damage model, Theor. Appl. Fract. Mech., 80, 259–266 (10.1016/j.tafmec.2015.06.003)

Swift W.M. (1973), Kinetics of MnS precipitate coarsening in 3pct Si-Fe sheet, Metall. Trans., 4, 153–157 (10.1007/BF02649614)

Taguchi S., Sakakura A., Matsumoto F., Takashima K., and Kuroki K. (1975), The development of grain-oriented silicon steel with high permeability, J. Magn. Magn. Mater., 2, 121–131 (10.1016/0304-8853(75)90114-6)

Takahashi N., and Harase J. (1996), Recent Development of Technology of Grain Oriented Silicon Steel, Mater. Sci. Forum, 204–206, 143–154 (10.4028/www.scientific.net/MSF.204-206.143)

Takajo S., Vogel S.C., and Tomé C.N. (2019), Viscoplastic self-consistent polycrystal modeling of texture evolution of ultra-low carbon steel during cold rolling, Model. Simul. Mater. Sci. Eng., 27, 045003 (10.1088/1361-651X/ab0b92)

Takenaka M., Fujita N., Hayakawa Y., and Tsuji N. (2018a), Acta Materialia Unique effect of carbon addition on development of deformation texture through changes in slip activation and twin deformation in heavily cold-rolled Fe-3 % Si alloys, Acta Mater., 157, 196–208 (10.1016/j.actamat.2018.07.019)

Takenaka M., Fujita N., Hayakawa Y., and Tsuji N. (2018b), Unique effect of carbon addition on development of deformation texture through changes in slip activation and twin deformation in heavily cold-rolled Fe-3% Si alloys, Acta Mater., 157, 196–208 (10.1016/j.actamat.2018.07.019)

Takeuchi S., Furubayashi E., and Taoka T. (1967), Orientation dependence of yield stress in 4.4% silicon iron single crystals, Acta Metall., 15, 1179–1191 (10.1016/0001-6160(67)90392-6)

Taoka T., Furubayashi E., and Takeuchi S. (1966), Formation of Cold-Rolled Texture and Recrystallized Texture in Single Crystals of 3% Silicon Iron (Part I) - Cold-Rolled Texture -, Trans. Iron Steel Inst. Japan, 6, 290–316 (10.2355/isijinternational1966.6.290)

Turczyn S., and Pietrzyk M. (1992), The effect of deformation zone geometry on internal defects arising in plane strain rolling, J. Mater. Process. Technol., 32, 509–518 (10.1016/0924-0136(92)90207-9)

Turner S., Moses A., Hall J., and Jenkins K. (2010), The effect of precipitate size on magnetic domain behavior in grain-oriented electrical steels, J. Appl. Phys., 107, 09A307 (10.1063/1.3334201)

Ushigami Y., et al. (2003), Recent development of low-loss grain-oriented silicon steel, J. Magn. Magn. Mater., 254–255, 307–314

(10.1016/S0304-8853(02)00933-2)

Ushigami Y., Kubota T., and Takahashi N. (1998), Recrystallization and Related Phenomena. Mechanism of Orientation Selectivity of Secondary Recrystallization in Fe-3%Si Alloy., ISIJ Int., 38, 553–558 (10.2355/isijinternational.38.553)

Ushioda K., and Hutchinson W.B. (1989), Role of shear bands in annealing texture formation in 3%Si-Fe(111)[112] single crystals., ISIJ Int., 29, 862–867 (10.2355/isijinternational.29.862)

Vasudevan A., Ponson L., Karma A., and Leblond J.-B. (2020), Configurational stability of a crack propagating in a material with mode-dependent fracture energy – Part II: Drift of fracture facets in mixed-mode I+II+III, J. Mech. Phys. Solids, 137, 103894 (10.1016/j.jmps.2020.103894)

Wang Y., Xu Y.-B., Zhang Y.-X., Fang F., Lu X., Liu H.-T., et al. (2015), Development of microstructure and texture in strip casting grain oriented silicon steel, J. Magn. Magn. Mater., 379, 161–166 (10.1016/j.jmmm.2014.12.043)

Wang Y., Xu Y.-B., Zhang Y.-X., Fang F., Lu X., Misra R.D.K., et al. (2015), Effect of annealing after strip casting on texture development in grain oriented silicon steel produced by twin roll casting, Mater. Charact., 107, 79–84 (10.1016/j.matchar.2015.07.001)

Wang Y., et al. (2016), Effect of Hot Rolling on Texture, Precipitation, and Magnetic Properties of Strip-Cast Grain-Oriented Silicon Steel, Steel Res. Int., 87, 1601–1608 (10.1002/srin.201600009)

Wittig J.E., and Frommeyer G. (2008), Deformation and Fracture Behavior of Rapidly Solidified and Annealed Iron-Silicon Alloys, Metall. Mater. Trans. A, 39, 252–265 (10.1007/s11661-007-9436-7)

Wright S.I., Nowell M.M., and Field D.P. (2011), A Review of Strain

Analysis Using Electron Backscatter Diffraction, Microsc. Microanal., 17, 316–329 (10.1017/S1431927611000055)

Wu S.J., and Davis C.L. (2004), Effect of duplex ferrite grain size distribution on local fracture stresses of Nb-microalloyed steels, Mater. Sci. Eng. A, 387–389, 456–460 (10.1016/j.msea.2004.01.144)

Xia Z., Kang Y., and Wang Q. (2008), Developments in the production of grain-oriented electrical steel, J. Magn. Magn. Mater., 320, 3229–3233 (10.1016/j.jmmm.2008.07.003)

Xie H., Jiang Z., and Yuen W.Y.D. (2011), Analysis of Microstructure Effects on Edge Crack of Thin Strip During Cold Rolling, Metall. Mater. Trans. B, 42, 1244–1252 (10.1007/s11663-011-9540-3)

Xu L., and Daehn G.S. (1994), Alligatoring and damage in the cold rolling of spheroidized steels, Metall. Mater. Trans. A, 25, 589–598 (10.1007/BF02651600)

Xu L., Liu Q., Song Y., Feng T., and Li Z. (2018), Formation of the primary recrystallization texture in the oriented electrical steel with 3% Si, IOP Conf. Ser. Mater. Sci. Eng., 382, 022102 (10.1088/1757-899X/382/2/022102)

Yan Y., Sun Q., Chen J., and Pan H. (2013), The initiation and propagation of edge cracks of silicon steel during tandem cold rolling process based on the Gurson–Tvergaard–Needleman damage model, J. Mater. Process. Technol., 213, 598–605 (10.1016/j.jmatprotec.2012.11.006)

Yang F., et al. (2017), The Effect of Annealing Atmosphere on the Evolution Behavior of Inhibitors in Thin-Gauge Grain-Oriented Silicon Steel, Mater. Trans., 58, 1524–1531 (10.2320/matertrans.M2017114)

Yoshitomi Y., et al. (1993), Influence Growth of Primary Recrystallized

Grains on Secondary Recrystallization Texture in Fe-3%Si Alloy, Mater. Sci. Forum, 113–115, 715–720 (10.4028/www.scientific.net/MSF.113-115.715)

Yuan W.J., Li R., Shen Q., and Zhang L.M. (2007), Characterization of the evaluation of the solid solubility of Si in sintered Fe–Si alloys using DSC technique, Mater. Charact., 58, 376–379 (10.1016/j.matchar.2006.06.003)

Zan D.Q., Sun Q., Pan H.L., Chen J.J., and Wang Z.D. (2017), Application of the cohesive zone model for analysing the edge crack propagation of steel sheet in the cold rolling process, Fatigue Fract. Eng. Mater. Struct., 40, 869–881 (10.1111/ffe.12548)

Zhai T., Wilkinson A.J., and Martin J.W. (2000), A crystallographic mechanism for fatigue crack propagation through grain boundaries, Acta Mater., 48, 4917–4927 (10.1016/S1359-6454(00)00214-7)

Zhang N., et al. (2021), Experimental investigation and simulation of crystallographic orientations evolution in a cold-rolled ultra-thin grain-oriented silicon steel, J. Magn. Magn. Mater., 517, 167385 (10.1016/j.jmmm.2020.167385)

Zhu C., Liu Y., Xiao Y., Yan W., and Li G. (2022), A New Review on Inclusion and Precipitate Control in Grain-Oriented Silicon Steels, JOM, 74, 3141–3161 (10.1007/s11837-022-05345-6)